Techniques en Appui des Formats de Modulation Avancés pour les Futurs Réseaux Optiques

Thèse

Siamak Amiralizadeh Asl

Doctorat en génie électrique
Philosophiæ doctor (Ph.D.)

Québec, Canada

Résumé

Les systèmes de communication optique avec des formats de modulation avancés sont actuellement l'un des sujets de recherche les plus importants dans le domaine de communication optique. Cette recherche est stimulée par les exigences pour des débits de transmission de donnée plus élevés. Dans cette thèse, on examinera les techniques efficaces pour la modulation avancée avec une détection cohérente, et multiplexage par répartition en fréquence orthogonale (OFDM) et multiples tonalités discrètes (DMT) pour la détection directe et la détection cohérente afin d'améliorer la performance de réseaux optiques.

Dans la première partie, nous examinons la rétropropagation avec filtre numérique (DFBP) comme une simple technique d'atténuation de nonlinéarité d'amplificateur optique semiconducteur (SOA) dans le système de détection cohérente. Pour la première fois, nous démontrons expérimentalement l'efficacité de DFBP pour compenser les nonlinéarités générées par SOA dans un système de détection cohérente porteur unique 16-QAM. Nous comparons la performance de DFBP avec la méthode de Runge-Kutta quatrième ordre. Nous examinons la sensibilité de performance de DFBP par rapport à ses paramètres. Par la suite, nous proposons une nouvelle méthode d'estimation de paramètre pour DFBP. Finalement, nous démontrons la transmission de signaux de 16-QAM aux taux de 22 Gbaud sur 80 km de fibre optique avec la technique d'estimation de paramètre proposée pour DFBP.

Dans la deuxième partie, nous nous concentrons sur les techniques afin d'améliorer la performance des systèmes OFDM optiques en examinent OFDM optiques cohérente (CO-OFDM) ainsi que OFDM optiques détection directe (DDO-OFDM). Premièrement, nous proposons une combinaison de coupure et prédistorsion pour compenser les distorsions nonlinéaires d'émetteur de CO-OFDM. Nous utilisons une interpolation linéaire par morceaux (PLI) pour charactériser la nonlinéarité d'émetteur. Dans l'émetteur nous utilisons l'inverse de l'estimation de PLI pour compenser les nonlinéarités induites à l'émetteur de CO-OFDM. Deuxièmement, nous concevons des constellations irrégulières optimisées pour les systèmes DDO-OFDM courte distance en considérant deux modèles de bruit de canal. Nous démontrons expérimentalement 100Gb/s+ OFDM/DMT avec la détection directe en utilisant les constellations QAM optimisées.

Dans la troisième partie, nous proposons une architecture réseaux optiques passifs (PON)

avec DDO-OFDM pour la liaison descendante et CO-OFDM pour la liaison montante. Nous examinons deux scénarios pour l'allocations de fréquence et le format de modulation des signaux. Nous identifions la détérioration limitante principale du PON bidirectionnelle et offrons des solutions pour minimiser ses effets.

Abstract

Optical communication systems with advanced modulation formats are currently one of the major research focuses of the optical communication community. This research is driven by the ever-increasing demand for higher data transmission rates. In this thesis, we investigate efficient techniques for advanced modulation with coherent detection, and optical orthogonal frequency-division multiplexing (OFDM) and discrete multi-tone (DMT) for both direct detection and coherent detection to improve the performance of optical networks.

In the first part, we investigate digital filter back-propagation (DFBP) as a simple semiconductor optical amplifier (SOA) nonlinearity mitigation technique in coherent detection systems. For the first time, we experimentally demonstrate effectiveness of DFBP in compensating for SOA-induced nonlinearities in a 16-ary quadrature amplitude modulation (16-QAM) single-carrier coherent detection system. We compare performance of DFBP with Runge-Kutta fourth-order method. We examine sensitivity of DFBP performance to its parameters. Afterwards, we propose a novel parameter estimation method for DFBP. Finally, we demonstrate successful transmission of 22 Gbaud 16-QAM signals over 80 km fiber with the proposed parameter estimation technique for DFBP.

In the second part, we concentrate on techniques to improve performance of optical OFDM systems, examining both coherent optical OFDM (CO-OFDM) and direct-detection optical OFDM (DDO-OFDM). First, we propose a combination of clipping and predistortion technique to compensate for CO-OFDM transmitter nonlinear distortions. We use piecewise linear interpolation (PLI) for characterizing the transmitter nonlinearity. At the transmitter, we use inverse of the PLI estimate to pre-compensate the nonlinearities induced at the CO-OFDM transmitter. Second, we design optimized non-square constellations for short-reach DDO-OFDM systems based on two channel noise models. We experimentally demonstrate 100 Gb/s+ OFDM/DMT with direct detection using the optimized QAM constellations.

In the third part, we propose and experimentally demonstrate a passive optical network (PON) architecture with DDO-OFDM for the downlink and CO-OFDM for the uplink. We examine two scenarios for the occupied frequency and modulation format of the signals. We identify main limiting impairments of the bidirectional PON and provide solutions to minimize their effects.

Contents

List of Tables

List of Figures

Abbreviations

ADC	Analog-to-digital converter
ASE	Amplified spontaneous emission
AWG	Arrayed waveguide grating
AWGN	Additive white Gaussian noise
B2B	Back-to-back
BER	Bit error rate
BP	Back-propagation
BPG	Bit pattern generator
BS	Backscattering
CAGR	Compound annual growth rate
CE	Conversion efficiency
CO-OFDM	Coherent optical orthogonal frequency-division multiplexing
CP	Cyclic prefix
CR	Clipping ratio
CW	Continuous-wave
DAC	Digital-to-analog converter
DC	Direct current
DDO-OFDM	Direct-detection optical orthogonal frequency-division multiplexing
DFBP	Digital filter back-propagation
DL	Downlink
DMT	Discrete multi-tone
DNL	Differential nonlinearity
DP	Dual polarization
DSB	Double sideband
DSP	Digital signal processing
DWDM	Dense wavelength-division multiplexed
ECL	External cavity laser
EDFA	Erbium-doped fiber amplifier
ENOB	Effective number of bits

EVM	Error vector magnitude
FEC	Forward error correction
FFT	Fast Fourier transform
FPGA	Field programmable gate array
FWM	Four-wave mixing
I	In-phase
IBO	Input power backoff
ICI	Inter-carrier interference
IFFT	Inverse fast Fourier transform
IM	Intensity modulator
IM/DD	Intensity modulation with direct detection
INL	Integral nonlinearity
IP	Internet protocol
LD	Laser diode
LO	Local oscillator
LPF	Low-pass filter
LTE	Long-term evolution
M-QAM	M-ary quadrature amplitude modulation
MAP	Maximum a posteriori
MCM	Multi-carrier modulation
MIMO	Multiple-input multiple-output
MMSE	Minimum mean square error
MZM	Mach-Zehnder modulator
NF	Noise figure
NRZ	Non-return-to-zero
OBPF	Optical bandpass filter
OFDM	Orthogonal frequency-division multiplexing
OFDMA	Orthogonal frequency-division multiple access
OLT	Optical line terminal
ONU	Optical network unit
OOK	On-off keying
OSNR	Optical signal-to-noise ratio
P/S	Parallel-to-serial
PA	Power amplifier
PAPR	Peak-to-average power ratio
PBC	Polarization beam combiner
PC	Polarization controller
PD	Photodiode

PDF Probability density function
PDM Polarization-division multiplexing
PLI Piecewise linear interpolation
PN Phase noise
PON Passive optical network
PR Phase rotation
PRBS Pseudorandom binary sequence
Q Quadrature
QPSK Quadrature phase-shift keying
RI Remodulation interference
RF Radio frequency
RK Runge-Kutta
RK4 Runge-Kutta fourth-order
RK4BP Runge-Kutta fourth-order back-propagation
RTO Real-time oscilloscope
S/P Serial-to-parallel
SBS Stimulated Brillouin scattering
SCR Signal-to-carrier power ratio
SE Spectral efficiency
SER Symbol error rate
SLM Selective mapping
SMF Single-mode fiber
SNR Signal-to-noise ratio
SOA Semiconductor optical amplifier
SP Single polarization
SSB Single sideband
SSBI Signal-signal beat interference
SSPA Solid-state power amplifier
TDM Time-division multiplexing
TIA Transimpedance amplifier
UL Uplink
VNI Visual networking index
VOA Variable optical attenuator
WDM Wavelength-division multiplexing

List of Symbols

h_0	Unsaturated gain exponent
α	Linewidth enhancement factor
P_{sat}	Saturation power
τ_c	Carrier lifetime
L	Loss
I_{bias}	Bias current
$E(t)$	Optical field
$h(t)$	Gain exponent
Δt	Sample time
$x(t)$	Electrical signal field
X_k	Data symbol for k^{th} subcarrier
f_k	Frequency of k^{th} subcarrier
T_s	Symbol time
$A(t)$	Signal amplitude
P_{avg}	Average power
V_π	half-wave voltage
α_d	Modulator backoff parameter
V_d	Modulator driving signal
$g(x)$	Nonlinear response
$\hat{g}(x)$	Piecewise linear interpolation of $g(x)$
κ	Attenuation factor
σ^2	Variance
R_{os}	Oversampling factor
$r(t)$	Received signal after optical-to-electrical conversion
ν	Laser linewidth
$\varphi(n)$	Phase noise
H	Hamming distance
β	Ratio between BER and SER
B	Signal bandwidth
γ	Signal-to-carrier amplitude ratio

A_c	Optical carrier amplitude
f_c	Optical carrier frequency
P	Signal power
G_{amp}	Amplifier gain
κ_{UL}	Uplink backscattering coefficient
κ_{DL}	Downlink backscattering coefficient
A_{LO}	Local oscillator amplitude
N_Q	Number of DAC quantization levels
δ	Distance between two adjacent DAC levels

To my wife Mahlegha,
to my parents,
and to my sister Samira

Acknowledgment

I would like to express special gratitude and appreciation to my supervisor, Leslie Ann Rusch, for her continuous support and guidance during my graduate studies at Université Laval. Her advice on both professional and personal level was invaluable. She gave me the flexibility to explore various research areas and never hesitated in devoting her time to me.

I would like to thank the members of jury, Prof. Sophie LaRochelle, Prof. Maite Brandt-Pearce and Dr. Massimiliano Salsi, for taking the time to read my thesis and for their valuable comments and suggestions.

A very special thanks goes to An Nguyen. He was a true friend for me from whom I learned a lot. His passion for research always inspired me during my studies. I would like to state my gratitude to Chul Soo Park for his guidance in the experiments. His technical experience was truly an invaluable asset. I would also like to thank Ramtin Farhoudi for many fruitful discussions we had.

Many thanks to all members of optical communications group at COPL. I would like to acknowledge Prof. Sophie LaRochelle and Prof. Wei Shi with whom I had the chance to work during my graduate studies.

I had many friends in Quebec City and during my studies, I never felt away from my home. In particular, I would like to thank my old friend Amin and also Peyman and Zahra for all of the joyful moments we had.

Finally, I want to thank my wife and best friend, Mahlegha. I would not have been able to finish my Ph.D. without her endless love and encouragement. My deepest gratitude goes to my family to whom I owe everything.

Foreword

Five chapters of this thesis are based on the material published in journal papers and conferences. I am the main contributor for all of these publications. In the following, the detailed contribution of each co-author is provided.

Chapter 2: S. Amiralizadeh, A. T. Nguyen, C. S. Park, A. Ghazisaeidi, and L. A. Rusch, "Experimental validation of digital filter back-propagation to suppress SOA-induced nonlinearities in 16-QAM", *Optical Fiber Communication Conference*, 2013 [1]. This paper demonstrates efficiency of digital filter back-propagation (DFBP) in suppressing the nonlinear distortions induced by semiconductor optical amplifier (SOA). An Nguyen and Chul Soo Park assisted me in the experiments. Amirhossein Ghazisaeidi provided the SOA simulator. Leslie Rusch was the supervisor. I was responsible for experiments, signal processing and simulations. The paper was written by me and revised by Leslie Rusch.

Chapter 3: S. Amiralizadeh, A. T. Nguyen, and L. A. Rusch, "Error vector magnitude based parameter estimation for digital filter back-propagation mitigating SOA distortions in 16-QAM", *Opt. Express*, vol. 21, no. 17, pp. 20376–20386, 2013 [2]. In this paper, we propose a parameter estimation technique to find the appropriate parameters for DFBP block. An Nguyen assisted me in doing the experiments. Leslie Rusch was the supervisor of the project. I ran the experiments, processed the captured experimental data and performed all simulations. The manuscript was prepared by me and revised by Leslie Rusch.

Chapter 4: S. Amiralizadeh and L. A. Rusch, "Transmitter sensitivity to high PAPR in coherent optical OFDM systems", *Conference on Lasers and Electro-Optics*, 2014 [3]. S. Amiralizadeh, A. T. Nguyen, and L. A. Rusch, "Modeling and compensation of transmitter nonlinearity in coherent optical OFDM", *Optics Express*, vol. 23, no. 20, pp. 26192–26207, 2015 [4]. The papers present a comprehensive investigation of nonlinearities in coherent optical orthogonal frequency-division multiplexing (CO-OFDM) transmitter. In the second paper, we also propose a combination of clipping and predistortion technique to compensate for the nonlinear distortions. I had fruitful discussions with An Nguyen about signal processing methods for CO-OFDM systems. All of the simulations and theoretical analysis were performed by me. Leslie Rusch was the supervisor. The manuscripts were prepared by me and revised by Leslie Rusch.

Chapter 5: S. Amiralizadeh, C. S. Park, and L. A. Rusch, "Experimental study of M-QAM constellation options for short-reach dual-polarization optical OFDM with direct detection", *European Conference on Optical Communication*, 2015 [5]. S. Amiralizadeh, A. Yekani, and L. A. Rusch, "Discrete multi-tone transmission with optimized QAM constellations for short-reach optical communications", *IEEE Journal of Lightwave Technology*, 2016 [6]. In [5], we study symbol error rate (SER) performance of optimized non-square constellations in a short-reach direct-detection optical orthogonal frequency-division multiplexing (DDO-OFDM) system. In [6], we elaborate on our work and investigate bit error rate (BER) performance of the constellations in a short-reach orthogonal frequency-division multiplexing (OFDM) and discrete multi-tone (DMT) system. Chul Soo Park assisted me in preparing the experimental setup. Amin Yekani prepared the Matlab code for DMT power- and bit-loading algorithms. I prepared the Matlab code for finding the optimized constellations, bit-to-symbol mapping and signal processing. I conducted the experiments and processed the captured data. Leslie Rusch was the supervisor. The manuscripts were prepared by me and revised by Leslie Rusch.

Chapter 6: S. Amiralizadeh, A. T. Nguyen, C. S. Park, and L. A. Rusch, "Single-fiber lightwave centralized WDM-OFDMA-PON with colorless optical network units", *Journal of Optical Communications and Networking*, vol. 8, no. 4, pp. 196–205, Apr. 2016. [7]. This paper proposes and experimentally demonstrates a passive optical network (PON) architecture for next-generation optical access networks. An Nguyen and Chul Soo Park assisted me in preparing the experimental setup. I conducted all of the experiments and processed the data afterwards. I also did all of the simulations and analysis. Leslie Rusch was the supervisor of the project. The paper was prepared by me and revised by Leslie Rusch.

Chapter 1

Introduction

1.1 Motivation

There has been a tremendous advance in optical communications since its invention in 80's. This advance is always driven by ever-increasing demand for higher data transmission rates. In recent years, with the emergence of bandwidth-hungry applications like real-time multimedia, long-term evolution (LTE) and cloud services, capacity demand has been increasing exponentially. Cisco visual networking index (VNI) forecasts the growth in Internet protocol (IP) traffic until 2019. As reported in Table 1.1, 23% compound annual growth rate (CAGR) in fixed Internet IP traffic is estimated until 2019. The predicted CAGR is even higher for mobile data traffic [8]. The exponential growth in global IP traffic is more evident in Fig. 1.1 where Cisco VNI predicts 168 exabytes per month of IP traffic in the world by 2019.

Table 1.1: Global IP traffic, 2014–2019 (Petabytes [PB] per Month).

	2014	2015	2016	2017	2018	2019	CAGR (2014–2019)
Fixed Internet	39,909	47,803	58,304	72,251	90,085	111,899	23%
Managed IP	17,424	20,460	23,371	26,087	29,274	31,858	13%
Mobile data	2,514	4,163	6,751	10,650	16,124	24,221	57%

In order to meet the demand for higher bit rates, novel technologies are being developed currently. Different strategies are proposed and demonstrated for the system upgrade; namely increasing the baud rate, exploiting higher-order modulation formats and using dense multiplexing schemes. Higher-order modulation formats have attracted a lot of attention recently as their implementation has become feasible with coherent detection and direct detection.

Advanced modulation techniques enable transmission of multiple bits per symbol and thus, achieve significantly higher spectral efficiencies (SEs) compared to the legacy on-off keying (OOK) systems. Fig. 1.2 shows the SEs demonstrated in the last two decades [9]. High-SE

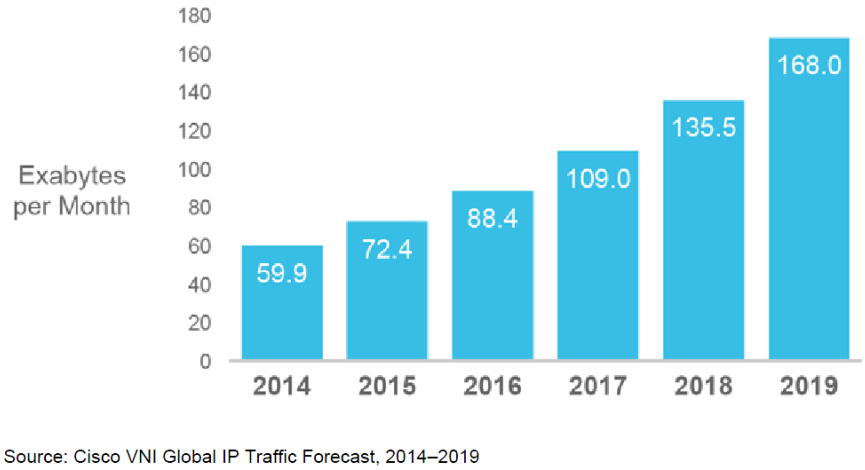

Figure 1.1: Cisco VNI global IP traffic from 2014 to 2019.

modulation formats allow data transmission rates close to single-mode fiber (SMF) capacity limit. SE of 11 b/s/Hz has been achieved recently by using polarization-division multiplexed (PDM) 128-ary quadrature amplitude modulation (128-QAM) coherent optical orthogonal frequency-division multiplexing (CO-OFDM) [10]. The aggregate bit rate was 101.7 Tb/s over 370 dense wavelength-division multiplexed (DWDM) channels.

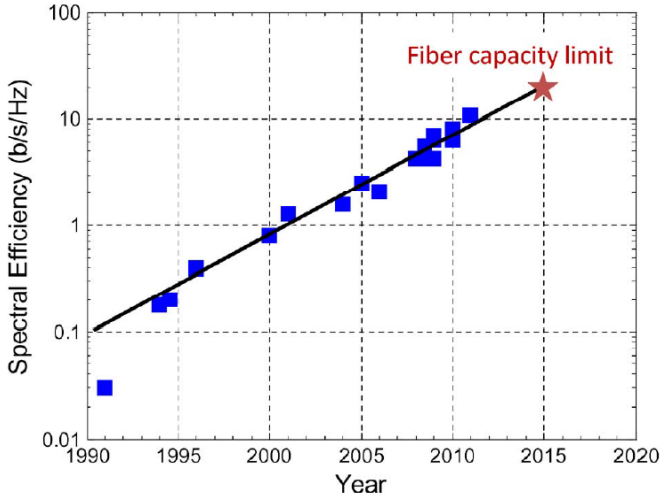

Figure 1.2: Achieved SEs is experiments during last two decades.

In addition to having high SE, advanced modulation techniques take advantage of digital signal processing (DSP) at the receiver. With the development of high-speed digital integrated circuits, impairments of the optical system can be dealt with in the digital domain in a more cost-efficient manner. Replacing the complicated analog electronics with digital circuits not

only improves performance of the system but also reduces cost per bit significantly, making implementation of high-speed advanced optical communication systems feasible.

This motivates the subject of this thesis, where we concentrate on two of the most promising modulation techniques, single-carrier advanced modulation with coherent detection and multi-carrier orthogonal frequency-division multiplexing (OFDM) systems. The main goal of this thesis is proposing and demonstrating efficient algorithms for coping with the impairments of the optical systems using coherent detection and/or OFDM in the context of next-generation optical networks.

1.2 Thesis Outline

The subjects covered in this thesis can be divided into three main parts. In the first part, presented in chapter 2 and chapter 3, we focus on single-carrier coherent optical networks with semiconductor optical amplifier (SOA) at the transmitter as booster amplifier and demonstrate an efficient method for mitigating the SOA nonlinear distortions. In the second part, presented in chapter 4 and chapter 5, we investigate optical networks using OFDM modulation. We propose techniques to improve performance of optical systems using optical OFDM. Third part, presented in chapter 6, is devoted to demonstration of an optical network architecture with direct-detection optical OFDM (DDO-OFDM) for downlink (DL) and CO-OFDM for uplink (UL).

This thesis targets study of optical systems with short/medium reach (below 100 km). Therefore, we neglect fiber nonlinearity in our investigations. We particularly focus on low-complexity solutions to address the cost requirements of next-generation optical networks. We rely on theoretical analysis, Monte Carlo simulations and experiments to demonstrate effectiveness of the introduced techniques.

1.2.1 Part I: SOA nonlinearity mitigation in coherent detection

This part deals with SOA nonlinearity problem in next-generation coherent detection systems. Photonic integrated transceivers are envisioned to meet the requirements of future optical networks with stringent cost requirements. SOAs are essential parts of these transceivers due to their integrability and low cost. However, amplitude and phase distortions induced by SOA degrade performance of the system, particularly in optical systems with advanced modulation formats where both amplitude and phase carry data.

We use a digital back-propagation (BP) scheme at the receiver to compensate for the SOA-induced nonlinearities in coherent detection systems. In chapter 2, we experimentally demonstrate the performance of DFBP technique for mitigating SOA nonlinearities in 16 Gbaud 16-QAM coherent detection system, for the first time. We show that the simpler digital fil-

ter BP (DFBP) method leads to better performance compared to Runge-Kutta (RK) based SOA post-compensation. Performance of DFBP depends on four parameters characterizing the behavior of the SOA used at the transmitter. We vary these parameters and investigate sensitivity of bit error rate (BER) performance to the DFBP parameters.

In chapter 3, we propose a simple, low-overhead algorithm for estimation of DFBP parameters based on error vector magnitude (EVM). The BER achieved with this method is significantly better than SOA characterization method and has negligible penalty as compared to DFBP with fine parameter estimation. We examine different bias currents for two commercial SOAs used in our experiments to find optimum operating points. The coarse parameter DFBP efficiently compensates SOA-induced nonlinearities for both SOA types in 16-QAM coherent detection at 22 Gbaud with 80 km fiber length.

1.2.2 Part II: optical OFDM performance improvement

In the second part, we turn to optical OFDM modulation as a promising technique for implementation of future optical systems. OFDM is a special case of multi-carrier modulation (MCM) in which multiple subcarriers are used to transmit the data. Orthogonality of the subcarriers over one symbol period is the key factor that makes OFDM distinctive from general MCM schemes. Optical OFDM can be implemented via both coherent detection and direct detection.

In CO-OFDM systems, the received signal is detected with a local oscillator (LO) and a coherent receiver. In DDO-OFDM, an optical carrier is transmitted along with the signal to enable direct detection of the received OFDM signal with a single photodiode (PD). DDO-OFDM allows transmission of advanced modulation formats (e.g., high-order QAM) in a cost-efficient manner thanks to its simple receiver design. However, it has less SE and noise tolerance compared to CO-OFDM, since a portion of the transmitted power is devoted to the carrier.

In chapter 4, we propose a combination of clipping and predistortion technique to compensate for the nonlinear distortions induced at the CO-OFDM transmitter. Nonlinearities are introduced by the digital-to-analog converter (DAC), electrical power amplifier (PA) and optical modulator in the presence of high peak-to-average power ratio (PAPR). We quantify the transmitter nonlinearity and introduce parameters to vary the nonlinearity. We use training symbols to extract the transmitter nonlinear function. We show that piecewise linear interpolation (PLI) captures transmitter nonlinearity accurately. We calculate BER in the presence of transmitter nonlinearity and additive white Gaussian noise (AWGN). We use the derived BER to validate the PLI accuracy in characterizing transmitter nonlinearity. The inverse of the PLI estimate of the nonlinear function is used as a predistorter to suppress transmitter nonlinearity. We investigate performance of the proposed scheme by Monte Carlo simulations

in a 16-QAM CO-OFDM system.

In chapter 5, for the first time, we investigate performance of optimized non-square M-QAM constellations in short-reach optical OFDM and discrete multi-tone (DMT) with direct detection. Our demonstration focuses on data center optical networks where low-cost direct-detection schemes are preferred. We obtain optimized constellations by using an iterative gradient-search algorithm. We find bit-to-symbol mappings with a blind search technique for the optimized constellations. Our experiments show that data rate can be improved in OFDM and DMT systems by using optimized constellations instead of square M-QAM.

1.2.3 Part III: experimental PON demonstration

In the last part of this thesis, we experimentally demonstrate a bidirectional lightwave centralized passive optical network (PON) architecture. We focus our attention on the PON implementation and identifying the limiting factors in the PON. The demonstrated PON uses optical OFDM modulation technique due to its flexibility and high SE. We use DDO-OFDM for the DL to allow a simple low-cost receiver at the optical network units (ONUs). For the UL, we use CO-OFDM to enable symmetric data transmission rates owing to performance advantage of coherent detection.

For the proposed PON, we examine two strategies by adjusting the frequency occupancy and the modulation format of the UL and DL signals. We examine the influence of DL signal-to-carrier power ratio (SCR) on performance of both UL and DL via simulations. We identify the impairments peculiar to the PON architecture and present solutions to minimize these impairments.

Our experimental demonstration includes realization of each of the two scenarios investigated. In the first case, a quadrature phase-shift keying (QPSK) OFDM signal with wide spectrum and narrow guard band achieves 21.6 Gb/s. In the second case, a 32-QAM OFDM approach with narrow spectrum and wide guard band achieves 14.5 Gb/s and a span of over 80 km.

1.2.4 Appendices

Five appendices are included at the end of this thesis. Appendix A discusses the parameter variation in SOA post-compensation block using coarse parameter estimation. In Appendix B, we explain the CO-OFDM and DDO-OFDM receiver DSP used in chapter 4, chapter 5 and chapter 6. Appendix C provides the necessary formulas for the theoretical analysis presented in chapter 4. In appendix D, we give the detailed coordinates of the M-QAM constellations used in the OFDM and DMT experiments of chapter 5. Appendix E investigates sensitivity of dual-polarization (DP) DMT performance to variation of optical band-pass filter (OBPF) center frequency. This sensitivity analysis proves that the employed polarization multiplexing scheme in chapter 5 is feasible for practical implementation of short-reach DP DMT systems.

1.3 List of Contributions

In chapter 2, we demonstrate digital filter-based BP for mitigation of SOA-induced nonlinearities via both simulations and experiments. Our contributions in this chapter are:

- First experimental demonstration of DFBP for suppressing SOA nonlinearity.
- Comparison of the performance of DFBP and Runge-Kutta fourth-order BP (RK4BP) in suppressing SOA-induced nonlinear distortions for 16-QAM at 16 Gbaud over 40 km of SMF.
- Analysis of performance sensitivity to variation of the DFBP parameters.

In chapter 3, we propose a simple, low-overhead technique to estimate DFBP parameters in compensating nonlinearity of SOA. The contributions in this chapter include:

- Proposing a novel DFBP parameter estimation method based on EVM monitoring.
- Experimental demonstration of DFBP in 22 Gbaud 16-QAM coherent detection over 80 km of SMF.

In chapter 4, we study CO-OFDM transmitter nonlinearity and propose a predistortion technique combined with clipping to mitigate the transmitter nonlinearities. The contributions in this chapter include:

- Proposing a combination of clipping and predistortion to compensate for OFDM transmitter nonlinearities.
- Proposing a novel transmitter nonlinearity characterization technique based on PLI.

In chapter 5, we propose application of optimized QAM constellations in short-reach direct-detection OFDM/DMT transmission. Our contributions in this chapter are:

- First experimental demonstration of 100 Gb/s+ OFDM/DMT with optimized QAM constellations.
- Investigation of the symbol error rate (SER) and BER performance of the constellations.

In chapter 6, we propose and experimentally demonstrate a bidirectional lightwave centralized WDM-orthogonal frequency-division multiple access (OFDMA)-PON with DDO-OFDM for DL and CO-OFDM for UL. Our contributions in this chapter can be summarized as:

- Experimental demonstration of the PON architecture for two scenarios for the UL and DL signals.
- Identifying impairments limiting the proposed PON performance and investigating their impact in the two scenarios via analysis, simulations and experiments.

Part I

SOA Nonlinearity Mitigation in Coherent Detection

Chapter 2

Experimental Validation of DFBP to Suppress SOA-Induced Nonlinearities

Abstract

This chapter, published in [1], deals with compensating for SOA nonlinear distortions in coherent detection systems. For the first time, we experimentally demonstrate the performance of a computationally efficient DFBP scheme for post-compensating SOA nonlinearities in coherent detection of 16-QAM signals. We examine effectiveness of DFBP via both simulations and experiments. We compare the performance of DFBP with RK-based post-compensation. Our results show that the simpler DFBP technique offers better performance compared to RK4 method. We also experimentally analyze sensitivity of BER performance to variation of DFBP parameters.

2.1 Introduction

Next generation optical communication systems are predicated on systems with integrable components [11]. The nonlinear behavior of SOAs is exploited in recent optical signal processing applications, e.g., wavelength conversion [12, 13], intensity noise suppression [14] and regeneration [15, 16]. Even when used simply for amplification, where nonlinear response is detrimental, SOA integrability along with its wide gain spectrum and cost effectiveness can make them more attractive than erbium-doped fiber amplifiers (EDFAs) [17–22]. The use of SOAs is imperative to compensate insertion loss in integrated transmitters, as shown in [23–25] where an optical modulator is monolithically integrated with a SOA. The SOA nonlinearity can induce amplitude and phase distortions and deteriorate signal quality when used for M-QAM signaling in coherent detection systems [26].

Various post- and pre-compensation schemes have been proposed to overcome the nonlinear effect of SOAs [27–31]. Both approaches rely on creating an inverse SOA to compensate for

the SOA nonlinearity. In pre-compensation, the inverse SOA is applied at the transmitter before the signal is distorted by the SOA, whereas in post-compensation the inverse SOA is implemented at the receiver to deal with SOA distortion. While pre-compensation can be attractive when SOA parameters are known, post-compensation has the ability to blindly adapt itself to unknown SOA parameters.

Digital BP techniques can be employed to overcome the SOA nonlinear effects. In BP technique, a numerical inverse SOA is implemented and the dynamic gain equation is typically solved using the RK4 method [29]. Linearization of the dynamic gain equation allows us to exploit DFBP in place of the computationally expensive RK methods for post-compensating the SOA nonlinearities [27,28]. Simulations show that when the SOA is employed as a booster amplifier, the simpler DFBP technique attains equal if not slightly better performance than RK4BP for realistic sampling rates near the Nyquist rate [27].

In this chapter, we demonstrate efficiency of DFBP for compensating SOA nonlinearities via experiment and simulations by presenting a comprehensive study of BER performance in a 16-QAM system using coherent detection. We show that the less complex DFBP method outperforms RK4BP and can be utilized effectively in advanced modulation systems to obtain a BER less than a forward error correcting (FEC) threshold of 3.8×10^{-3}. We specify regions where DFBP is more efficient by changing the input power of SOA. We examine two different SOAs (linear and nonlinear) and show that without post-compensation, the SOA must be used in light saturation regime where it cannot maintain enough launched power to the fiber. We also examine sensitivity of DFBP to SOA parameters.

2.2 Digital Filter-Based Inverse SOA

We employ the noisy Cassioli-Mecozzi model to predict SOA behavior [32]. We also consider internal loss of the SOA in this model by dividing its waveguide into K sections. Each section includes a gain block, additive amplified spontaneous emission (ASE) noise and a loss block. While K should tend to infinity, we observed $K > 40$ gives indistinguishable results in our simulations. Therefore, we conservatively set $K = 80$ in simulations for "ground truth" SOA output, using the RK4 algorithm to solve the propagation equations. To extract the SOA forward-propagation parameters, we plot average gain versus average input power of SOA using experimental measurements and then find the best fit simulation of this curve by changing SOA parameters in the simulations.

For BP, we implement the inverse SOA by reversing the sign of the internal loss and gain exponent in the SOA model. We also use a lower value of $K = K_{inv}$ to reduce BP complexity [27]. We use RK4BP to refer to application of the conventional RK4 algorithm and DFBP to indicate BP realized by solving the linearized dynamic gain equation. For the inverse SOA, we use the parameters that give best BER instead of finding similar gain curves for simula-

tions and experiment. In chapter 3, we express DFBP equations in more detail and propose a computationally efficient approach to find the DFBP parameters. This would introduce more flexibility to the BP by eliminating the requirement for SOA characterization. Table 2.1 indicates the parameters used to compensate via BP. Following this approach, the DFBP method can also lend itself to an adaptive filter version when we adaptively set the BP parameters. This could be interesting for elastic networks, network hops and other applications in which the channel is dynamic.

Table 2.1: Applied parameters for BP pertaining to each SOA.

	Linear SOA ($I_{bias} = 200\,\text{mA}$)			Nonlinear SOA ($I_{bias} = 200\,\text{mA}$)	
BP algorithm - K_{inv}	DFBP-1	DFBP-10	RK4BP-10	DFBP-1	DFBP-10
Unsaturated gain exponent, h_0	3.2	4.2	4.2	6	7.6
Linewidth enhancement factor, α	4	4	4.5	4.4	4.4
Saturation power, P_{sat} (dBm)	3.5	6	7	8.8	9.7
Carrier lifetime, τ_c (ps)	120	110	110	80	80
SOA loss, L (dB)	0	4.9	4.9	0	5.6

2.2.1 Experimental setup

Fig. 2.1 shows the experimental setup for 16 Gbaud 16-QAM coherent detection system. At the transmitter, an external cavity laser (ECL) at 1550 nm with less than 100 kHz linewidth is modulated using an in-phase/quadrature (I/Q) modulator. Each of the Mach-Zehnder modulators (MZMs) is driven by 4-level electrical signals obtained by combining two decorrelated non-return-to-zero (NRZ) $2^{11}-1$ pseudorandom binary sequences (PRBSs) at 16 Gbaud. The resulting 16-QAM signal is then amplified using either a linear Kamelian or nonlinear CIP SOA with noise figure of 7 dB and 8.4 dB, respectively. The injected current of the SOAs was fixed at 200 mA to maintain the same power consumption. We change the input power of the SOAs, P_{in}, using a variable optical attenuator (VOA) to examine the performance of the system for different saturation levels. The signal is launched into 40 km of standard SMF and filtered by a 1-nm optical band-pass filter with 3 dB loss at the demultiplexer to remove the out-of-band ASE noise. A polarization controller (PC) is employed after the demultiplexer to maximize the received power onto one polarization of the coherent receiver.

At the receiver, we coherently detect the signal using a tunable laser with output power of 9.5 dBm as LO. The obtained in-phase and quadrature electrical signals are then digitized using two-channels of an 80-GS/s real-time oscilloscope (RTO). We then perform off-line DSP using the captured data. In the DSP, we apply an anti-aliasing filter, compensate for chromatic dispersion and perform clock recovery. We then numerically amplify the signal so that it will have the same power as the SOA output (i.e. power launched into the fiber). We compensate for SOA-induced nonlinearities using DFBP (or RK4BP) algorithm. Afterwards, we perform

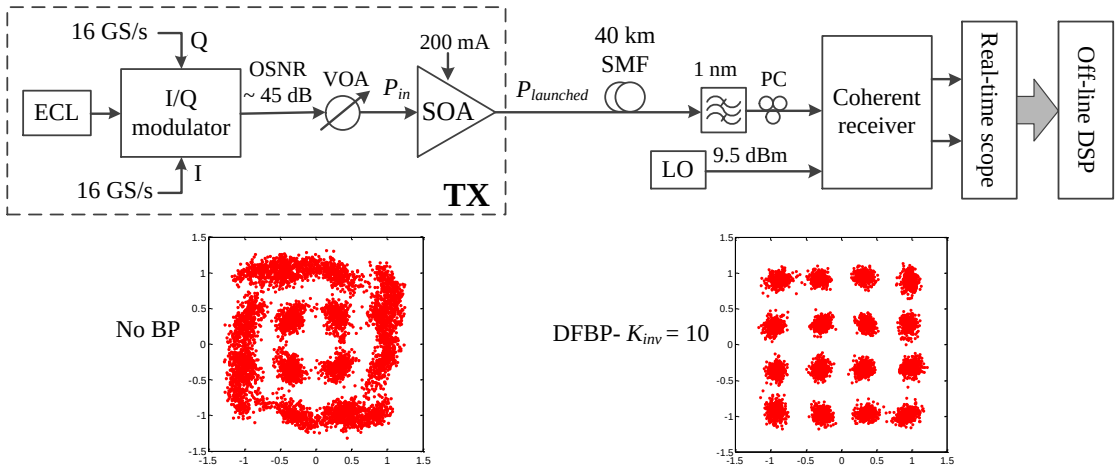

Figure 2.1: Experimental setup for 16-QAM 16 Gbaud single-channel coherent detection system using SOA as power booster at the transmitter.

frequency offset estimation [33] and phase recovery using decision directed algorithm [34]. In order to compensate for the front end low-pass filtering effect, we employ a minimum-mean-square error (MMSE) equalizer. In agreement with [26], we observed that the linear MMSE filter has no contribution in compensating SOA nonlinearities. Finally, we make a symbol decision for maximum a posteriori (MAP) detection in AWGN, i.e., choose the closest symbol to the received I/Q coordinates after BP. In the inset of Fig. 2.1, we show an example recovered constellation with and without compensating nonlinearities for the linear SOA when $P_{in} = -11.8\,\text{dBm}$.

2.2.2 Experimental and simulation results

We varied the input power of the SOA to examine BP performance for different SOA saturation levels. In Fig. 2.2(a), we show BER versus P_{in} for both experiment and simulation with $K_{inv} = 10$ for the linear SOA. Simulations yield the same behavior as experimental results. We observe that both BP techniques reduce BER to less than FEC threshold of 3.8×10^{-3}. However, the less complex method of DFBP outperforms RK4BP by giving 2 dB more dynamic range and lower BER floor. We also specify the light saturation and deep saturation regimes of SOA regarding its input power. The DFBP method can be applied efficiently when SOA is deeply saturated to achieve a BER less than FEC limit. Fig. 2.2(b) shows the BER versus launched power, $P_{launched}$, experimental results of DFBP for both linear and nonlinear SOA when $K_{inv} = 1$ and 10. The results demonstrate that DFBP scheme gives the same performance for $K_{inv} = 1$ and 10 when using either a linear SOA or high-gain nonlinear SOA. Therefore, we can reduce complexity significantly by using one, instead of 10, inverse SOA block. We notice the receiver noise is limiting system performance for low launched powers, where SOA is lightly saturated, and severe nonlinearity restricts the performance in high pow-

ers, where SOA is in deep saturation regime. As a result, BP is inevitable to have enough launched power in the system.

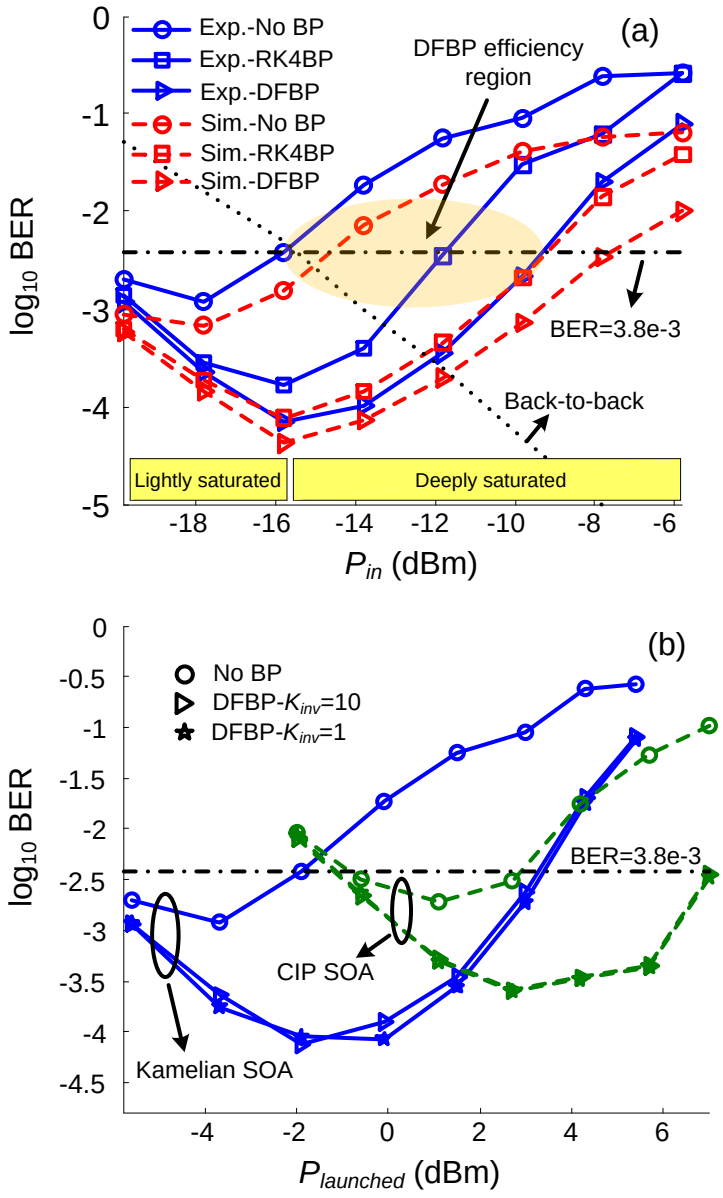

Figure 2.2: (a) BER results for different input powers of linear SOA with $K_{inv} = 10$. Sim.: simulation, Exp.: experiment, (b) Measured BER for different launched powers to the fiber (SOA output power).

In Fig. 2.3 and Fig. 2.4, we assume $P_{in} = -11.8\,\text{dBm}$ and $-18.5\,\text{dBm}$ for linear and nonlinear SOA, respectively, and examine the performance sensitivity to DFBP parameters when $K_{inv} = 1$. We fix three of the SOA parameters at their optimal value, as reported in table 2.1, and vary the fourth parameter to see its impact on BER in Fig. 2.3(a) and Fig. 2.3(b). It

must be noted when $K_{inv} = 1$, there is no loss block in the inverse SOA, i.e., $L = 0\,\text{dB}$. The results indicate that DFBP performance has a very low sensitivity to h_0. In addition, 10 % variation of the other parameters has minor impact on BER.

Finally, we consider 1000 different parameter sets chosen randomly over a uniform distribution in the intervals specified at inset of Fig. 2.4(a) and Fig. 2.4(b) and calculate BER for each of them. We observe that BER is still below FEC limit of 3.8×10^{-3} in Fig. 2.4(a) and Fig. 2.4(b). The results suggest that coarse estimation of parameters gives reliable BER performance for DFBP.

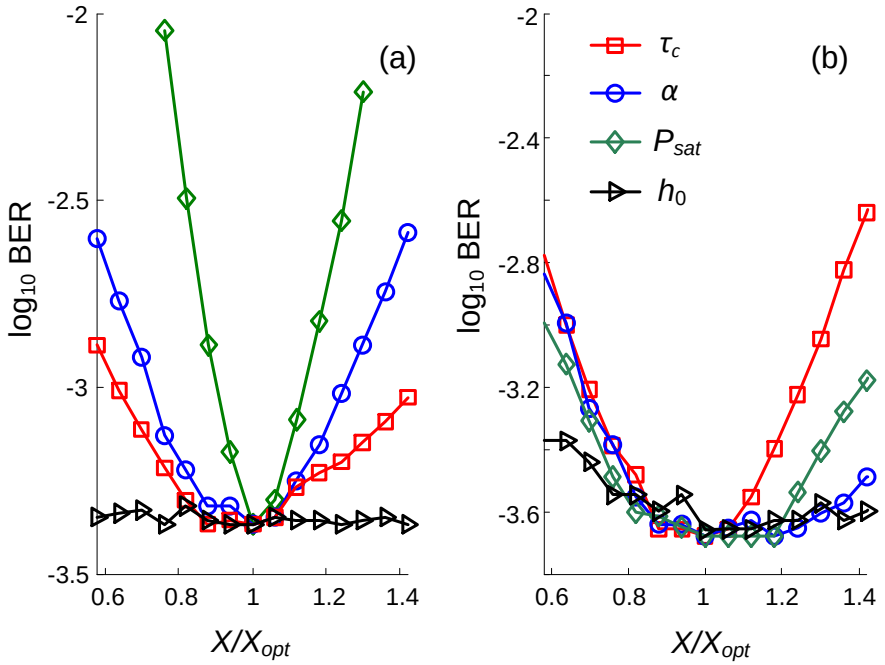

Figure 2.3: DFBP parameters sensitivity analysis using experimental data when $K_{inv} = 1$. (a) nonlinear SOA, (b) linear SOA.

2.3 Conclusion

We experimentally demonstrated the DFBP method efficiency to mitigate SOA nonlinearities in deep saturation regime for coherently detected 16-QAM system at 16 Gbaud. Our experimental and simulation results show the less complex DFBP algorithm gives better performance compared to the conventional RK4BP method. We further reduced the complexity by using DFBP with one inverse gain block ($K_{inv} = 1$). We performed DFBP parameters sensitivity analysis and verified that BER is below FEC threshold of 3.8×10^{-3} even with the coarse estimation of DFBP parameters. This suggests feasibility of coarse parameter allocation for DFBP block.

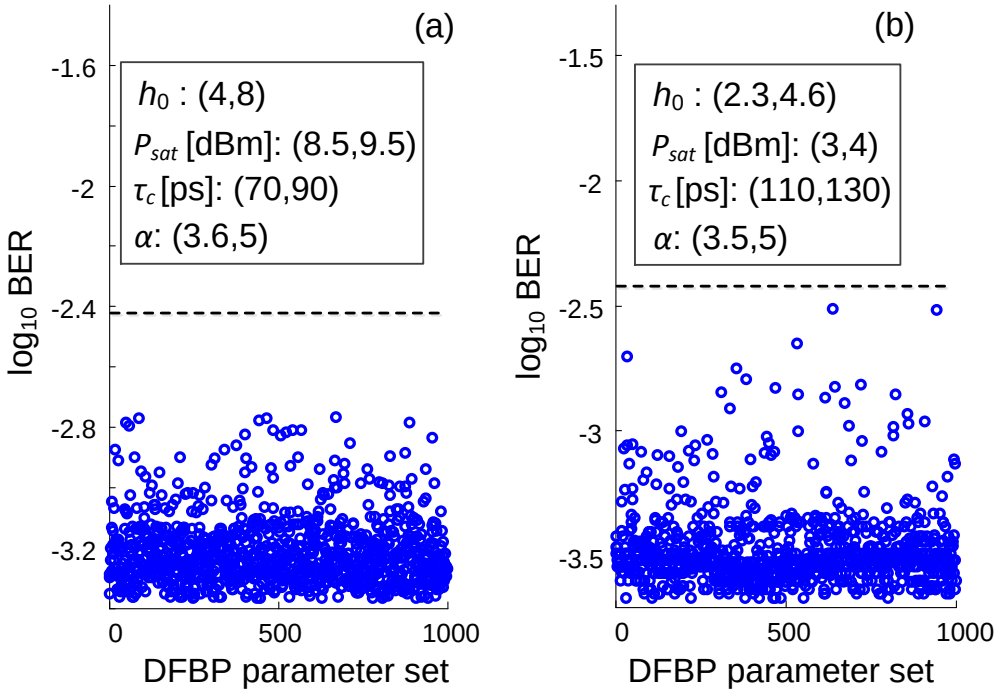

Figure 2.4: Performance variation of the system with random DFBP parameters for $K_{inv} = 1$. (a) nonlinear SOA; Inset: DFBP parameter range (b) linear SOA; Inset: DFBP parameter range.

Our results in this chapter establishes efficiency of DFBP method in suppressing SOA-induced nonlinearities. DFBP is particularly attractive in optical networks where application of cost-effective integrable SOAs is preferred to EDFAs in end-users. Implementation of DFBP increases the link budget for optical networks and allows longer system reach. In the next chapter, we turn our attention to practical implementation aspects of DFBP technique. We investigate DFBP parameters and propose a simple parameter adaptation method based on EVM to facilitate its realization. We also investigate higher data transmission rates compared to this chapter (22 Gbaud vs. 16 Gbaud) to further comply with the high capacity requirement of next-generation optical networks.

Chapter 3

EVM Based Parameter Estimation for DFBP

Abstract

In this chapter, published in [2], we investigate the performance of DFBP using coarse parameter estimation for mitigating SOA nonlinearity in coherent communication systems. We introduce a simple, low-overhead method for parameter estimation for DFBP based on EVM as a figure of merit. The BER achieved with this method has negligible penalty as compared to DFBP with fine parameter estimation. We examine different bias currents for two commercial SOAs used as booster amplifiers in our experiments to find optimum operating points and experimentally validate our method. The coarse parameter DFBP efficiently compensates SOA-induced nonlinearity for both SOA types in 80 km propagation of 16-QAM signal at 22 Gbaud.

3.1 Introduction

In chapter 2, a computationally efficient DFBP technique is employed to post-compensate nonlinear effects of SOAs. At practical sampling rates, DFBP was shown in simulations and in experiments to outperform the more complex RK based method. The simplicity of DFBP stems from a linearized SOA dynamic gain equation used in its derivation. The complexity of DFBP can be further reduced by using one inverse gain block instead of multiple blocks; this was shown to provide good compensation in chapter 2. In this chapter, we use a method to determine DFBP parameters without a characterization of the SOA. Indeed, we find parameters that are more effective in removing distortion than parameters based on knowledge of the transmitter SOA.

We propose a simple, low-overhead method to optimize DFBP parameters. We used the EVM as a figure of merit for the optimization (as opposed to BER) to reduce complexity. We

further propose a strategy to reduce the search space for optimal parameters, and show that coarse resolution can achieve compensation on a par with a computationally expensive search over a space with fine resolution. We demonstrate the efficiency of this technique in DFBP adaptation via both experiment and simulations. We examine SOAs designed for both linear and nonlinear performance. We determine the operating point of each SOA to obtain high gain while staying in a regime where post-compensation is effective. We target BER below FEC threshold of 3.8×10^{-3} with 7% overhead. We investigate the propagation performance by including up to 80 km of fiber to the system.

3.2 EVM Based Parameter Estimation of DFBP

The efficiency of DFBP for post-compensating SOA nonlinearities in coherent communication systems was investigated via both simulations and experiments in chapter 2. DFBP parameters were shown to play an important role in post-compensation performance. These parameters can be determined in one of two ways. In the first case the SOA can be characterized experimentally, e.g., the parameters can be inferred for the SOA gain and conversion efficiency (CE) curve [27, 35]. The second method is to sweep the parameters, choosing those resulting in the best BER—an approach taken in the previous chapter. From a mathematical standpoint, and assuming only linear impairments and AWGN, performance should be similar.

The nature of post-compensation is, however, that the source of the nonlinearity is remote from the signal processing. The optical and electrical systems in the link will introduce various impairments, as will the DSP algorithms used for filtering, dispersion compensation and retiming before post-compensation can be applied. The accumulation of these effects will change the nature of the SOA-induced distortion, making the use of parameters gleaned from the SOA characterization less likely to be effective. Sweeping the parameter set to minimize BER yields better results. The parameter set essentially characterizes the overall channel, including but not limited to the SOA.

The structure of the DFBP was derived from SOA dynamics and is effective in combating the nonlinear transfer of intensity noise into phase noise (PN), even though parameters used for the inverse SOA may differ from parameters for the physical SOA at the transmitter. Therefore we retain the parameter set of the physical SOA model, and propose a new methodology for fixing values in that set. In section 3.2.1, we describe that parameter set for the SOA and relate them to the DFBP implementation. In section 3.2.2, we define our strategy for searching for the optimal parameter set. We propose to reduce the search space based on SOA characteristics and previous experimental observations, and motivate the use of EVM as a figure of merit for optimization. In section 3.2.3, we present parameters obtained by characterizing SOAs in our lab that are used in simulations. These parameters are also applied in BP to compare the performance with our proposed method based on coarse estimation of parameters. In

section 3.3, these techniques will be applied in an experimental demonstration.

3.2.1 DFBP parameters

The DFBP method is predicated on inversing the transmitter SOA behavior. The SOA model and the parameters capturing SOA behavior in forward propagation are critical for DFBP. The relationship between SOA input and output fields is given by [36]

$$E_{SOA,out}\left(t\right) = E_{SOA,in}\left(t\right) e^{\frac{1}{2}(1-j\alpha)h(t)}, \tag{3.1}$$

where $E_{SOA,in}(t)$ and $E_{SOA,out}(t)$ are respectively the SOA input and output fields, α is the linewidth enhancement factor and $h(t)$ represents the gain exponent or integrated material gain. The following SOA dynamic gain equation can be solved to find $h(t)$:

$$\tau_c \frac{\mathrm{d}h\left(t\right)}{\mathrm{d}t} = h_0 - h(t) - \left(e^{h(t)} - 1\right) \frac{\left|E_{SOA,in}(t)\right|^2}{P_{sat}}, \tag{3.2}$$

where h_0, P_{sat} and τ_c are the unsaturated gain exponent, the saturation power and the carrier lifetime, respectively. Therefore, knowledge of h_0, α, P_{sat} and τ_c enables us to model the relationship between the SOA input and output fields. These four values are the parameter set describing SOA behavior and those needed to implement the DFBP. The input power $\left|E_{SOA,in}(t)\right|^2$ can be easily measured.

The DFBP is developed from a linearized version of the gain equation (3.2) to reduce complexity [27, 28]. In this approach, $h(t)$ is assumed to be equal to the sum of the average gain exponent and zero-average fluctuations, i.e., $h(t) = \bar{h} + \delta h(t)$. Using the following static gain equation, $\bar{h}$ can be found

$$-h_0 - \bar{h} = \left(e^{\bar{h}} - 1\right) \frac{\left|E_{SOA,in}(t)\right|^2}{P_{sat}}, \tag{3.3}$$

where the negative sign of h_0 is introduced to implement an "inverse SOA". Let Δt be the sampling period, which is equal to symbol time since the DFBP input signal is one sample per symbol in our implementation (oversampling factor = 1). As shown in the DFBP block diagram in Fig. 3.1, we find the zero-average fluctuations, $\delta h(t)$, using a digital filter which is derived from the linearized SOA model by taking z-transform [27]. For convenience we define two parameters, c_1 and c_2, from the SOA parameter set and the easily measured input power $\left|E_{SOA,in}(t)\right|^2$ via

$$c_1 = \frac{1 - e^{\bar{h}}}{1 + \frac{\left|E_{SOA,in}(t)\right|^2 e^{\bar{h}}}{P_{sat}}} \cdot \frac{\Delta t}{\Delta t + \tau_{eff}}, \tag{3.4}$$

$$c_2 = -\frac{\Delta t - 2\tau_{eff}}{\Delta t + 2\tau_{eff}}, \tag{3.5}$$

where

$$\tau_{eff} = \frac{\tau_c}{1 + \frac{\left|E_{SOA,in}(t)\right|^2 e^{\bar{h}}}{P_{sat}}}. \tag{3.6}$$

Having found $h(t)$, the compensated output is found by multiplying the input by $e^{\frac{1}{2}(1-j\alpha)h(t)}$.

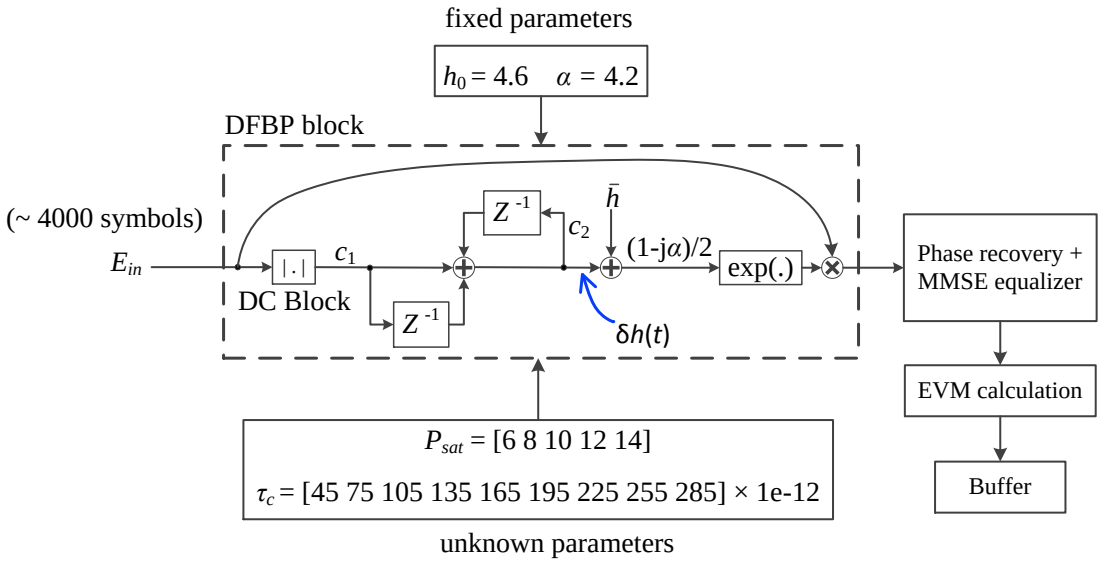

Figure 3.1: Block diagram of coarse estimation method for DFBP. Unsaturated gain exponent (h_0) and linewidth enhancement factor (α) are fixed. Saturation power (P_{sat}) and carrier lifetime (τ_c) are estimated by 4000 training symbols based on EVM performance.

3.2.2 DFBP parameter estimation

The previous section presented the equations used in the DFBP exploiting knowledge of h_0, α, P_{sat} and τ_c. In the previous chapter, our sensitivity analysis showed that DFBP performance is almost independent of h_0. Therefore we set h_0 at a typical value of 4.6. In our experimental examination of both linear and nonlinear SOAs there is little variation in α and we fix it at $\alpha = 4.2$. With two of the parameters fixed, the DFBP performance now mainly depends on P_{sat} and τ_c.

Our objective is to select the remaining two parameters to minimize the BER. Simulation of BER can be computationally costly and requires use of training sequence (i.e., knowledge of bits transmitted). The EVM is known to correlate well with BER at reasonable signal-to-noise ratio (SNR) levels and is given by [37]

$$\text{EVM} = \frac{1}{N_t}\sum_{i=1}^{N_t}|S_i - S_{0,i}|^2\,, \tag{3.7}$$

where S_i, $S_{0,i}$ and N_t are received symbol, ideal constellation point for received symbol and number of randomly transmitted data, respectively. The EVM figure of merit does not require knowledge of transmitted bits thus enabling blind adaptation. We propose the use of EVM for optimization of P_{sat} and τ_c in a computationally simple manner and show via simulation and experiment that such an optimization leads to significant BER improvement.

As indicated in Fig. 3.1, we capture a block of received samples (4000 symbols) to be used for finding the optimal parameter set. We apply noise filtering, dispersion compensation (if necessary) and retiming on the captured data. To implement the DFBP, we use fixed values of h_0, α and search over 45 possibilities for (P_{sat}, τ_c), i.e., 9 for τ_c and 5 for P_{sat} as shown in Fig. 3.1. Our spread of values (P_{sat}, τ_c), covers a wide gamut of possibilities for linear and nonlinear SOAs. One might limit them having knowledge about SOA parameters. For each pair, the DFBP block compensates for SOA nonlinearity. We then perform phase recovery and MMSE equalization for those 4000 symbols and calculate EVM. At the end, we choose the parameter pair corresponding to minimum EVM.

While we searched all 45 parameter pairs, optimization methods, e.g. gradient descent, can be used to find the pairs giving minimum BER. When SOA parameters are fairly constant the computational burden of a complete search is acceptable. For applications where DFBP parameters need to be tuned regularly optimization methods could reduce latency. In this work, however, we focus on simplifying parameter estimation for DFBP to compensate SOA nonlinearity efficiently and examine the size of the search space.

3.2.3 SOA characterization

In the previous section we proposed a method to find the optimized parameters for DFBP. Although this estimation technique does not require information on the SOA at the transmitter, SOA characterization allows us to have more precise simulations which can be used to verify the experimental results. In addition, we also apply parameters from characterization of the SOA directly in the DFBP to contrast performance testing the two parameter extraction methods.

We use the simulator presented in [32] and consider a SOA waveguide as cascade of K small sections for greater accuracy. The SOA distributed loss and ASE is included in this model. The propagation equations are solved using RK4 algorithm when $K = 80$ as "ground truth". For BP, we set $K = 1$ (one inverse gain block) to reduce complexity. In chapter 2, it has been shown this causes minimal penalty.

Table 3.1 indicates the parameters extracted by characterization of the two SOAs used in our experiments. We examined two commercial SOAs with differing design objectives; the first stresses gain and linearity (linear Covega BOA-2679 or L-SOA with noise figure of 7.3 dB), while the second enhances the nonlinear response for optical signal processing applications (nonlinear CIP-NL-OEC-1550 or NL-SOA with noise figure of 8.4 dB). We varied the three parameters h_0, P_{sat} and L (SOA loss) and fitted them to the average gain versus SOA input power curve. To extract the remaining two parameters, α and τ_c, we measured CE for four-wave mixing (FWM) in SOAs as a function of frequency detuning. We compared the theoretical curve of CE versus frequency detuning with experimental results, and varied α

and τ_c to find a good fit between the two curves [35].

Table 3.1: Applied parameters in simulations and BP pertaining to each SOA.

	L-SOA ($I_{bias} = 400\,\text{mA}$)		NL-SOA ($I_{bias} = 160\,\text{mA}$)	
Parameter	$K = 80$	$K = 1$	$K = 80$	$K = 1$
Unsaturated gain exponent, h_0	6.7	6	7.2	6.5
Linewidth enhancement factor, α	4	4	3.8	3.8
Saturation power, P_{sat} (dBm)	9.7	9.2	8.4	7.6
Carrier lifetime, τ_c (ps)	275	275	190	190
SOA loss, L (dB)	2.9	0	3.1	0

3.3 Experimental Setup

In this section we take the techniques laid out in section 3.2 and validate them experimentally. Our investigation includes back-to-back (B2B) measurements as well as propagation for up to 80 km. Please note that while our transmitter is constructed from discrete components for experimental convenience, DFBP for post-compensation targets integrated transmitter sources with a SOA booster stage, or other subsystems (e.g., wavelength converters) where SOAs may be operated in saturation.

Fig. 3.2 shows the experimental setup. An ECL source with less than 100 kHz linewidth is used at 1550 nm. Each of two 22-Gbaud 4-level electrical signals is obtained by combining two $2^{20} - 1$ PRBSs. These signals form the 16-QAM signal set that drives the I/Q Mach-Zehnder external modulator (SHF 46213D). The SOA is used in a booster configuration at the transmitter to increase launched power. The 1-nm OBPF after the SOA has 3.8 dB loss, and limits ASE.

We performed our experiment in two different configurations. In configuration (A) we examine B2B performance with the SOA present. In configuration (B) the signal is launched through 80 (or 60) km of standard SMF with 0.19 dB/km loss. The received optical SNR (OSNR) is adjusted using a VOA and an EDFA. After a PC, a VOA adjusts the received power to -7 dBm for configuration (A) and -10 dBm for configuration (B). The LO was a narrow linewidth ECL with 14 dBm output power. We used these values for LO and receiver input power to operate the coherent receiver at its optimum working regime.

After coherent detection with a 22-GHz integrated coherent receiver, the signal is digitized using two channels of a commercial 80-GS/s RTO with 30 GHz bandwidth. Signal processing is performed offline on 2 million captured samples. In the DSP, we apply a Gaussian low-pass filter and do dispersion compensation, if needed. We then perform resampling and timing recovery. Afterwards, we numerically boost the signal power to its inferred value at the SOA output and utilize the DFBP method to post-compensate the SOA-induced non-

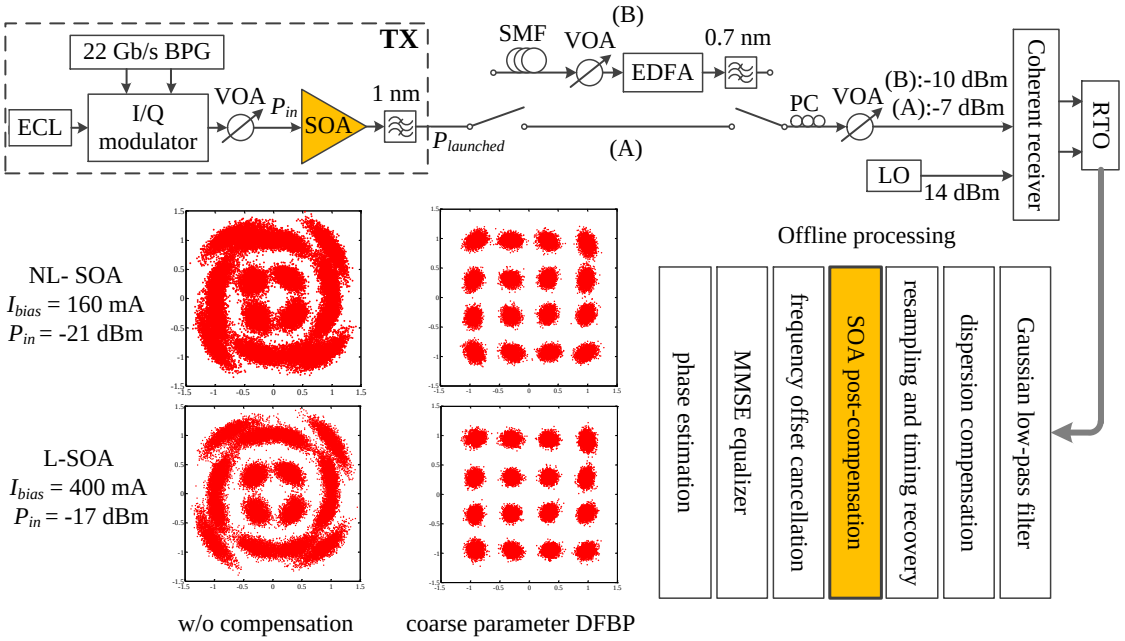

Figure 3.2: Experimental setup for 22-Gbaud 16-QAM single-channel coherent detection system. SOA is used at transmitter to obtain higher launched power. Post-compensation block is added in the DSP part to mitigate nonlinearity induced by SOA. In configuration (B), 80 (or 60) km of SMF is added and ASE noise loading is employed to adjust OSNR comparing to (A). The inset illustrates efficiency of coarse parameter DFBP for compensating nonlinearity induced by each of the two SOAs utilized in our experiment. BPG: bit pattern generator.

linearity. We remove the frequency offset between the LO and the received signal using the estimator suggested in [33]. We apply an MMSE filter to mitigate the effect of limited receiver bandwidth. We then employ a decision-aided maximum likelihood algorithm to estimate the carrier phase [34]. Finally, we choose the closest symbol to the received I/Q coordinates from 16-QAM constellation and carry out symbol-to-bit mapping. We synchronize to the transmitted PRBS, count errors and estimate BER. The signal constellations for two SOAs are shown as an inset in Fig. 3.2. The amplitude and phase distortions deteriorate signal performance, nevertheless, application of coarse parameter DFBP leads to recovery of the 16-QAM signal.

3.4 Experimental and Numerical Results

In our first set of results, we show the effect of the induced nonlinearity on BER when varying SOA input power and applying different bias currents to specify a suitable working point for each SOA. We devote the second subsection to comparing the performance of the proposed DFBP with parameters optimized over the discrete parameter set (Fig. 3.1) to a DFBP whose parameters were optimized over the same range of values, but with much greater granularity. Having the appropriate working conditions, we concentrate on the results from configuration

(B) to find the OSNR penalty due to application of SOA as compared to the B2B case for which we have no SOA and fiber. By transmitting the distorted signal from SOA over a certain length of fiber, it is expected to experience degradation of performance comparing to results from first subsection due to interaction between SOA nonlinearity and effects originated from transmission, e.g., dispersion. Therefore, in choosing suitable operating points for the SOAs, sufficient distance of BER from the FEC limit was targeted.

3.4.1 Appropriate SOA operating condition

We change the input power to the SOA in configuration (A) of the experimental setup and examine system performance for different SOA saturation levels. The BER versus launched power, $P_{launched}$, for NL-SOA and L-SOA are presented in Fig. 3.3(a) and Fig. 3.3(b), respectively. We observe significant improvement ($\sim 6\,\mathrm{dB}$) in launched power to the fiber when applying DFBP to mitigate nonlinearity for both SOAs. As expected, with higher bias currents, the SOA gives more gain which in turn leads to higher launched powers. The performance is, however, limited due to severe nonlinearity.

In Fig. 3.3(a), the launched power is 1 dB less for $I_{bias} = 160\,\mathrm{mA}$ as compared to launched powers for $I_{bias} = 250\,\mathrm{mA}$ and 300 mA. Although BER less than a FEC limit of $3.8 \times 10{-}3$ is achievable for all three examined bias currents, we choose $I_{bias} = 160\,\mathrm{mA}$ as a good working point for two reasons. First, the BER distance from the FEC limit is more reliable for this case and second, the SOA power consumption is less for lower bias currents. We show the gain versus bias current of the CIP nonlinear SOA as an inset to demonstrate that the obtained gain decreases quickly for currents below around 160 mA. Therefore, $I_{bias} = 160\,\mathrm{mA}$ is a good compromise between gain and performance. As shown in Fig. 3.3(b), the difference between launched power for $I_{bias} = 400\,\mathrm{mA}$ and 600 mA is 1 dB for the linear Covega SOA, as well. Therefore, we select $I_{bias} = 400\,\mathrm{mA}$ as operating point for the Covega SOA considering above the previously mentioned reasons, and especially to lower power consumption. Simulation results for the selected bias currents are shown with diamond makers for both SOAs in Fig. 3.3 verifying the experimental results for coarse parameter DFBP. As mentioned in section 3.2.3, forward propagation parameters for SOA in simulations are adjusted using the information from SOA characterizations.

3.4.2 Coarse vs. fine parameter estimation

We have already mentioned that parameters h_0 and α either vary little among SOAs or have little impact on the DFBP improvement. The parameters P_{sat} and τ_c, however, vary over wide ranges and DFBP performance is sensitive to these values. For instance, we observed that for our SOAs, P_{sat} can vary from 6 to 14 dBm, while τ_c can vary from 45 to 285 ps. This large search area can be examined in a brute force manner with fine resolution (0.2 dB steps for P_{sat} and 5 ps steps for τ_c), or a reduced search area can be adopted to decrease the delay and

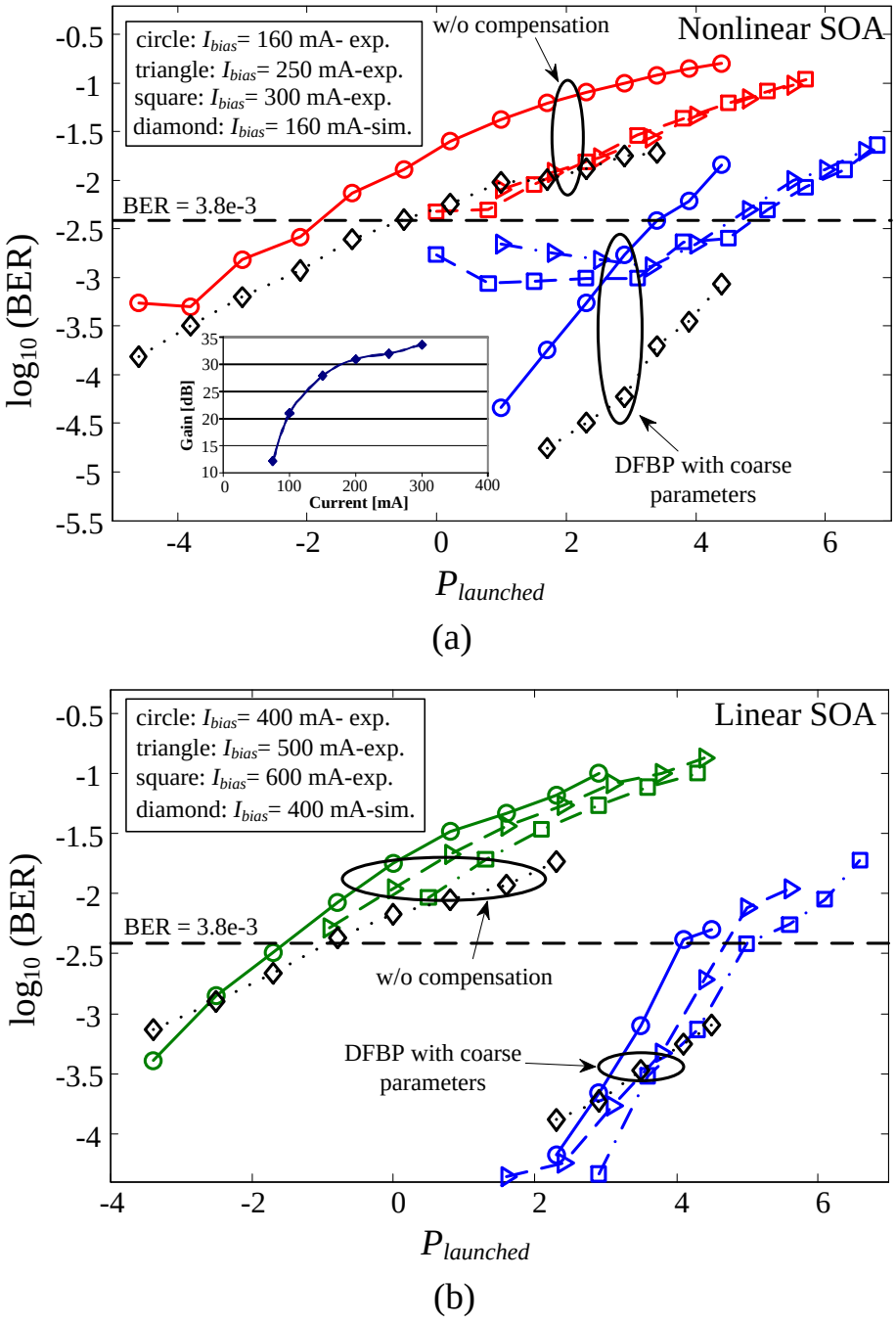

Figure 3.3: BER versus launched power to the fiber without compensation and with coarse parameter DFBP for different SOA bias currents. (a) Nonlinear SOA. The inset shows gain versus SOA bias current. (b) Linear SOA. sim.: simulations, exp.: experiment. Higher SOA bias current leads to more gain and higher launched power, but degrades performance due to increased nonlinear distortions induced by the SOA.

computational overhead for parameter estimation. We examine experimentally the impact of using a coarse resolution (5 values for P_{sat} and 9 values for τ_c) for estimation.

We captured over 1 million symbols per SOA input power level to compare the performance of EVM-optimized coarse parameter estimation vs. BER-optimized, fine parameter estimation. In the first case, we examine only 4000 symbols and find P_{sat} and τ_c (examining 45 pairs) that minimizes the EVM for those symbols. We then take the EVM optimized P_{sat} and τ_c and find the BER over the entire captured data set. In the second case, we take all captured data and minimize the BER by examining in turn a total of ~ 300 pairs of values for P_{sat} and τ_c. The same captured data is used in both cases. We repeated the procedure for each SOA type examined.

The BER versus input power of SOA is reported in Fig. 3.4. Results are given for the nonlinear NL-SOA (160 mA bias current) and for the L-SOA (400 mA bias current). BER for the DFBP found with EVM optimization using coarse resolution is given with circle markers, while results for the DFBP found with BER optimization using fine resolution are given with triangle markers. In addition, the results for parameters attained by SOA characterization are shown with square markers. For both SOA types, we see negligible BER degradation when using the simpler, less computationally expensive EVM based optimization. In Appendix A, variation of parameters estimated by coarse DFBP versus parameters measured by characterization is discussed.

Our demonstration establishes that post-compensation can be applied without use of a training sequence, and with minimal delay and computation. However, when using the parameters obtained by SOA characterization, we observe significant performance degradation especially for L-SOA. These results suggest that, in contrast to our proposed method, parameters given by measurement do not guarantee efficient compensation. The degradation stems from two effects: first, the SOA operating point for characterization and for coherent detection are in most cases different and second, the accumulation of various effects during transmission, e.g. dispersion and filtering effect, are not captured during characterization of SOA parameters.

In Fig. 3.5 we report the sensitivity of BER to variations of parameters P_{sat} and τ_c. We sweep these parameters with fine resolution (0.2 dB for P_{sat} and 5 ps for τ_c), calculating the BER for each parameter pair. The search space is chosen to have BER contours fall in the region of the FEC limit. Fig. 3.5(a) corresponds to the nonlinear NL-SOA, while Fig. 3.5(b) gives results for the linear L-SOA. The plots are reported for $P_{in} = -19$ dBm and -13 dBm for NL-SOA and L-SOA, respectively. The dark central section of the contour represents BER performance well below the FEC threshold. The points highlighted correspond to the EVM optimized parameters found.

Consider the EVM based search space: P_{sat} between 6 dBm and 14 dBm, and τ_c between 45 ps and 285 ps. We can see that this parameter space clearly covers the BER range of interest—

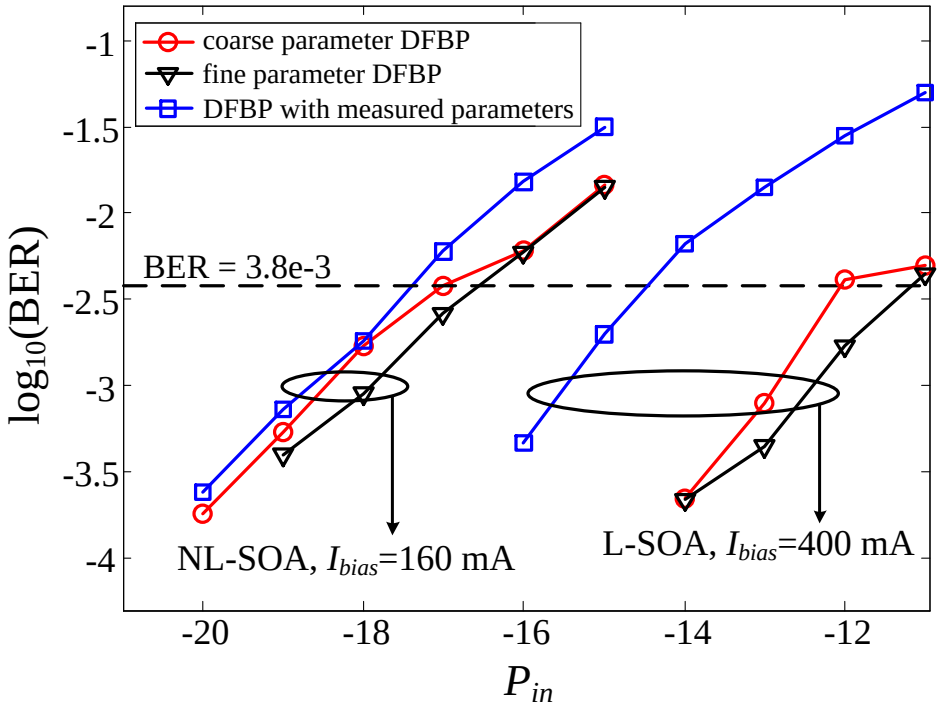

Figure 3.4: BER versus SOA input power for fine parameter DFBP, coarse parameter DFBP and DFBP using the parameters obtained from characterization of NL-SOA and L-SOA.

that above and below the FEC limit. Despite having covered a wide range with limited resolution, our approach fell safely in the below-FEC level. Even with no prior information on the SOA used (either SOA characterization or even linear/nonlinear category), we can blindly find a DFBP solution that moves us below the FEC level. Fig. 3.5 suggests that DFBP performance is more sensitive to P_{sat} than τ_c. The width of the low-BER region for P_{sat} is around 1 dBm for both plots which validates our choice for resolution of P_{sat} in coarse estimation.

3.4.3 Propagation performance—two SOA types

In this section we examine the efficiency of DFBP in the presence of fiber propagation for two types of SOA. Fig. 3.6 shows BER versus received OSNR measured in 0.1 nm resolution bandwidth; the BER curve with square markers corresponds to B2B without SOA (and hence no nonlinearity or DFBP), i.e., no SOA and no fiber. Two types of SOA, linear and nonlinear, are examined using a DFBP with parameters found per the method described in section 3.2. The SOA currents were fixed at the values determined in section 3.4.1. The SOA input power was set to $P_{in} = -21$ dBm and -17 dBm (or equivalently, $P_{launched} = 1$ dBm) for NL-SOA and L-SOA, respectively. We launched the 16-QAM signal into 80 km and 60 km of SMF for each SOA. The OSNR penalty is less than 4 dB for all cases when we apply the DFBP algorithm.

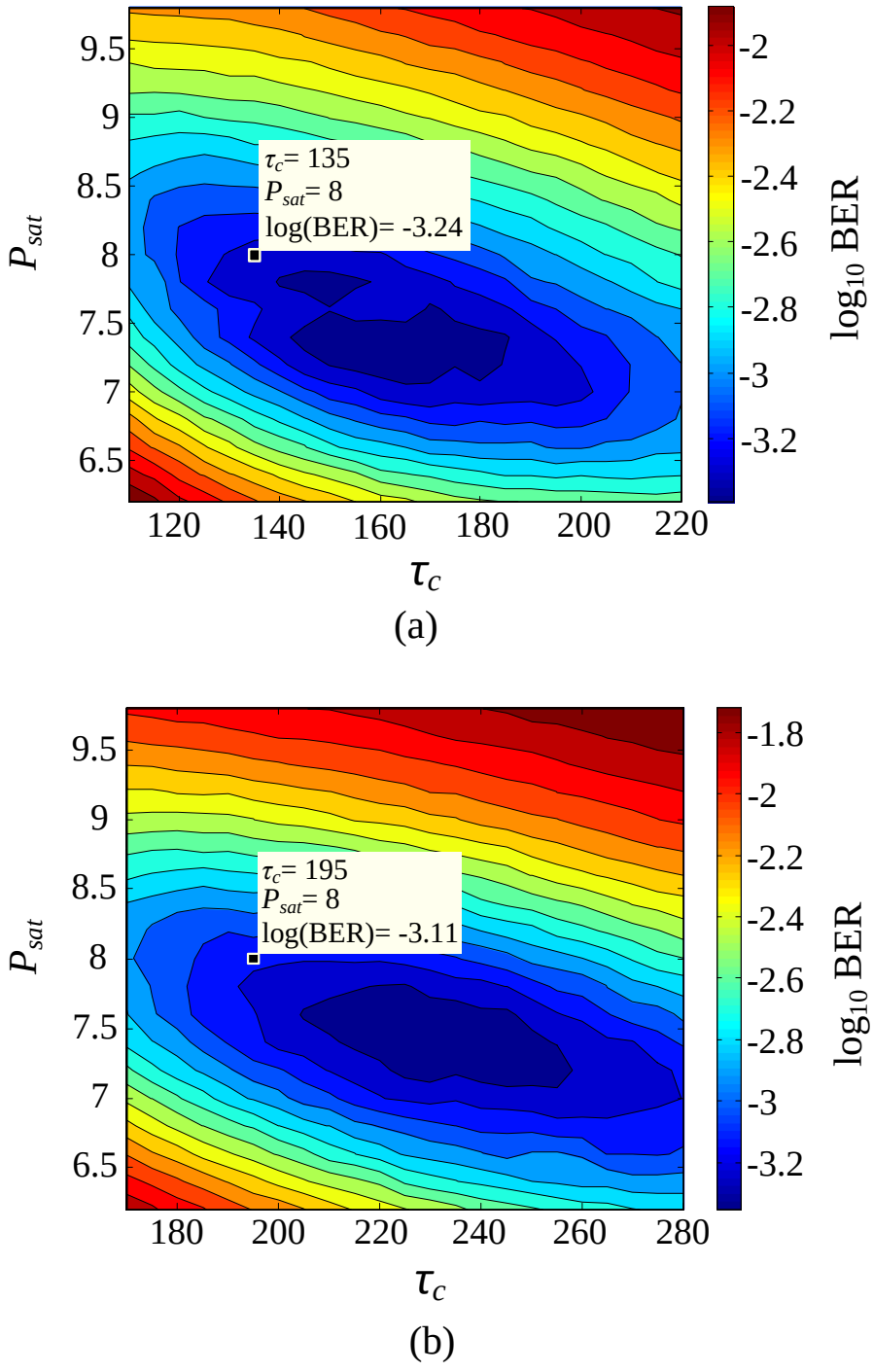

Figure 3.5: BER as a function of τ_c and P_{sat}. The specified point is the parameter pair found by EVM optimized, coarse estimation method for DFBP. The estimated parameter set is close to the middle dark blue region with minimum BER. (a) NL-SOA; (b) L-SOA.

While not shown in Fig. 3.6, we also observed that with 100 km of fiber, the BER is above the FEC limit within the achievable OSNR range.

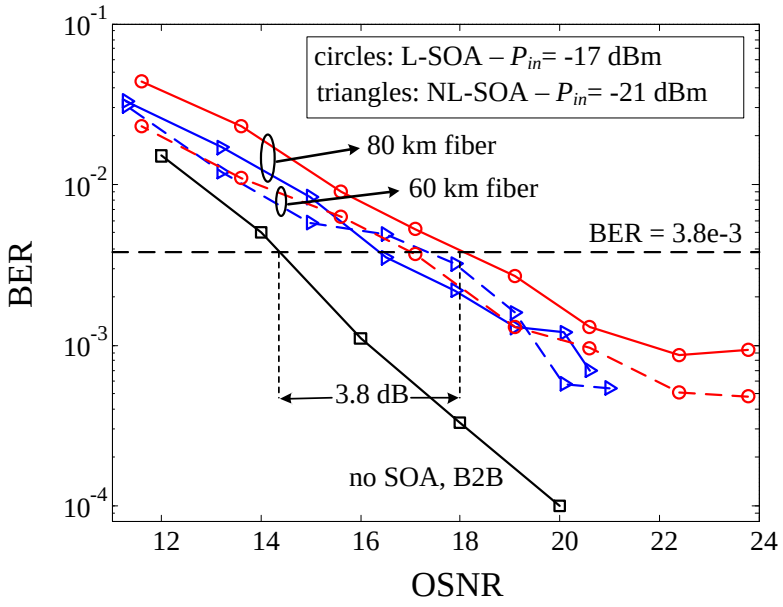

Figure 3.6: BER versus OSNR in 0.1 nm resolution bandwidth with coarse parameter DFBP. OSNR penalty at FEC threshold is 3.8 dB for 80 km transmission compared to a B2B system with no SOA and fiber.

3.5 Conclusion

We presented a simple method based on EVM to coarsely estimate parameters of DFBP. The proposed scheme determines DFBP parameters by processing a small portion of data (4000 symbols). We demonstrated, via experiment and simulations, the efficiency of a DFBP using an EVM optimized, coarse parameter estimation for mitigating SOA-induced phase and amplitude distortions in 16-QAM with coherent detection at 22 Gbaud. The penalty due to coarse estimation of DFBP parameters is negligible compared to DFBP with very fine parameter estimation. We examined the OSNR penalty induced by application of SOA as booster at transmitter in transmission of signal over 80 km of SMF. The experimental results show less than 4 dB OSNR penalty at FEC threshold (BER $= 3.8 \times 10^{-3}$) for both nonlinear and linear SOAs employed in our experiment.

The coarse parameter DFBP technique we proposed and demonstrated for SOA nonlinearity compensation offers a simple solution for improving performance of integrated transceivers in optical networks with coherent detection. While previous methods based on SOA dynamic gain equation add substantial complexity to the system, our technique not only simplifies the compensation, but also gives superior performance compared to the previous techniques. The

requirement for large power backoff can be eliminated in next-generation optical networks by using the proposed compensation method.

Part II

Optical OFDM Performance Improvement

Chapter 4

Modeling and Compensation of CO-OFDM Transmitter Nonlinearity

Abstract

In this chapter, published in [4], we present a comprehensive study of nonlinearities from an optical OFDM transmitter and propose a combination of clipping and predistortion to compensate for the nonlinear distortions. Nonlinearities are introduced by the combination of effects from the DAC, electrical PA and optical modulator in the presence of PAPR. We introduce parameters to quantify the transmitter nonlinearity. High input backoff avoids OFDM signal compression from the PA, but incurs high penalties in power efficiency. At low input backoff, common PAPR reduction techniques are not effective in suppressing the PA nonlinear distortion. A bit error distribution investigation shows a technique combining nonlinear predistortion with PAPR mitigation could achieve good power efficiency by allowing low input backoff. We use training symbols to extract the transmitter nonlinear function. We show that PLI leads to an accurate transmitter nonlinearity characterization. We derive a semi-analytical solution for BER that validates the PLI approximation accurately captures transmitter nonlinearity. The inverse of the PLI estimate of the nonlinear function is used as a predistorter to suppress transmitter nonlinearity. We investigate performance of the proposed scheme by Monte Carlo simulations. Our simulations show that when DAC resolution is more than 4 bits, BER below FEC limit of 3.8×10^{-3} can be achieved by using predistortion with very low input power backoff for electrical PA and optical modulator.

4.1 Introduction

OFDM is a flexible modulation technique that has had wide adoption in wireline (telephone and cable) and wireless communications standards [38–40]. As optical communications move into a new era where spectral efficiency is of increased importance, OFDM is undergoing extensive examination as a key enabler. Robustness to channel dispersion and its flexible

structure make optical OFDM attractive for both long-haul and short-reach applications [10, 41–47].

In OFDM systems, an inverse fast Fourier transform (IFFT) is used to modulate the data onto orthogonal subcarriers for transmission. Some data sequences lead to a large number of subcarriers adding together with coherent phase, and this leads to high peaks in the OFDM signal. This is known as high PAPR and is a major challenge in OFDM systems. PAPR is especially problematic at the transmitter where OFDM signals are more susceptible to nonlinear distortions arising in the DAC, the electrical PA and the optical modulator [48, 49].

Various schemes have been proposed and demonstrated to resolve the PAPR problem in OFDM systems including clipping, nonlinear companding, selective mapping (SLM), trellis shaping, predistortion and many other techniques with different efficiency and computational complexity [50, 51]. Recently, some of these approaches originally developed for wireless and wireline have been applied in optical OFDM systems. In [52], a Zadoff–Chu sequence is utilized to build a precoding matrix applied before the IFFT at the transmitter to reduce PAPR. Trellis shaping is used to reduce PAPR in [53]. With the SLM technique, 1 dB Q factor improvement is obtained in a QPSK CO-OFDM system when optical fiber is the only nonlinearity source [54].

Predistortion is deployed extensively to compensate for transmitter nonlinearities. In radio frequency (RF) OFDM, the main focus is usually on electrical PA nonlinearity [55–58]. In optical OFDM, on the other hand, predistortion is applied to mitigate nonlinearity of electrical-to-optical conversion block [59–63]. In [59–61], predistortion is based on inverting the sinusoidal transfer function of the MZM. An adaptive digital predistorter is utilized in [63] to compensate for optical modulator nonlinearity. Polynomials are used to estimate the nonlinear transfer function of optical modulator. A frequency-domain predistorter is used to compensate for nonlinearity of direct-detection optical OFDM systems in [62].

While the previous PAPR studies have focused on one or two sources of nonlinearity, we address the distortions as they appear along the transmitter RF front-end, from DAC to amplifier to modulator [3]. In this chapter, we use combination of clipping and predistortion to overcome transmitter nonlinearity aggravated by high PAPR. We propose a simple strategy to characterize the nonlinear transfer function of the CO-OFDM transmitter; the nonlinearity estimate is used to calculate the correct predistortion to apply. We show that transmitter nonlinear response approximated by PLI leads to effective predistortion. We derive a semi-analytical solution for BER that validates (via Monte Carlo techniques) the PLI approximation accurately captures transmitter nonlinearity. Note that although we use predistortion to suppress *transmitter* nonlinearities, in the characterization step, the estimated transfer function captures nonlinear effects of the whole B2B system. Therefore, once system nonlinear response is accurately estimated, predistortion mitigates distortions regardless of the source of nonlinear-

ity. Although fiber nonlinearity is exacerbated by high PAPR, compensation of fiber nonlinear effect requires complex methods and can be implemented independent of transmitter compensation [64]. In this thesis, our focus is on optical networks with short/medium reach and we neglect fiber nonlinearity.

In section 4.2, we give a brief review of PAPR in OFDM. We describe the models used in our study and introduce parameters varied in simulations in section 4.3. The impact of transmitter nonlinearity on performance of optical OFDM is investigated in section 4.4. In section 4.5, we analyze the distribution of OFDM symbol errors with respect to PAPR. Based on this information, we establish our strategy to tackle transmitter nonlinear distortion in the presence of high PAPR. We provide a semi-analytical solution to estimate CO-OFDM system performance in the presence of nonlinearity. We also explain our proposed transmitter characterization method based on training sequences and the PLI approximation. In section 4.6, we examine the performance of the proposed method via Monte Carlo simulations considering different transmitter nonlinear characteristics and compare the results with theoretical predictions. Finally, we draw conclusions in section 4.7.

4.2 PAPR in OFDM

The baseband OFDM signal after IFFT at the transmitter is given by

$$x(t) = \frac{1}{\sqrt{N}} \sum_{k=0}^{N-1} X_k \exp(j2\pi f_k t), \quad 0 \le t < T_s, \tag{4.1}$$

where N is the FFT size, X_k are the complex data modulating subcarriers, $f_k = k/T_s$ is the center frequency for k^{th} subcarrier and T_s is the period of the OFDM symbol.

Assuming that the input data are statistically independent and identically distributed (i.i.d.), the real and imaginary part of $x(t)$ are orthogonal and uncorrelated. The real part $\Re\{x(t)\}$ and imaginary part $\Im\{x(t)\}$ each has a Gaussian distribution with zero mean and variance of $\frac{1}{2}\mathrm{E}\left[|X_k|^2\right]$ for large N ($N > 64$) based on the central limit theorem. Accordingly, the instantaneous signal power has a central chi-squared distribution with two degrees of freedom; its probability density function (PDF) is strictly decreasing with a maximum at zero. We will exploit this fact to justify our suggested mitigation approach in section 4.5.

PAPR of an OFDM symbol is defined as the ratio between maximum instantaneous power and average power, given by

$$\mathrm{PAPR} = \frac{\max\limits_{0 \le t < T_s} \left[|x(t)|^2\right]}{\frac{1}{T_s}\int_0^{T_s} |x(t)|^2 \, \mathrm{d}t}. \tag{4.2}$$

Assuming that OFDM symbols have constant average power, PAPR is essentially determined by the instantaneous power which varies with the data sequence transmitted. For example, if

subcarriers add together coherently, large peaks will be observed in the OFDM signal envelope leading to high PAPR. Furthermore, PAPR increases with increasing N. The number of symbols in the constellation used to transmit multiple bits per subcarrier has negligible effect on PAPR statistics [65]. Throughout this chapter, we use FFT size of 256 and investigate 16-QAM signaling in simulations.

4.3 System Model

In this section, we explain the system model employed in simulations and analysis. We particularly focus on nonlinearity sources at the transmitter and introduce three different parameters capturing the distortion contribution of each component. We vary these parameters to quantify the performance degradation in section 4.4.

Fig. 4.1 shows the block diagram for an M-QAM CO-OFDM system. PRBSs with length of $2^{21}-1$ are used to generate 16-QAM symbols. IFFT and cyclic prefix addition are two key blocks in OFDM systems. An IFFT is used to modulate data onto orthogonal subcarriers. A cyclic prefix is appended to the time domain OFDM signal to facilitate channel equalization at the receiver. In simulations, the IFFT size is 256 of which 196 data-bearing subcarriers are available in each OFDM symbol. The remaining 60 subcarriers are left empty to achieve an oversampling factor of $R_{\text{os}} = 1.3$. Oversampling reduces the impact of aliasing at the DAC [43]. Eight samples are added to each OFDM symbol as a cyclic prefix, leading to 9.43 ns symbol duration with 28 GS/s sampling rate and a bit rate of 83.1 Gb/s.

The OFDM signal is clipped at the transmitter to avoid large peaks and decrease quantization noise induced by the DAC. Normalized clipping level, the so-called clipping ratio (CR) defined as the ratio between clipping level and rms power of the OFDM signal, is used to quantify clipping [66]. A predistortion block is also included in the OFDM transmitter shown in Fig. 4.1 which will be explained in section 4.5. After digital-to-analog conversion, the I/Q signals are amplified with an RF amplifier and drive an I/Q optical modulator biased at the null point and modulating an ideal continuous-wave (CW) laser. ASE noise is added to the signal in the channel before detection. The signal is coherently detected by an LO. After analog-to-digital-conversion, the signals are processed at the OFDM receiver to recover the data bits and calculate BER. At least 200 errors are detected for each point to accurately estimate BER. The DSP performed in the OFDM receiver is described in Appendix B. The DAC, electrical PA and optical modulator each play an important role in the nonlinear behaviour of the transmitter and they are explained in more detail.

4.3.1 DAC

When OFDM signals are converted from digital to analog domain, they experience quantization noise due to finite DAC resolution. In a DAC with k bits resolution, the closest of 2^k levels

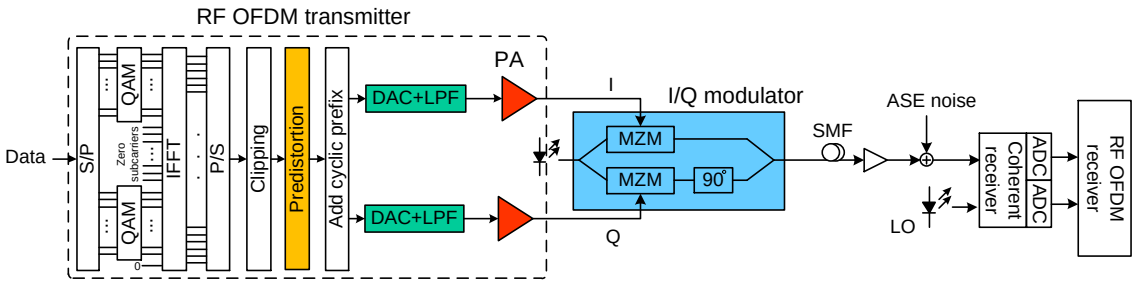

Figure 4.1: M-QAM CO-OFDM system block diagram. ADC: analog-to-digital converter, S/P: serial-to-parallel, P/S: parallel-to-serial.

is assigned to each input sample. As the maximum and minimum levels of the DAC are determined by the input signal amplitude range, OFDM signals with high PAPR have wider excursions which must span the same DAC levels, and thus suffer from excessive quantization noise. In our simulations, we find the maximum (minimum) amplitude of an OFDM frame consisting of 1000 OFDM symbols and assign it to the highest (lowest) level of quantization. The remaining $2^k - 2$ levels are uniformly distributed between the minimum and maximum levels. After quantization we upsample the signal by a factor of 4 and apply a fourth-order super-Gaussian low-pass filter (LPF). This model has enough accuracy to simulate most DAC effects [66]. We find it sufficient in our study, without need of a more comprehensive model based on effective number of bits (ENOB) that includes integral nonlinearity (INL) and differential nonlinearity (DNL) of the DAC [67].

4.3.2 Electrical PA

Modeling the nonlinear response of PAs can take many forms. In this work, we use a simple solid-state PA (SSPA) model in which the amplifier is viewed as a memoryless nonlinearity [65]. In the SSPA model, AM/PM conversion is assumed to be negligible and AM/AM conversion is given by

$$g_{SSPA}\left(A\left(t\right)\right) = \frac{g_0 A\left(t\right)}{\left[1 + \left(\frac{A(t)}{A_{sat}}\right)^{2p}\right]^{\frac{1}{2p}}}, \tag{4.3}$$

where $A\left(t\right)$ is the input signal amplitude, g_0 is the amplifier gain, A_{sat} is the input saturation amplitude and p adjusts AM/AM saturation sharpness. We take $p = 2$ as a good approximation of available commercial amplifiers [40]. For $p = 2$, the input signal experiences 1.5 dB gain compression when it is at the saturation level. The gain $g_{SSPA}\left(A\left(t\right)\right)$ can also be cast from (4.3) as

$$g_{SSPA}\left(A\left(t\right)\right) = \frac{g_0 \sqrt{P_{sat}}}{\left[1 + \left(\frac{P_{sat}}{P_{in}(t)}\right)^{p}\right]^{\frac{1}{2p}}}, \tag{4.4}$$

where $P_{in}(t)$ is input power and $P_{sat} = A_{sat}^2$. In order to quantify nonlinear distortion induced by PA, we define input backoff (IBO) as the ratio between input saturation and average power, i.e., IBO $= P_{sat}/P_{avg}$. While higher IBO gives a more linear response, it leads to an inefficient PA. High bandwidth communications systems require significant trade-off of efficiency and distortion, as wideband linear amplifiers significantly increase system cost.

4.3.3 Optical modulator

Depending on the structure of subcarriers and the OFDM transmitter, an I/Q modulator or a single external modulator can be deployed for electrical-to-optical conversion in CO-OFDM. Simulations presented in this chapter assume an I/Q modulator with symmetric nonlinear response for I and Q branches, i.e., no I/Q imbalance. We expect similar behaviour in terms of transmitter nonlinearity for CO-OFDM systems using either I/Q or a single modulator.

In this study, an MZM is assumed in both simulations and analysis. The transfer function of an MZM is illustrated in Fig. 4.2. In CO-OFDM systems, the modulator is biased at the null point and the driving signal amplitude is kept between $\pm V_\pi$ where V_π is half-wave voltage of MZM. We adjust maximum (minimum) of the RF OFDM signal to V_π $(-V_\pi)$ to ensure clipping is excluded from the modulator induced nonlinearities. To sweep the MZM nonlinear effect, we multiply the driving signal amplitude, $V_d(t)$, by α_d $(\alpha_d \leq 1)$ considering some backoff in the MZM operating range. In this case, the output optical field of the MZM, $E_{out}(t)$, can be expressed as

$$E_{out}(t) = E_{in}(t) \sin\left(\frac{\pi \alpha_d V_d(t)}{2V_\pi}\right), \tag{4.5}$$

where $E_{in}(t)$ is the input optical field to be modulated. Smaller α_d leads to better nonlinear performance, but comes with the cost of optical power inefficiency. In other words, as α_d decreases, the impact of optical modulator nonlinearity on the signal decreases; however, the output signal will be more attenuated due to higher insertion loss of the optical modulator.

Considering combination of the nonlinearity from amplifier and optical modulator, the overall normalized nonlinear function of the transmitter is given by

$$g_{TX}(A) = \sin\left(\frac{\pi \alpha_d}{2V_\pi} \frac{g_{SSPA}(A)}{g_{SSPA}(A_{max})}\right), \tag{4.6}$$

where A_{max} is the maximum input amplitude. Notice that the transmitter nonlinear function has a symmetry to the origin, i.e., it is an odd function. Therefore, for convenience we assume that $g_{TX}(A)$ acts on magnitude alone.

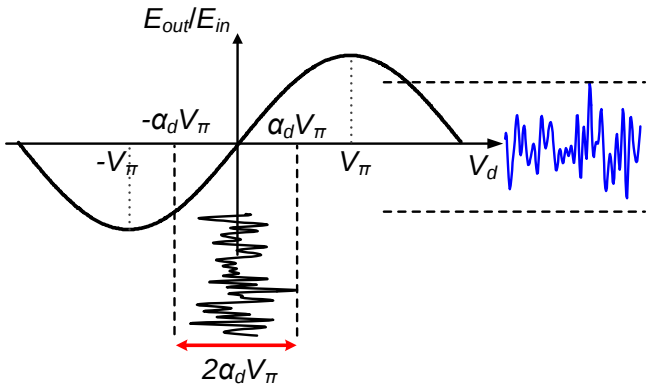

Figure 4.2: Transfer function of MZM biased at null point for CO-OFDM. Nonlinearity is varied by changing the electrical signal range through α_d.

4.4 Impact of Transmitter Nonlinearity on OFDM Performance

To investigate the impact of transmitter nonlinear distortions on performance of optical OFDM, we vary the parameters introduced in section 4.3 for DAC, electrical PA and MZM for a 16-QAM CO-OFDM system. One thousand OFDM symbols (called one OFDM frame in the remainder of this chapter) are transmitted in the simulations presented in this section.

Fig. 4.3(a), Fig. 4.3(b) and Fig. 4.3(c) show EVM versus IBO for a DAC with respectively 4, 5 and 6 bits resolution. Solid blue lines represent the results with clipping and dashed red lines show the results without clipping. Intentionally clipping the signal at the transmitter can suppress quantization noise. CR is swept in Monte Carlo simulations to find the clipping level offering lowest EVM for each DAC resolution. The CRs are adjusted at 1.9, 2.1 and 2.25 for 4-, 5- and 6-bit DAC, respectively. The performance improvement obtained is significant when a lower resolution DAC is employed; however, the improvement gradually disappears as higher resolution DACs are used, compare Fig. 4.3(a) with Fig. 4.3(c). In addition, clipping is not effective in mitigating the nonlinearity from electrical PA and MZM. This can be explained by the difference in nature of DAC quantization noise and the nonlinearity induced by electrical PA and MZM. High peaks in the OFDM signal lead to larger separation of DAC quantization levels, which exacerbates quantization noise for all samples regardless of their amplitude. Therefore, limiting PAPR of the OFDM signal improves overall performance while sacrificing accuracy of high amplitude samples. On the other hand, performance degradation in electrical PA and MZM is due solely to compression of relatively high-amplitude samples; low-amplitude samples remain largely unaffected. As a result, while clipping is effective to reduce DAC quantization noise, other mitigation techniques should be utilized to overcome nonlinearity induced by electrical PA and MZM (the same applies to other DAC nonlinearities such as INL

and DNL).

Fig. 4.3 also indicates that when IBO is higher than a certain value, the amplifier response is very linear and no improvement in EVM can be achieved by increasing IBO. Driving the modulator across the full range considerably deteriorates OFDM performance. For example, when IBO is equal to 4 dB, $\alpha_d = 0.6$ and $\alpha_d = 1$ give respectively 2% and 5.4% EVM degradation with respect to the case where a linear optical modulator is used. This suggests the importance of adjusting MZM driving voltage; by slightly reducing driving OFDM signal amplitude range, performance can be enhanced significantly. We emphasize that use of power backoff for electrical PA and modulator reduces power efficiency. Therefore, although higher backoff leads to linear transmitter response, it decreases the output optical power which makes it more susceptible to noise and can lead to performance degradation. This effect is not considered in Fig. 4.3. The impact of α_d on modulation efficiency of optical modulator will be discussed in section 4.6.

4.5 Transmitter Nonlinearity Characterization

The PAPR of an OFDM signal directly affects its performance in the presence of nonlinear distortions. In [54], Goebel *et al.* showed there is a correlation between OFDM symbol PAPR and Q factor; OFDM symbols with higher PAPR have lower Q factor. As discussed in section 4.2, the PDF of instantaneous signal power is strictly decreasing. Thus, OFDM symbols with high PAPR are less likely to occur. To motivate our proposed predistortion strategy we will examine the distribution of the bit errors as a function of PAPR. This distribution will be indexed by the IBO to assess the impact of the PA.

4.5.1 Bit error distribution

Fig. 4.4(a) displays error distribution versus PAPR after clipping for one OFDM frame with different clipping levels when DAC resolution is 4 bits, IBO is equal to 6 dB and the MZM is driven across the full range, i.e., $\alpha_d = 1$. Random binary data are used to generate 16-QAM symbols. Errors are densely aggregated in PAPR range between 6 dB and 10 dB when no clipping is applied. PAPR higher than 10 dB leads to poor performance, but PAPR this high appears so rarely that this PAPR range causes few errors.

Clipping decreases PAPR and moves the error distribution toward lower PAPR ranges. By reducing CR, the number of errors decreases while the distribution moves further to left. Note that clipping the signal decreases quantization noise for all samples. Therefore, the reduction in number of errors occurs for all PAPR ranges. As clipping itself induces distortion, despite lower PAPR of the OFDM signal, total number of errors increases by further decreasing CR from the optimum value of 1.9. We verified that the distribution of the number of OFDM symbols versus PAPR is similar to the error distribution, suggesting that the performance of

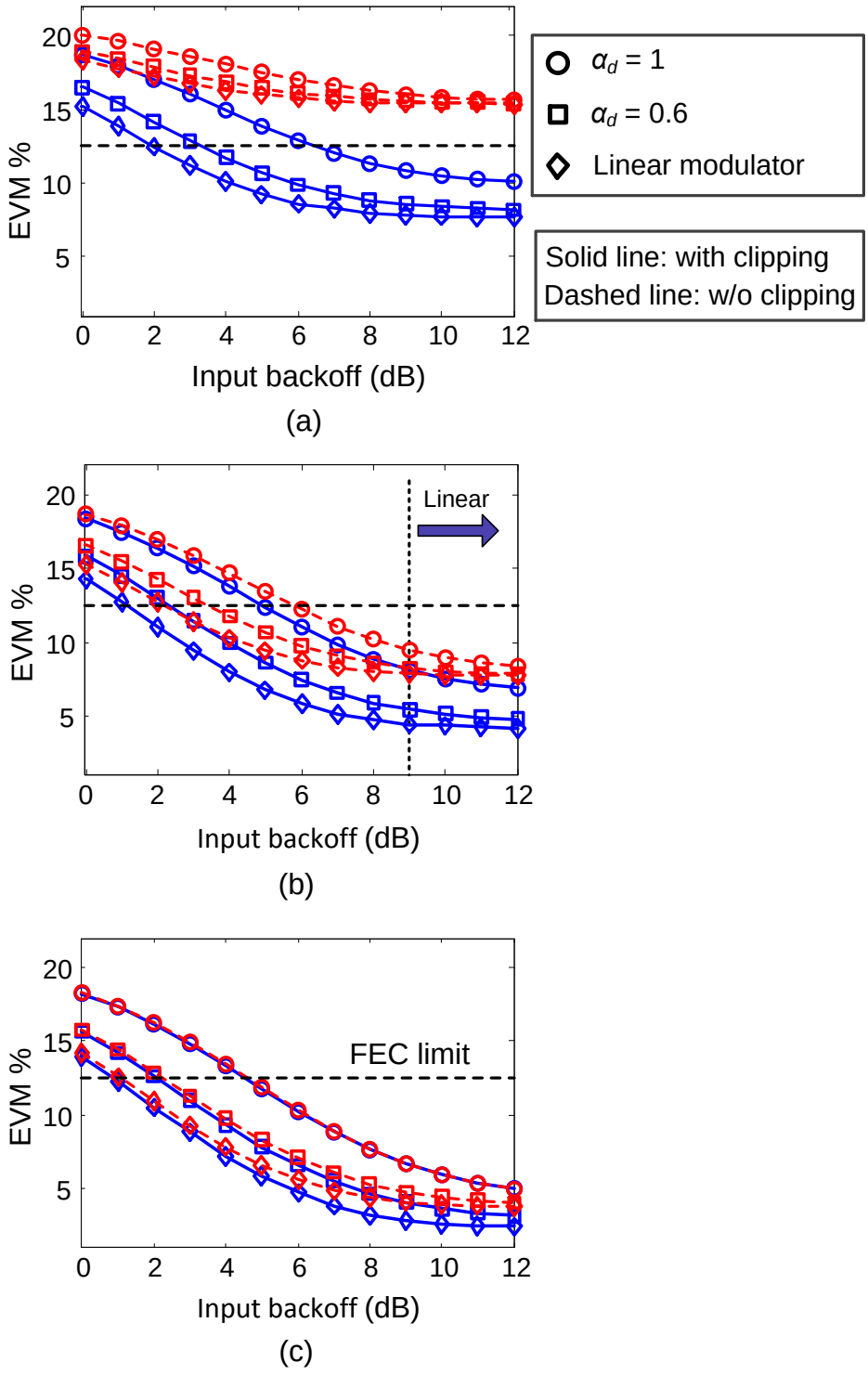

Figure 4.3: EVM versus electrical PA IBO for 16-QAM CO-OFDM system with (a) 4-bit DAC with $CR = 1.9$, (b) 5-bit DAC with $CR = 2.1$ and (c) 6-bit DAC with $CR = 2.25$. BER of 3.8×10^{-3} is considered as FEC limit.

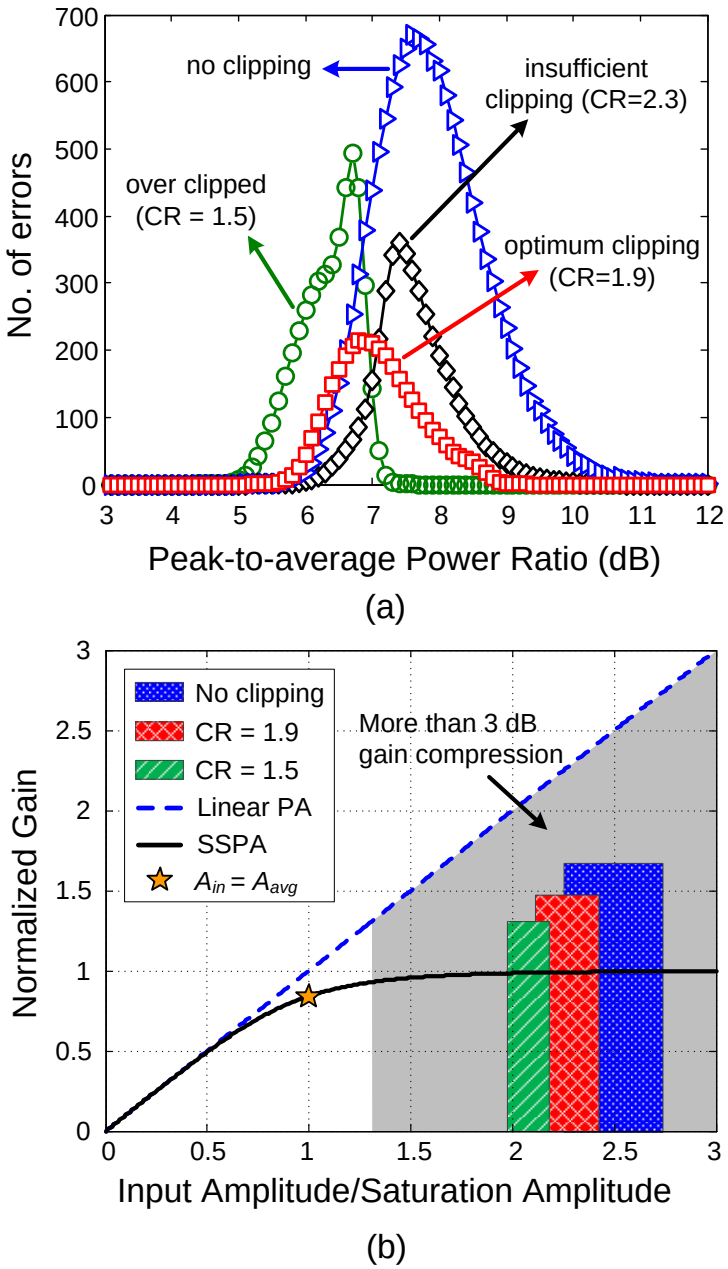

Figure 4.4: (a) Bit error distribution for IBO = 6 dB, $\alpha_d = 1$ and 4-bit DAC as a function of PAPR for one OFDM frame (1000 OFDM symbols) with different clipping levels. (b) Normalized gain versus normalized input amplitude of the electrical PA. Rectangles show the range within one standard deviation of the mean of PAPR for different clipping levels. Star represents the PA input voltage amplitude equal to the average amplitude when IBO = 0 dB.

the OFDM system is mainly determined by PAPRs with greater probability, i.e., those in the modal region.

Fig. 4.4(b) shows normalized gain versus the input amplitude normalized by the saturation amplitude of the PA. The operating point of the amplifier is determined by the IBO; with high IBO, the average of input amplitudes is in the linear region. A star indicates average amplitude level when IBO is equal to 0 dB in Fig. 4.4(b). The gray shading denotes the region where gain compression is more than 3 dB. The rectangles represent the modal region of the PAPR probability density—the range within one standard deviation of the mean value—for different CRs. This range depends on both PAPR and IBO as

$$\frac{A_{max}}{A_{sat}} = \sqrt{\frac{\text{PAPR}}{\text{IBO}}}. \tag{4.7}$$

In order to avoid gain compression more than 3 dB at the electrical PA, the ratio between maximum input amplitude and saturation amplitude should be less than 1.3. Equivalently, the difference between PAPR and IBO should be less than 2.3 dB. With IBO as low as 0 dB, it is not possible to avoid distortion at the PA by utilizing common PAPR reduction methods. For example, by using the SLM technique with reasonable complexity and overhead, the PAPR would still be more than 6 dB (see Fig. 1 in [50]). Therefore, after initial PAPR reduction, other methods must be employed to mitigate the distortions from the electrical PA and MZM.

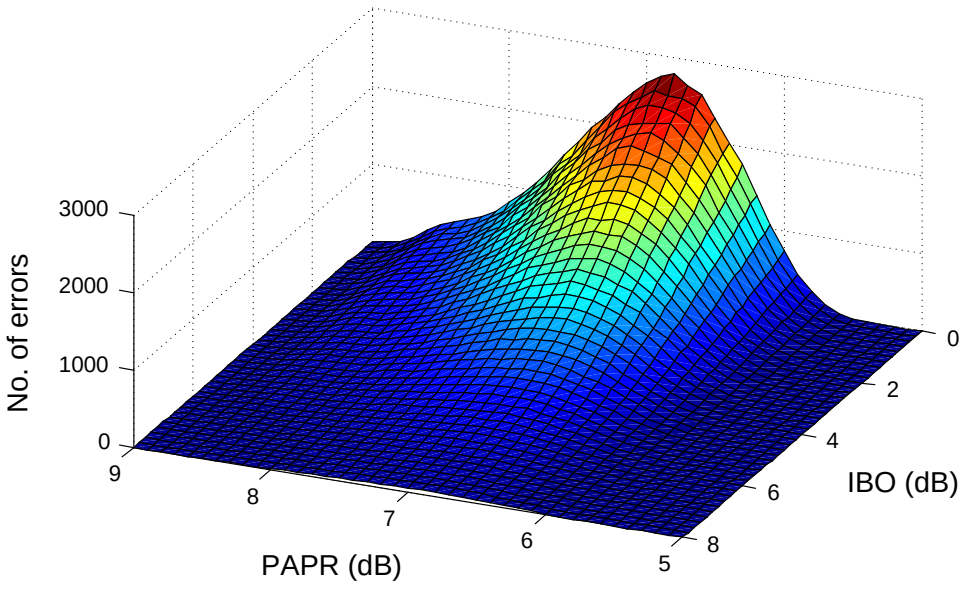

Figure 4.5: Error distribution of one OFDM frame (1000 OFDM symbols) versus PAPR for different electrical PA IBOs when $\alpha_d = 1$ and 4-bit DAC is used. The number of errors is averaged over 200 OFDM frames.

Fig. 4.5 depicts the distribution of errors as a function of PAPR for various IBOs and CR

equal to 1.9. We observed less than 0.1 dB variation in the mean of PAPR. The distributions shown in Fig. 4.4 are relatively similar for different amplifier IBOs. Simulations also showed that with a higher DAC bit resolution less improvement is observed by clipping; however, the OFDM signal experiences roughly the same nonlinear distortion at the electrical PA and MZM as the 4-bit DAC case.

Various techniques have been introduced in the literature to decrease PAPR of the OFDM signal. However, these methods are not very effective when significant nonlinear distortion is imposed by the electrical PA and modulator in the OFDM transmitter. The block diagram in Fig. 4.6 shows the advantage of employing predistortion to mitigation strategies. After decreasing PAPR with common PAPR reduction techniques, high power backoff should be considered for the input OFDM signal to the optical modulator and electrical PA to avoid severe nonlinear distortion. Predistortion improves power efficiency of the OFDM transmitter significantly by alleviating the requirement for high power backoff. Our examination of error distributions as a function of IBO leads us to propose the second strategy with predistortion.

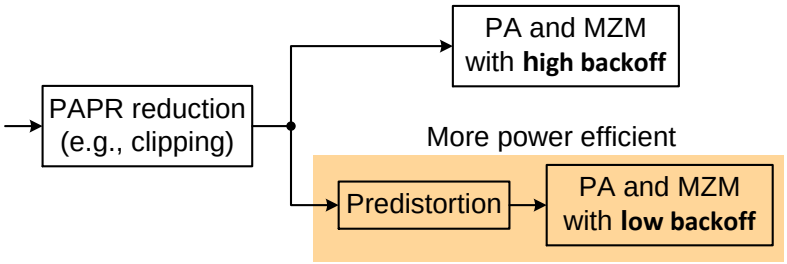

Figure 4.6: Comparison of power backoff requirement for the transmitter with and without predistortion.

In order to implement the predistorter, the nonlinear response of the transmitter should be characterized. In the next section, we describe a simple technique for characterizing the nonlinear response of the transmitter. We provide theoretical analysis that enables us to evaluate performance of the system in presence of nonlinearity and accuracy of the nonlinear function estimation.

4.5.2 Evaluation of BER

Development of a theoretical equation to assess system performance in the presence of nonlinearity not only allows us to see the impact of nonlinear distortions on the system, but also gives us a tool to investigate the accuracy of the estimated predistortion function. Fig. 4.7 summarizes the models used for the theoretical analysis. The DAC quantization noise and clipping is modeled as additive Gaussian noise [66]. With the assumption of a Gaussian distribution for real and imaginary parts of the OFDM signal, and by exploiting Bussgangs theorem, it

has been shown previously that the memoryless nonlinearities in OFDM can be modeled by a constant factor and an additive noise term with zero mean [68,69]. We use the same approach in modeling the electrical PA and MZM nonlinearity. Finally, AWGN is added to the signal as ASE noise.

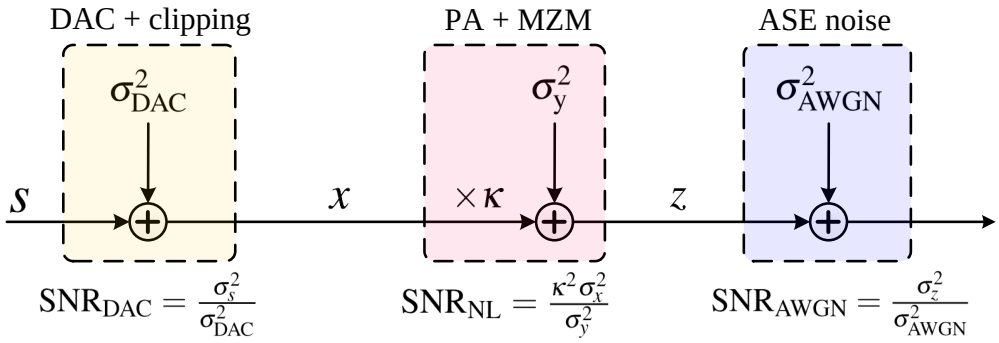

Figure 4.7: Block diagram of the models used for theoretical analysis. Each noise source has impact on total SNR and degrades signal quality.

Let $z(t)$, $x(t)$ and $g(\cdot)$ be the output signal, input signal and nonlinear function of the OFDM transmitter where $z = g(x)$. The output of the nonlinear block can be written as [57,68–70]

$$z\left(t\right) = \kappa x\left(t\right) + y\left(t\right), \tag{4.8}$$

where κ is a constant factor and $y(t)$ is an additive zero-mean noise component uncorrelated with the input signal, i.e., $\mathrm{E}\left[x(t)y(t)\right] = 0$. The attenuation factor κ and variance of $y(t)$, σ_y^2, can be written as

$$\kappa = \frac{\mathrm{E}\left[x(t)z(t)\right]}{\sigma_x^2} = \frac{1}{\sigma_x^2}\int_{-\infty}^{\infty} x g\left(x\right) \frac{1}{\sqrt{2\pi\sigma_x^2}} \exp\left(-\frac{x^2}{2\sigma_x^2}\right) \mathrm{d}x, \tag{4.9}$$

$$\sigma_y^2 = \mathrm{E}\left[z(t)^2\right] - \kappa^2\sigma_x^2 = \int_{-\infty}^{\infty} g^2\left(x\right) \frac{1}{\sqrt{2\pi\sigma_x^2}} \exp\left(-\frac{x^2}{2\sigma_x^2}\right) \mathrm{d}x - \kappa^2\sigma_x^2, \tag{4.10}$$

where σ_x^2 is the input signal variance. Although $y(t)$ is not a Gaussian process, after the FFT block at the receiver, the noise component can be approximated as AWGN with variance of σ_y^2 for large N due to central limit theorem arguments [69].

In [66], Berger *et al.* studied the distortions induced by clipping and quantization effect of DAC and showed that the Gaussian approximation leads to accurate BER estimation for BER above 10^{-4}. The DAC noise variance can be obtained by [66]

$$\sigma^2_{\mathrm{DAC}} = \sigma_x^2 \sum_{j=0}^{N_Q/2-1} \Bigg(\left[(2j+1)^2 \delta^2 + 2 \right] \left[\Phi\left(\sqrt{2}\,(j+1)\,\delta \right) - \Phi\left(\sqrt{2} j \delta \right) \right] + \frac{2\delta}{\sqrt{\pi}} \left[j e^{-(j+1)^2\delta^2} - (j+1)\, e^{-j^2\delta^2} \right] \Bigg) + \sigma_x^2 \left(\left[(N_Q - 1)^2 \delta^2 + 2 \right] \left[1 - \Phi\left(\frac{N_Q \delta}{\sqrt{2}} \right) \right] - \frac{N_Q - 2}{\sqrt{\pi}} \delta e^{-\frac{N_Q^2}{4}\delta^2} \right), \tag{4.11}$$

where N_Q is the number of quantization levels, δ is the distance between two adjacent quantization levels and $\Phi(t)$ is the Gaussian cumulative density function given by

$$\Phi\left(t\right) = \frac{1}{\sqrt{2\pi}} \int_{-\infty}^{t} e^{-\frac{x^2}{2}}\, \mathrm{d}x. \tag{4.12}$$

Hence, the SNR at the receiver is given by

$$\mathrm{SNR} = R_{\mathrm{os}} \frac{\kappa^2 \sigma_x^2}{\kappa^2 \sigma^2_{\mathrm{DAC}} + \sigma_y^2 + \sigma^2_{\mathrm{AWGN}}}, \tag{4.13}$$

where σ^2_{AWGN} denotes variance of optical channel noise due to ASE and R_{os} is the oversampling factor.

The SNR at the receiver can also be written as a function of SNR after each noise source. The SNR at the output of each block is given in Fig. 4.7. Each noise source has an influence on the SNR and degrades signal quality. Using the SNR definition at the output of each noise source, the SNR at the receiver can be written as

$$\mathrm{SNR} \approx R_{\mathrm{os}} \frac{\mathrm{SNR_{DAC}SNR_{NL}SNR_{AWGN}}}{\mathrm{SNR_{DAC}} + \mathrm{SNR_{DAC}SNR_{NL}} + \mathrm{SNR_{DAC}SNR_{AWGN}} + \mathrm{SNR_{NL}SNR_{AWGN}}}. \tag{4.14}$$

The approximation is made by assuming the total signal power remains the same after clipping and DAC quantization, i.e., $\sigma_{\mathrm{s}}^2 \approx \sigma_{\mathrm{x}}^2$. Consequently, the bit error probability for M-QAM with Gray coding is given by

$$\mathrm{BER} = \frac{2}{\log_2 \mathrm{M}} \frac{\sqrt{\mathrm{M}} - 1}{\sqrt{\mathrm{M}}} \mathrm{erfc}\left(\sqrt{\frac{3}{2\left(\mathrm{M}-1\right)} \mathrm{SNR}} \right). \tag{4.15}$$

In order to calculate κ and σ_y^2 for the optical OFDM transmitter model, the integrals should be evaluated for the nonlinear function given by (4.6). Derivation of a closed-form equation for κ and σ_y^2 is usually a tedious task and not always possible. Therefore, we approximate the nonlinear function by PLI to obtain a simplified solution.

4.5.3 PLI for transmitter nonlinearity characterization and predistortion

Although different models are available to study nonlinear effects in optical OFDM transmitters, it is challenging to find the nonlinear response of a real system. The nonlinear function of the transmitter can be approximated with desired accuracy in small intervals by using polynomials [70]. This simplifies calculation of the integrals in (4.9) and (4.10). In this section, we take the same approach and approximate the nonlinear response of the transmitter by PLI (first-order polynomial) and show that linear interpolation is sufficient for accurate BER estimation. We also describe a training symbol-based method to extract the PLI approximation of the transmitter nonlinear function.

Let $\hat{g}(x)$ be PLI of $g(x)$ with $m+1$ intervals given by

$$\hat{g}(x) = \begin{cases} a_i x + b_i, & x_i \leq x < x_{i+1} \\ g(x_{m+1}), & x_{m+1} \leq x, \end{cases} \tag{4.16}$$

$i = 1, ..., m$, where a_i is slope of the line in the i^{th} interval from x_i to x_{i+1}, $b_i = g(x_i) - a_i x_i$, $x_1 = 0$ and x_{m+1} is the maximum amplitude of the signal at the output of the clipping block. By using $\hat{g}(x)$ in (4.9) and (4.10), it is straightforward to obtain κ and σ_y^2 as

$$\kappa = \frac{2}{\sigma_x^2} \sum_{i=1}^{m} \left[a_i \psi_2 \left(x_i, x_{i+1} \right) + b_i \psi_1 \left(x_i, x_{i+1} \right) \right] + \frac{2}{\sigma_x^2} g \left(x_{m+1} \right) \psi_1 \left(x_{m+1}, \infty \right), \tag{4.17}$$

$$\begin{aligned} \sigma_y^2 =& 2 \sum_{i=1}^{m} \left[a_i^2 \psi_2 \left(x_i, x_{i+1} \right) + 2 a_i b_i \psi_1 \left(x_i, x_{i+1} \right) + b_i^2 \psi_0 \left(x_i, x_{i+1} \right) \right] \\ & + 2 g^2 \left(x_{m+1} \right) \psi_0 \left(x_{m+1}, \infty \right) - \kappa^2 \sigma_x^2, \end{aligned} \tag{4.18}$$

where $\psi_k(v, w)$ is given in Appendix C. The derived equations for κ and σ_y^2 yields exact values as m goes to infinity. We found that $m = 15$ is accurate enough for estimation of BERs above 10^{-5}.

The nonlinear response of the optical OFDM transmitter can be extracted with high accuracy if its behaviour is approximated by straight lines in sufficiently small input intervals. In order to characterize transmitter nonlinearity, we transmit training sequences and then compare the received instantaneous samples to the transmitted ones. For each amplitude level of the I and Q signals, a unique value can be found as the amplitude compression. If m intervals are considered between 0 and the maximum amplitude of transmitted samples, m points can be obtained by comparing the received and transmitted signals.

Let $x_I[n]$ and $x_Q[n]$ be the real and imaginary part of the OFDM signal after clipping, respectively. Assuming that the nonlinear distortion is the only impairment in the system, the OFDM signal after ADC at the receiver is given by

$$r[n] = g_I(x_I[n]) + jg_Q(x_Q[n]), \tag{4.19}$$

where $g_I(\cdot)$ and $g_Q(\cdot)$ are the AM/AM characteristics of the channel for the I and Q arm, respectively. Let $I_{i,I}$ and $I_{i,Q}$ be

$$I_{i,I} = \left\{ x_I[n] \,|\, \frac{\left(i-\frac{1}{2}\right)A_{I,max}}{m} \le x_I[n] < \frac{\left(i+\frac{1}{2}\right)A_{I,max}}{m} \right\}, \tag{4.20}$$

$$I_{i,Q} = \left\{ x_Q[n] \,|\, \frac{\left(i-\frac{1}{2}\right)A_{Q,max}}{m} \le x_Q[n] < \frac{\left(i+\frac{1}{2}\right)A_{Q,max}}{m} \right\}, \tag{4.21}$$

$i = 1, ..., m$, where $A_{I,max}$ and $A_{Q,max}$ are the maximum amplitude of the I and Q signal, respectively. The definition of these sets assures that all samples map into one of the prescribed intervals. Each sample experiences a certain amount of compression due to the nonlinear response of the transmitter. The compression factor is equal to the ratio between output and input signal amplitude. For each of the defined m intervals in $I_{i,I}$ and $I_{i,Q}$, the average compression factors of the i^{th} interval, $c_I(i)$ and $c_Q(i)$, can be obtained respectively by

$$c_I(i) = \frac{\sum_{x_I[n]\in I_{i,I}} \frac{g_I(x_I[n])}{x_I[n]}}{|I_{i,I}|}, \qquad c_Q(i) = \frac{\sum_{x_Q[n]\in I_{i,Q}} \frac{g_Q\left(x_Q[n]\right)}{x_Q[n]}}{|I_{i,Q}|}, \tag{4.22}$$

where $|\cdot|$ denotes cardinality of the set. Averaging is done over numerous samples in each set to minimize impact of Gaussian noise on the estimated nonlinear response. Linear interpolation of the obtained m coordinates for each of I and Q arms gives the compression functions $f_{LI,I}(x)$ and $f_{LI,Q}(x)$ as

$$f_{LI,I}(x) = \begin{cases} \frac{m[c_I(i)-c_I(i-1)]}{A_{I,max}}\left(x - \frac{iA_{I,max}}{m}\right) + c_I(i), & \frac{(i-1)A_{I,max}}{m} \le x < \frac{iA_{I,max}}{m} \\ c_I(m), & A_{I,max} \le x, \end{cases}, \tag{4.23}$$

$$f_{LI,Q}(x) = \begin{cases} \frac{m\left[c_Q(i)-c_Q(i-1)\right]}{A_{Q,max}}\left(x - \frac{iA_{Q,max}}{m}\right) + c_Q(i), & \frac{(i-1)A_{Q,max}}{m} \le x < \frac{iA_{Q,max}}{m} \\ c_Q(m), & A_{Q,max} \le x, \end{cases}, \tag{4.24}$$

where $c_I(0) = c_Q(0) = 0$. The output of the nonlinear block is equal to the input amplitude multiplied by the compression factor. Therefore, the PLI approximation of the nonlinear response of the transmitter for I and Q signal is respectively given by

$$\hat{g}_I(x) = xf_{LI,I}(x) \quad \text{and} \quad \hat{g}_Q(x) = xf_{LI,Q}(x). \tag{4.25}$$

The estimated transmitter nonlinear functions can be used to evaluate the system performance or pre-compensate for the induced nonlinear distortions in the system. In the latter case, inverse of the estimated functions, i.e., $\hat{g}_I^{-1}(x)$ and $\hat{g}_Q^{-1}(x)$, should be applied before DAC at

the transmitter. While (4.6) assumes both I and Q arms experience the same nonlinearity g_{TX}, for the PLI we estimate the nonlinearity separately in the I and Q arms.

We note that inverse of the nonlinear response can also be applied at the receiver with more flexibility. However, the main problem with post-compensation is increased complexity of the receiver side signal processing as compared to pre-compensation where complexity increase is moderate. The envelope of the OFDM signal varies during transmission due to fiber dispersion. Therefore, the post-compensation block must be applied after frequency-domain equalizer imposing an extra FFT/IFFT operation.

4.6 Simulations

In this section we first validate the accuracy of the BER theoretical expression in (4.15). We next simulate the performance of our PLI-based predistortion when varying IBO and DAC resolution. We also show the impact of optical modulator input signal backoff on its power efficiency.

Monte Carlo simulations are run with the nonlinearity generated per (4.6) for various IBOs, and errors are counted to estimate BER. The theoretical expression for BER is evaluated under two scenarios: 1) with side information of the transmitter nonlinearity, (4.6), and using numerical integration of (4.9) and (4.10), and 2) with the PLI estimate of the nonlinear function, obtained from Monte Carlo simulations, using (4.17) and (4.18). This validation serves two purposes. Firstly they establish that the approximations made in developing the theoretical expression are valid, and secondly that the PLI estimate of the nonlinear function is a good predictor of BER performance. The better the PLI estimate, the better will be the performance of our pre-compensation based on this estimate.

In Fig. 4.8(a) the BER versus electrical PA IBO is plotted where solid lines refer to BER estimate with a Gaussian assumption and side information on nonlinearity, dashed lines with triangle markers refer to BER estimate with a Gaussian assumption and a PLI estimate of nonlinearity, and circle markers refer to BER estimate from Monte Carlo error counting. For PLI, we first transmit 40 OFDM symbols as training signals and estimate the transmitter nonlinear function by linear interpolation with $m = 15$. Afterwards, we extract a_i and b_i and calculate BER using (4.17) and (4.18). For an ideal DAC, the estimated nonlinear function is very accurate; both approaches give the same BER. However, when a 4-bit DAC is used PLI approach underestimates BER. This is expected since with a low-bit DAC, there is not enough resolution to accurately estimate the nonlinear function of the transmitter. We also note the good agreement between Monte Carlo simulations and theoretical BER calculation.

In Fig. 4.8(b), we present the power attenuation due to input signal backoff in optical modulator when DAC and electrical PA are ideal. Although decreasing α_d solves the optical

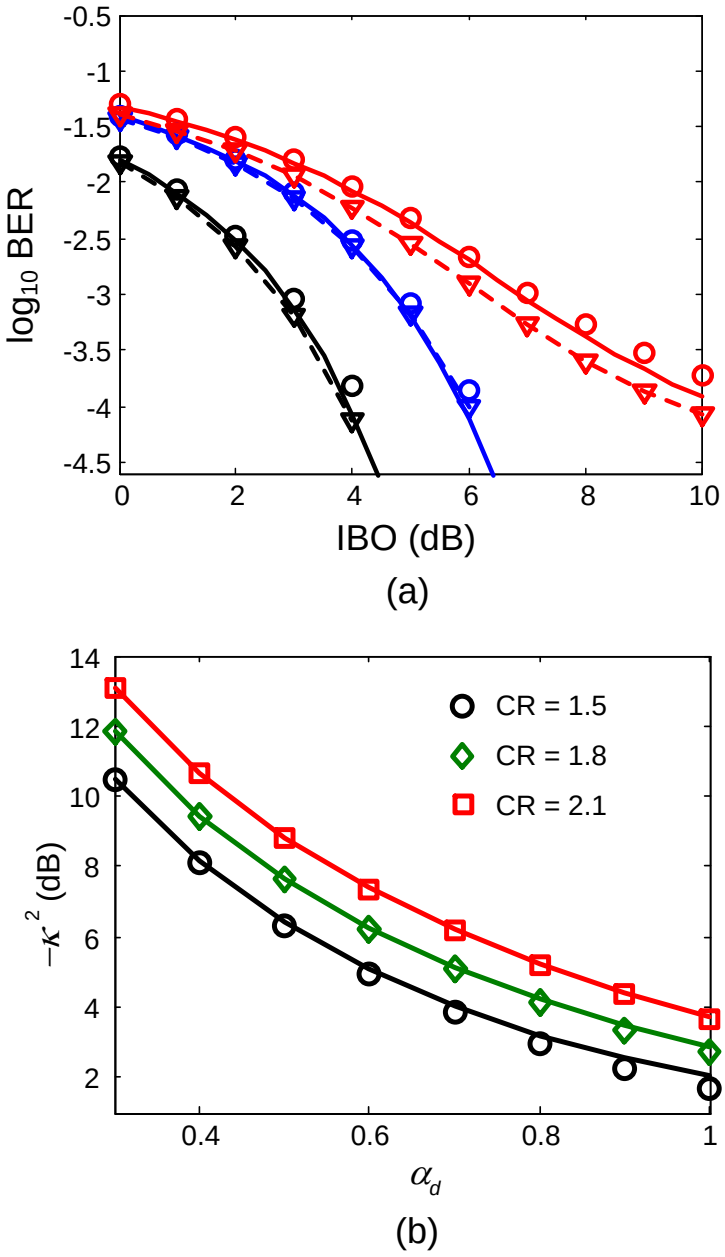

Figure 4.8: (a) BER versus IBO for 16-QAM CO-OFDM. Solid lines refer to BER estimate with side information on nonlinearity, dashed lines with triangle markers refer to BER estimate with a PLI estimate of nonlinearity, and circle markers refer to BER estimate from Monte Carlo error counting. Black: ideal DAC, $\alpha_d = 0.7$; blue: ideal DAC, $\alpha_d = 1$; red: 4-bit DAC with CR $= 1.9$ and $\alpha_d = 1$. The ASE noise power is assumed to be zero. The DAC noise variance is calculated by (4.11) and is equal to $0.013\,\sigma_x^2$. (b) Power attenuation at I/Q modulator due to input signal backoff. Solid lines: κ^2 obtained with side information on nonlinearity; markers: Monte Carlo simulations.

modulator nonlinearity problem, it reduces the power efficiency of the modulator. Therefore, it is essential to use predistortion to suppress nonlinearity while driving the optical modulator in a power efficient regime. We also observe that modulation efficiency increases by decreasing CR; however, if the OFDM signal is over-clipped, the clipping noise will degrade performance. Simulations are in agreement with the theoretical predictions. We notice that the accuracy of theoretical calculations decrease when CR decreases. For low CRs, the assumption of Gaussian distribution for the OFDM signal becomes less accurate. Therefore, theoretical predictions have low accuracy in this regime.

Fig. 4.9(a) and Fig. 4.9(b) show BER versus received SNR, for 4-bit and 5-bit DAC, respectively. Solid lines refer to BER estimate with side information on nonlinearity and markers show Monte Carlo simulation results. When 4-bit DAC is used, transmitter nonlinear function cannot be estimated with sufficient accuracy. In addition, applying predistortion increases PAPR of the DAC input signal which in turn leads to more quantization noise from DAC. Therefore, predistortion gives negligible performance improvement due to inadequate bit resolution. For 5-bit DAC, the nonlinearity characterization with PLI is very accurate and predistortion gives significant improvement. BER is always above FEC threshold of 3.8×10^{-3} without predistortion. When predistortion is employed, received SNR of 18 dB is sufficient to achieve BER below FEC.

4.7 Conclusions

We studied the impact of high PAPR in an optical OFDM transmitter and proposed a simple predistortion scheme to enhance system performance taking into the account the entire transmitter chain of DAC, electrical PA and optical modulator. We used the statistical properties of the PAPR and the distinct nature of the quantization noise from electrical PA and MZM nonlinearity to propose a new predistortion strategy. We apply clipping along with digital predistortion to mitigate performance degradation due to high PAPR without incurring power efficiency degradation. Our simulations show when predistortion is used, BER below FEC threshold of 3.8×10^{-3} can be achieved with a 5-bit DAC, IBO equal to 2 dB and $\alpha_d = 1$ for optical modulator in 16-QAM CO-OFDM. Clipping is known as the simplest PAPR mitigation method and predistortion can be implemented via a lookup table with minimal hardware complexity.

Although optical OFDM technology offers significant benefits for optical networks due to its flexibility, its implementation is more demanding compared to single-carrier systems discussed in the first two chapters. OFDM signals have high sensitivity to frequency synchronization and phase noise. Considering the close subcarrier spacing of OFDM signals, even very little variation of frequency disturbs orthogonality between subcarriers which in turn leads to ICI degrading system performance. As discussed in this chapter, the inherent high PAPR of the

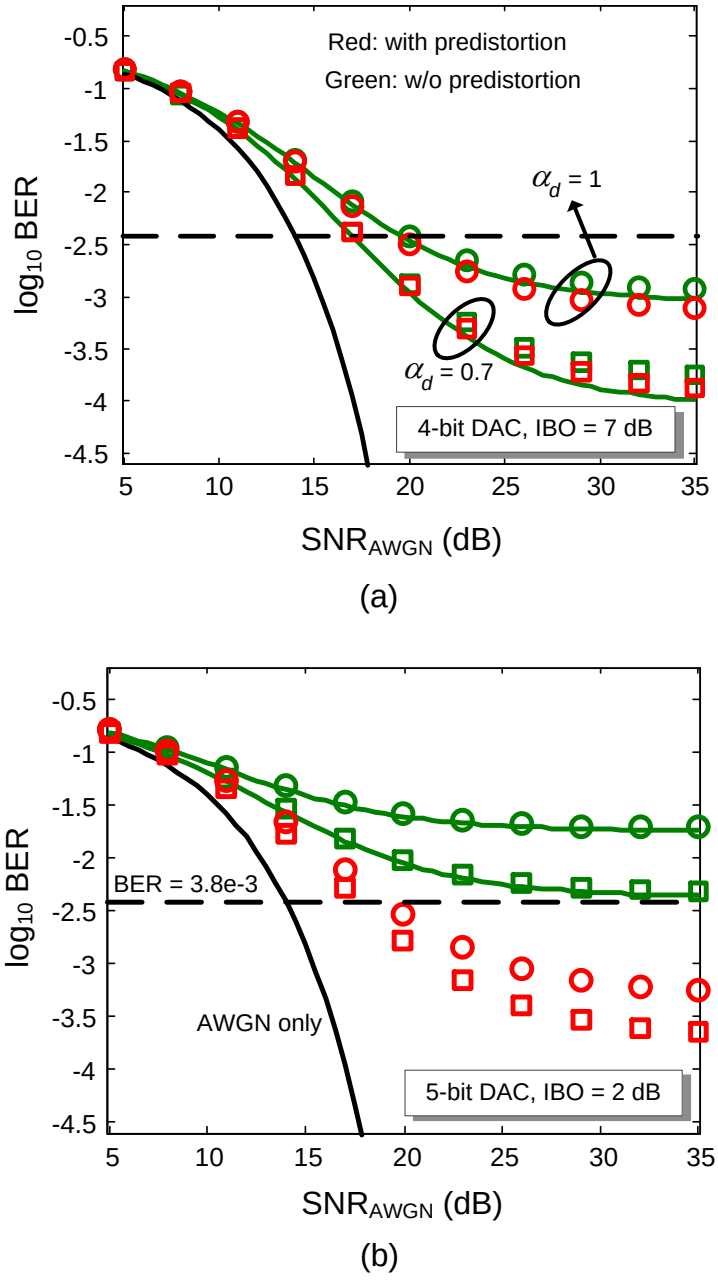

Figure 4.9: BER versus received SNR for 16-QAM CO-OFDM system with (a) 4-bit DAC and CR = 1.9; (b) 5-bit DAC and CR = 2.1. Circles: $\alpha_d = 1$, squares: $\alpha_d = 0.7$.

OFDM signals is another factor that hinders implementation of OFDM systems in optical networks in practice. We presented an effective solution for dealing with PAPR problem of the OFDM systems; however, extensive research should still be done to make implementation of OFDM technology cost-efficient for optical networks.

Chapter 5

DMT Transmission with Optimized QAM Constellations

Abstract

In this chapter, published in [6], we investigate performance of optimized M-QAM constellations in short-reach single-polarization (SP) and DP DMT with direct detection. The constellations are obtained by using an iterative gradient-search algorithm. For the non-square constellations, we find bit-to-symbol mappings with a blind search method. We investigate both of the BER and SER improvement obtained by the designed constellations. This is crucial to quantify the improvement in data transmission rate. The experiments show that data rate can be improved in both SP and DP DMT systems by using optimized constellations instead of square M-QAM. Net data transmission rate of 165 Gb/s and 152 Gb/s is respectively achieved for back-to-back and 2.2 km in a direct-detection DP DMT system assuming FEC threshold of 3.8×10^{-3}.

5.1 Introduction

High capacity short-reach optical communication systems are extensively studied to accommodate bit rate requirements for data centers [71,72]. Implementation of optical systems with high capacity targets can be demanding in a cost-sensitive scenario. With the recent progress in high-speed DACs and ADCs, intensity modulation with direct detection (IM/DD) can be used to achieve 100 Gb/s and higher data rates per channel at low cost. Several modulation techniques are investigated to accommodate the envisioned data rates in a cost-efficient manner [73–78].

DMT modulation, a variation of OFDM, with direct detection is a promising candidate for data centers. DMT is attractive in particular for short-reach optical systems where the optical channel is highly frequency limited due to the use of inexpensive devices (e.g., silicon modulator) and double sideband (DSB) transmission [77]. Optimized bit- and power-loading

in DMT maximize data transmission rate for frequency limited components by careful choice of the modulation format and power of each subcarrier for a given SNR per subcarrier [78].

System capacity can be further improved by expanding the available set of constellations beyond the conventional square QAM, e.g., non-square constellations adapted to the noise characteristics of the channel [5, 79–83]. Square QAM constellations are used for their simplicity, but proper choice of non-square geometries improve performance. In OFDM systems, DACs are an essential part of the system; we do not incur extra complexity at the transmitter when exploiting an arbitrary arrangement of the constellation points in I/Q plane. At the receiver side, complexity increases due to the requirement for a two-dimensional decision unit with look-up table instead of a conventional QAM slicer [84].

Square QAM constellations with Gray coding offer low BER to SER ratio. For irregular constellations, it is not straightforward (or even possible in most cases) to implement Gray coding. Therefore, non-square constellations can suffer an extra penalty due to bit mapping. It is imperative to identify and employ bit mappings with low BER to SER ratio to retain the improvement obtained in SER.

In this chapter, we first explore a short-reach DSB direct-detection DMT system with uniform bit- and power-loading. We will take our learnings from uniform loading and apply them to DMT with optimized bit- and power-loading. For the DMT channel, we use an iterative gradient-search method to generate two sets of optimized M-QAM constellations. Each set contains four constellations, one for each alphabet size (M = 8, 16, 32 and 64) investigated. For the irregular constellations, we find bit-to-symbol mappings that have low SER to BER conversion penalty using a blind search technique. For each constellation size, we investigate SER and BER performance of the three constellation types (standard square QAM and two constellations derived for the channel noise model) in a DMT system with uniform bit and power allocations to all subcarriers. We determine the constellation type offering the best BER performance for each constellation size. Finally, we evaluate BER improvement of the chosen constellations compared to square M-QAM in a direct-detection DMT system with bit- and power-loading. Our experiments study SP and DP systems, both using direct detection. The polarization multiplexing scheme investigated improves spectral efficiency without inducing significant complexity [85, 86].

The chapter is organized as follows. In section 5.2, we discuss the noise sources in short-reach DSB direct-detection DMT and identify two channel noise models. In section 5.3, we describe the methodology for finding symbol positions and a bit-to-symbol mapping in the two non-square M-QAM constellation sets, one for each channel model. Section 5.4 is devoted to the DMT experiments. We explain the experimental setup for SP and DP DMT in section 5.4.1. We present the results for DMT with uniform and optimized loading in section 5.4.2. Section 5.5 concludes the chapter.

5.2 Noise in Short-Reach DMT

Square QAM constellations are not optimal in AWGN [87], but are used for their simplicity. In this section, we discuss under which circumstances direct-detection DMT is an AWGN system, and when a phase rotation (PR) should be taken into account. Understanding the noise distribution motivates our examination of three constellation types. As short-reach systems do not require optical amplification, ASE is not the dominant noise. We describe the noise sources in DMT and the parameters that influence the noise distribution. We use Monte Carlo simulations to explore SNR per subcarrier for various laser linewidths and fiber lengths.

5.2.1 Noise distribution

The optical carrier and the data subcarriers travel at different speeds in optical fiber. This difference during transmission over fiber disturbs their phase coherency, which in turn leads to two noise sources after direct detection: PR and inter-carrier interference (ICI). The PR and ICI arise from the interaction between PN on the laser carrier and chromatic dispersion in fiber in directly detected DMT systems [88]. PR can be approximated by a zero-mean Gaussian random variable influencing the imaginary part of the signal. ICI can be modeled as an additive complex, zero-mean Gaussian random variable. The variance of both PR and ICI increases with increasing laser linewidth and fiber length, or decreasing number of subcarriers. Impairments due to PR become comparable to that of ICI as fiber length increases and number of subcarriers decreases [88]. For short-reach systems, PR is very small compared to ICI.

Ultra-high-speed DACs/ADCs usually suffer from limited bit resolution. Therefore, as discussed in chapter 4, quantization noise is one of the major impairments in high-capacity DMT systems. High PAPR of the signals exacerbates the undesirable effect of quantization. This quantization noise can be treated as AWGN parameterized by the quantization noise power, which is in turn a function of the number of quantization levels [89].

As we examine short links, we assume small (but non-zero) fixed and deterministic PR and group the Gaussian ICI in the Gaussian receiver and quantization noise. The relative effect of PR and Gaussian noise on the constellations depends on system parameters influencing ICI (laser linewidth, fiber length and FFT size) and the other Gaussian noise contributions (DAC bit resolution and receiver noise). We expect constellations optimized for AWGN-only and AWGN with small PR to outperform square M-QAM constellations.

5.2.2 System model and simulations

We evaluate SNR per subcarrier as a function of laser linewidth and fiber length in simulations. QPSK signaling for all subcarriers is simulated assuming an 8-bit DAC with 64 GS/s sampling rate. The DAC is modeled by a 256-level uniform quantizer along with a 33-GHz fourth-order super-Gaussian LPF. We use FFT size of 1024 and Hermitian symmetry to generate the DSB

DMT signal. Eighty subcarriers are left empty in each sideband for oversampling. PN in semiconductor lasers, $\varphi(n)$, is modeled as a Wiener process:

$$\varphi(n) = \sum_{i=-\infty}^{n} u(i), \tag{5.1}$$

where $u(i)$ are independent identically distributed (i.i.d.) Gaussian random variables with zero mean and variance of $2\pi\nu\Delta t$, ν is the laser linewidth and Δt is the sample duration. An optical modulator with no nonlinrsity and zero chirp is considered and optical fiber is modeled as a linear medium with dispersion parameter of 17 ps/(nm·km). A thermal noise-limited receiver is assumed with absolute temperature of 300 K, load resistance of 80 Ω, noise-equivalent bandwidth of 64 GHz and responsivity of 0.6. The received power is 0 dBm. A combination of EVM and BER is used to estimate SNR. At low SNR (< 10 dB), BER gives accurate estimation of SNR; however, for high SNRs errors are too few for accurate BER calculation. Therefore, in this regime EVM is more precise for estimating SNR. EVM can be related to SNR as [90]

$$\mathrm{SNR} = \frac{1}{\mathrm{EVM}^2}. \tag{5.2}$$

Fig. 5.1(a) and Fig. 5.1(b) show SNR as a function of laser linewidth and subcarrier frequency for 2 km and 10 km fiber lengths, respectively. With 10 km we have significant power fading due to chromatic dispersion inducing disparate delays to the two direct-detected signal sidebands. The linewidth dependence is greatly overshadowed by this effect (note the scale where blue is a deep fade of 25 dB). With 2 km we change the SNR scale to focus on penalty with increased linewidth (blue is a 6 dB penalty). We observe that even when fiber length is as short as 2 km, a laser with large linewidth leads to signal degradation. As an example, with a 2-MHz laser source, SNR is 2 dB and 5 dB lower on average compared to a 100-kHz laser when fiber length is 2 km and 10 km, respectively. Note that results shown in Fig. 5.1 emphasize performance degradation due to laser PN and fiber chromatic dispersion without discriminating between ICI and PR.

These simulations establish the dominance of PN-induced noise. In the next section, we find the appropriate constellations for short-reach direct-detection DMT. One set of the constellations is optimized for AWGN without any PR and the other set assumes AWGN with small PR.

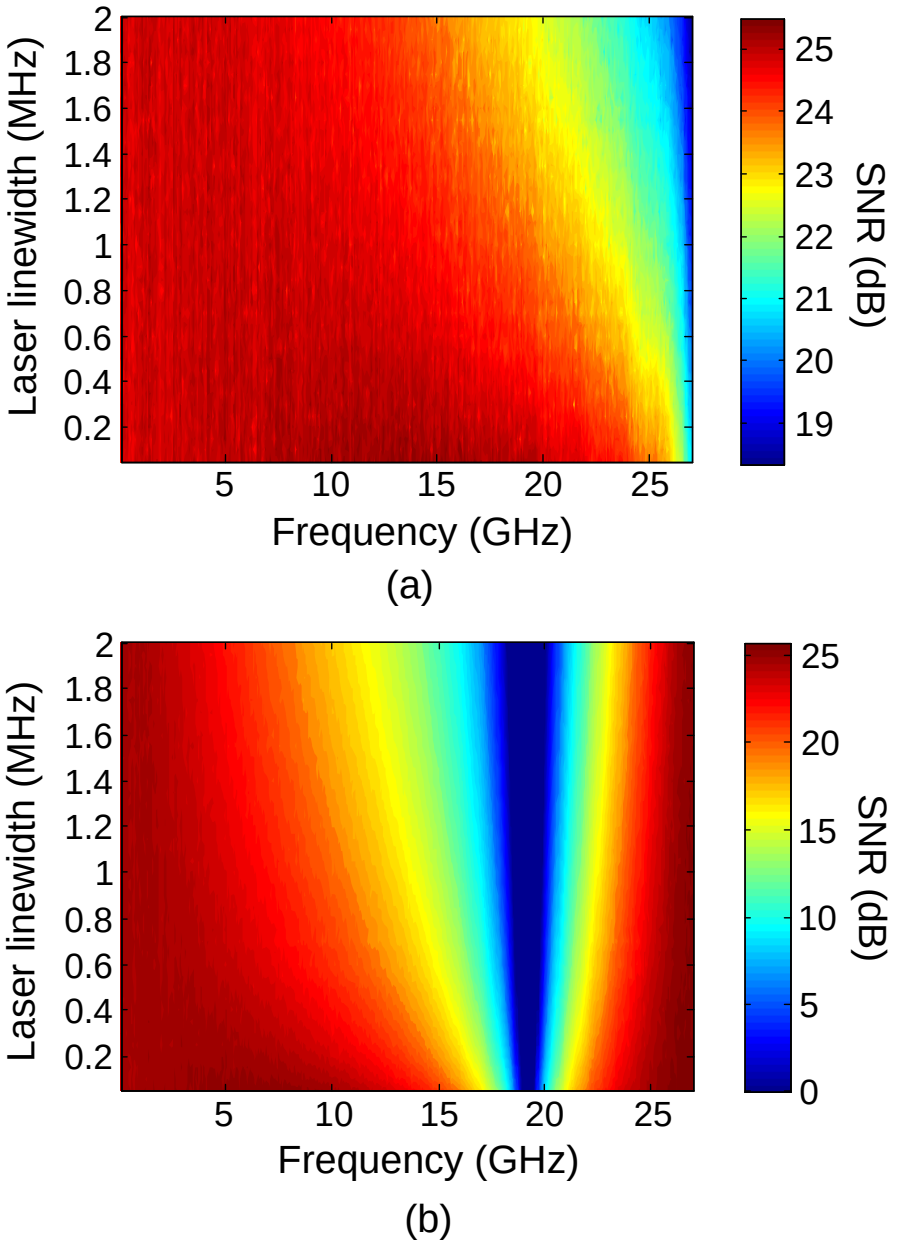

Figure 5.1: SNR as a function of laser linewidth and subcarrier frequency for (a) 2 km and (b) 10 km fiber length.

5.3 Constellation Design

5.3.1 Finding optimal M-QAM constellation

QAM constellations optimized for Gaussian noise are derived by minimizing theoretical symbol error probability for a given transmitted power with a gradient-based algorithm [87]. In [91], this method is adopted to optimize the constellations in the presence of both PN and AWGN. Coherent detection is investigated for both weak and strong PN scenarios [80].

We investigate performance of two M-QAM constellation sets when using direct detection. The first one is optimized for AWGN without any rotation of the received symbols; similar to the constellations studied in [87]. The second constellation set is optimized for AWGN with small PR. In the remainder of this chapter, the standard square M-QAM, the QAM constellations optimized for AWGN without PR and AWGN with PR are respectively referred to as $\mathrm{QAM_{SQ}}$, $\mathrm{QAM_{w/o\,PR}}$ and $\mathrm{QAM_{with\,PR}}$.

In the gradient-search algorithm, four parameters are adjusted to obtain the desired constellation after convergence: Gaussian noise power, step size, initial constellation points and rotation of the transmitted symbols [87,91]. Gaussian noise power is adjusted to achieve SER of about 4×10^{-3}, close to typical FEC thresholds. The step size is between 0.01 and 0.001 on the I/Q plane. Square QAM constellation along with several random constellation points serve for initialization. To find $\mathrm{QAM_{with\,PR}}$ constellations, constant rotation of $\pi/18$, $\pi/28$, $\pi/38$ and $\pi/50$ is considered between transmitted and received symbols in 8-, 16-, 32- and 64-QAM, respectively. These angular offset parameters were selected to ensure that the resulting SER is not significantly higher than the AWGN-only case, i.e., the small PR condition. The algorithm converged to the Fig. 5.2 constellations with less than 5×10^4 iterations.

We note that an exact constellation design requires consideration of all of the system parameters along with their contributions to PR and AWGN. However, it is very difficult (if not impossible) to derive a closed-form solution for SER as a function of all system parameters. The employed approach in finding the constellations and adjusting the parameters of gradient-search algorithm has been proven to provide acceptable accuracy [87, 91]. Furthermore, the gradient-search method is not very sensitive to the Gaussian noise power and the rotation angle when finding the QAM constellations.

5.3.2 Bit-to-symbol mapping

BER is the ultimate figure of merit, which is dependent on bit-to-symbol mapping for the constellation. M!/2 bit mapping options are available for an M-QAM constellation assuming symmetry between “0” and “1”. Testing these options is not feasible for constellations larger than 8-QAM. We adapt the simple blind search technique in [92] minimizing BER, to obtain bit mappings minimizing SER to BER conversion penalty. Let $s_0, ..., s_{M-1}$ denote symbols of

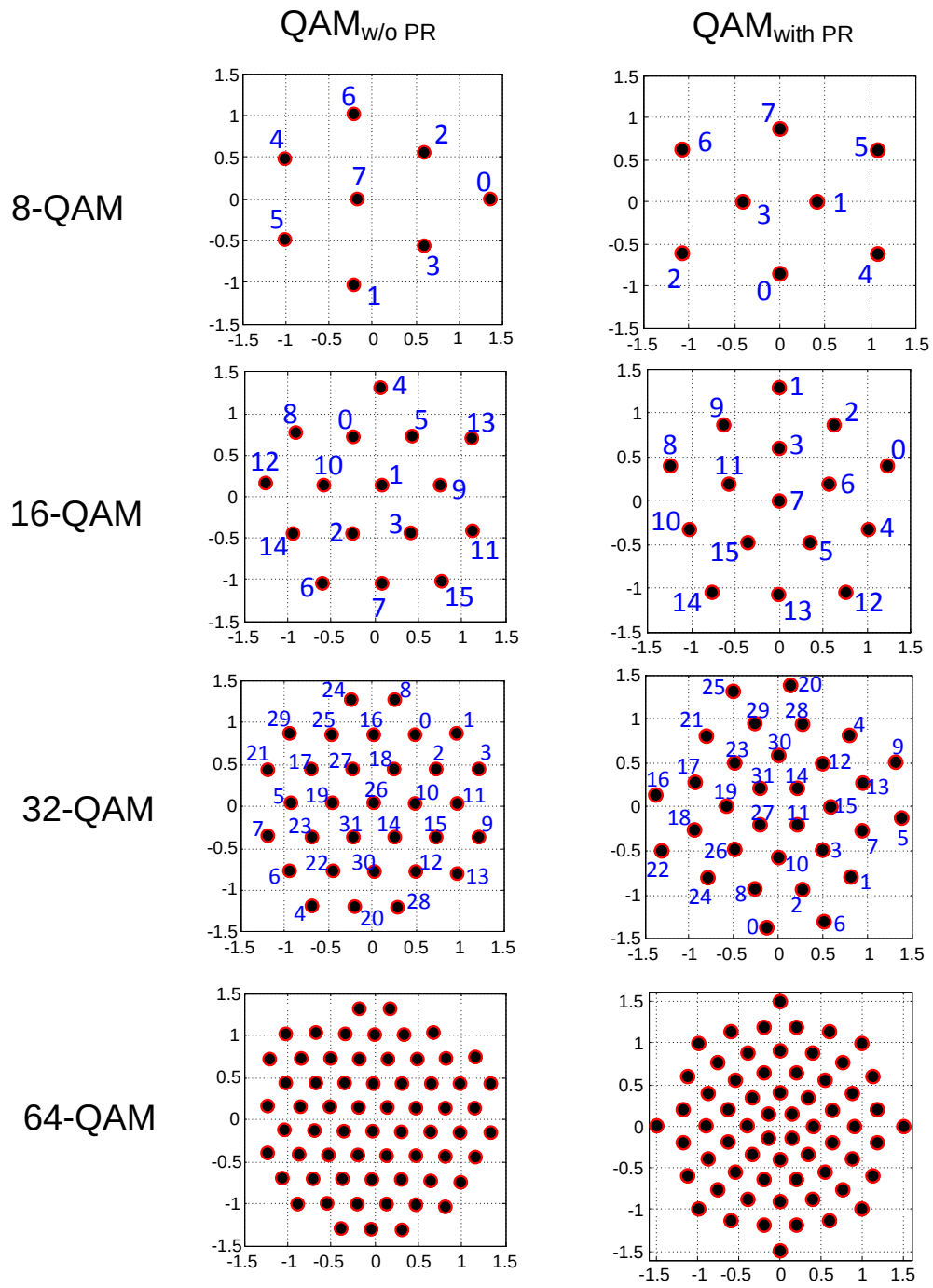

Figure 5.2: Two M-QAM constellation sets optimized for short-reach direct-detection DMT. Bit mappings are given in decimal next to the symbol. $\mathrm{QAM}_{\mathrm{w/o\,PR}}$ is optimized for AWGN without any rotation of the received symbols. $\mathrm{QAM}_{\mathrm{with\,PR}}$ is optimized for AWGN with a very small PR. Detailed coordinates of the symbols for the optimized constellations and square QAM with Gray coding are given in Appendix D.

constellation set S with M points on the I/Q plane. The ratio between BER and SER can be approximated as

$$\beta = \frac{\text{BER}}{\text{SER}} \simeq \frac{1}{kM} \sum_{i=0}^{M-1} \bar{H}_i, \tag{5.3}$$

where $k = \log_2 M$ is the number of bits per symbol and $\bar{H}_i$ is the average Hamming distance between s_i and its neighbouring symbols. Exact calculation would include all constellation points, rather than only neighbouring symbols.

The flow chart shown in Fig. 5.3 describes the bit mapping algorithm for the non-square QAM constellations. The algorithm starts by randomly assigning bits to all symbols and calculating β per (5.3). Then a list of all $\binom{M}{2}$ possible swapping pairs for the assigned bits is generated. Beginning by the first pair in the list the bits assigned to the two symbols are switched and β is recalculated. Whenever a lower β is achieved, the algorithm restarts with the new bit mapping and the first pair in the list. The program ends when all of the pairs in the list are tested. The bit mappings found for the non-square constellations are given in Fig. 5.2. Detailed coordinates of the symbols and bit mapping for the optimized constellations and square QAM with Gray coding are given in Appendix D.

We also find a lower bound for the estimated β by considering the best bit mapping option for each symbol and its neighbouring symbols, regardless of the bits assigned to the other symbols. For each symbol s_i with n_i neighbouring symbols, we assign "0" (in decimal) to s_i and choose a subset with n_i elements from the set of possible decimal bit mappings $\{1, 2, ..., M-1\}$ that minimizes $\bar{H}_i$. This gives a lower bound on $\bar{H}_i$, $i = 0, 1, ..., M-1$. We replace these lower bounds in (5.3) and find a lower bound for β. It is obvious that if $n_i \leq k$, $\bar{H}_{i,LB} = 1$ is the lower bound for average hamming distance between s_i and its neighbouring symbols. If $n_i > k$, the lower bound can be obtained as

$$\bar{H}_{i,LB} = \frac{\sum_{j=1}^{h-1} j\binom{k}{j} + h\left(n_i - \sum_{j=1}^{h-1}\binom{k}{j}\right)}{n_i}, \tag{5.4}$$

where $h \geq 2$ is an integer satisfying

$$\sum_{j=1}^{h-1} \binom{k}{j} < n_i \leq \sum_{j=1}^{h} \binom{k}{j}. \tag{5.5}$$

For the constellations studied in this chapter, $h = 2$ satisfies (5.5) since n_i is smaller than or equal to 6. By replacing $h = 2$ in (5.4), the lower bound simplifies to

$$\bar{H}_{i,LB} = 2 - \frac{k}{n_i}. \tag{5.6}$$

Therefore, the lower bound for $\bar{H}_i$ can be written as

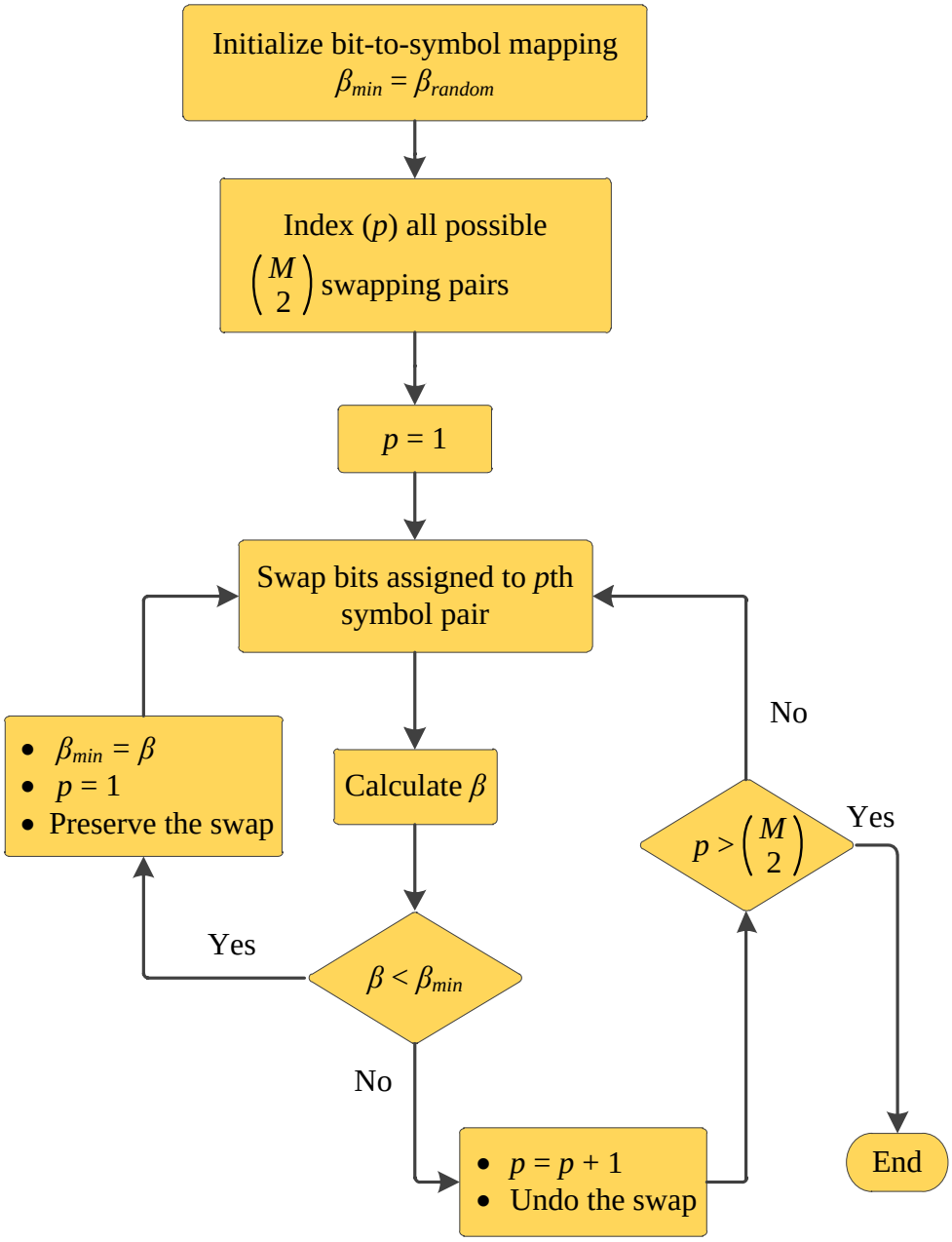

Figure 5.3: Flow chart of the bit-to-symbol mapping algorithm. β_{random}: the ratio between BER and SER for the initial random bit mapping.

$$\bar{H}_{i,LB} = \max\left[1, 2 - \frac{k}{n_i}\right]. \tag{5.7}$$

Replacing $\bar{H}_i$ by $\bar{H}_{i,LB}$ in (5.3) gives the lower bound for the ratio between BER and SER.

Fig. 5.4 depicts the ratio between BER and SER for the bit mappings obtained by the blind search algorithm versus QAM constellation size for $\text{QAM}_{\text{w/o PR}}$ (circles) and $\text{QAM}_{\text{with PR}}$ (triangles). In Monte Carlo simulations, we transmit M-QAM OFDM symbols assuming an AWGN channel and direct detection. We find SER and BER by error counting and calculate β. Monte Carlo simulations (dashed lines) show that estimation of β with (5.3) is relatively accurate for all of the constellations. The obtained bit mappings are close to the lower bound (dash-dot line) for all constellation sizes except 64-QAM. As QAM size increases, the algorithm requires more time to test the bit mappings. Due to the excessive computation time for 64-QAM, it is difficult to investigate a large number of random initial constellations to achieve a bit mapping with low β. We also note that for 8-QAM constellations, all 8!/2 bit mapping options are tested.

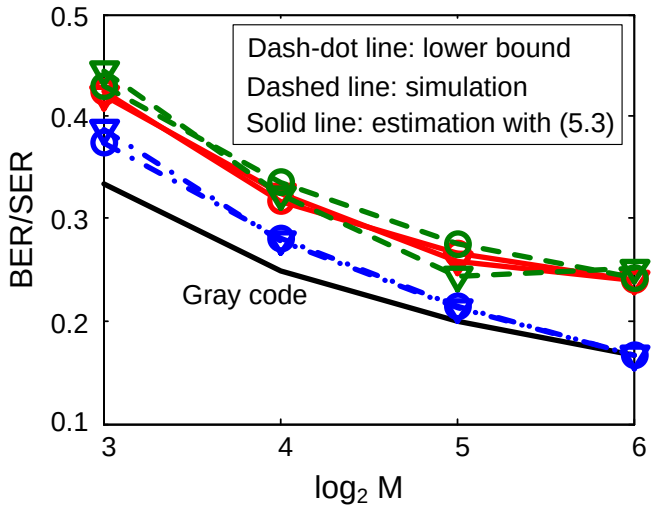

Figure 5.4: The ratio between BER and SER versus QAM constellation size. Circles: $\text{QAM}_{\text{w/o PR}}$, triangles: $\text{QAM}_{\text{with PR}}$.

5.4 Experimental Assessment

In the experiments, we first examine DMT with a fixed modulation format on all sub-channels to evaluate performance of M-QAM options for different constellation sizes. The performance is measured via both BER and SER. We identify M-QAM constellations offering the best BER performance. Afterwards, we turn to DMT with optimized loading and investigate BER performance of the chosen constellations with minimum BER compared to DMT with QAM_{SQ}.

Spectral efficiency can be increased by employing polarization-division-multiplexing (PDM). Several techniques are used for implementing PDM in DDO-OFDM [85]. We adopt a simple PDM scheme, originally proposed for single sideband (SSB) DDO-OFDM, which does not require multiple-input multiple-output (MIMO) processing at the receiver but sacrifices spectral efficiency [86]. In this scheme, the carriers for two polarizations are located at different frequencies and the OFDM signal spectra overlap partially. At the receiver for each polarization, an OBPF is applied to suppress the carrier of the unwanted polarization. In this fashion, each receiver only detects the signal with the same polarization as the surviving carrier. The PDM scheme we use increases spectral efficiency compared to a WDM system, since it allows partial overlap of the signal spectra. While stability of the OBPF center frequency is critical for SSB OFDM systems, DSB signals are much less sensitive to center frequency offset. We verified in our experiments that even with 6 GHz variation of the OBPF center frequency, BER increase is less than twofold (see Appendix E). These features make the employed PDM technique compelling for practical implementation of short-reach PDM DMT.

5.4.1 Experimental setup

Fig. 5.5 depicts the experimental setup for SP and DP DSB DMT with direct detection. Two independent OFDM signals for X and Y polarization are generated offline by Matlab and converted to analog signals by 64-GS/s DACs with 15 GHz bandwidth and 8 bits resolution. Inverse FFT size is 1024 and eight samples are appended to the time-domain signal as cyclic prefix (CP), which leads to 0.78% overhead. Pre-emphasis is employed to compensate for limited DAC bandwidth only when uniform loading is used. For DMT with optimized loading, we estimate SNR by transmitting QPSK signals with the same power on all subcarriers. We do power and bit allocations based on Chow's margin-adaptive algorithm [93]. The amplified DAC signals drive two $LiNbO_3$ MZMs modulating two tones at 1551.72 nm and 1551.45 nm for X and Y polarization, respectively. The MZMs are biased at the quadrature point. The optical carriers are two laser diodes (LDs) with 100 kHz linewidth and 16 dBm output power. The launched power to the fiber is 6 dBm.

For SP DMT, the signals are transmitted over standard SMF. The DMT signals with 4 dBm power are detected by a single PIN PD. For DP DMT, the signals from MZMs are combined by a polarization beam combiner (PBC) to form a PDM signal and transmitted over SMF. At the receiver for each polarization, an OBPF with 4 dB loss rejects the carrier for the unwanted polarization (22 dB suppression). The received power is 0 dBm for both polarizations. The signals after PD are digitized at 80 GS/s by a 30-GHz RTO and processed offline to recover the transmitted data.

At the receiver DSP block, we resample the digital signals captured by RTO and do frame synchronization. We remove the CP and perform an FFT to obtain the frequency-domain signal. We use OFDM preamble symbols for channel estimation in frequency domain. The

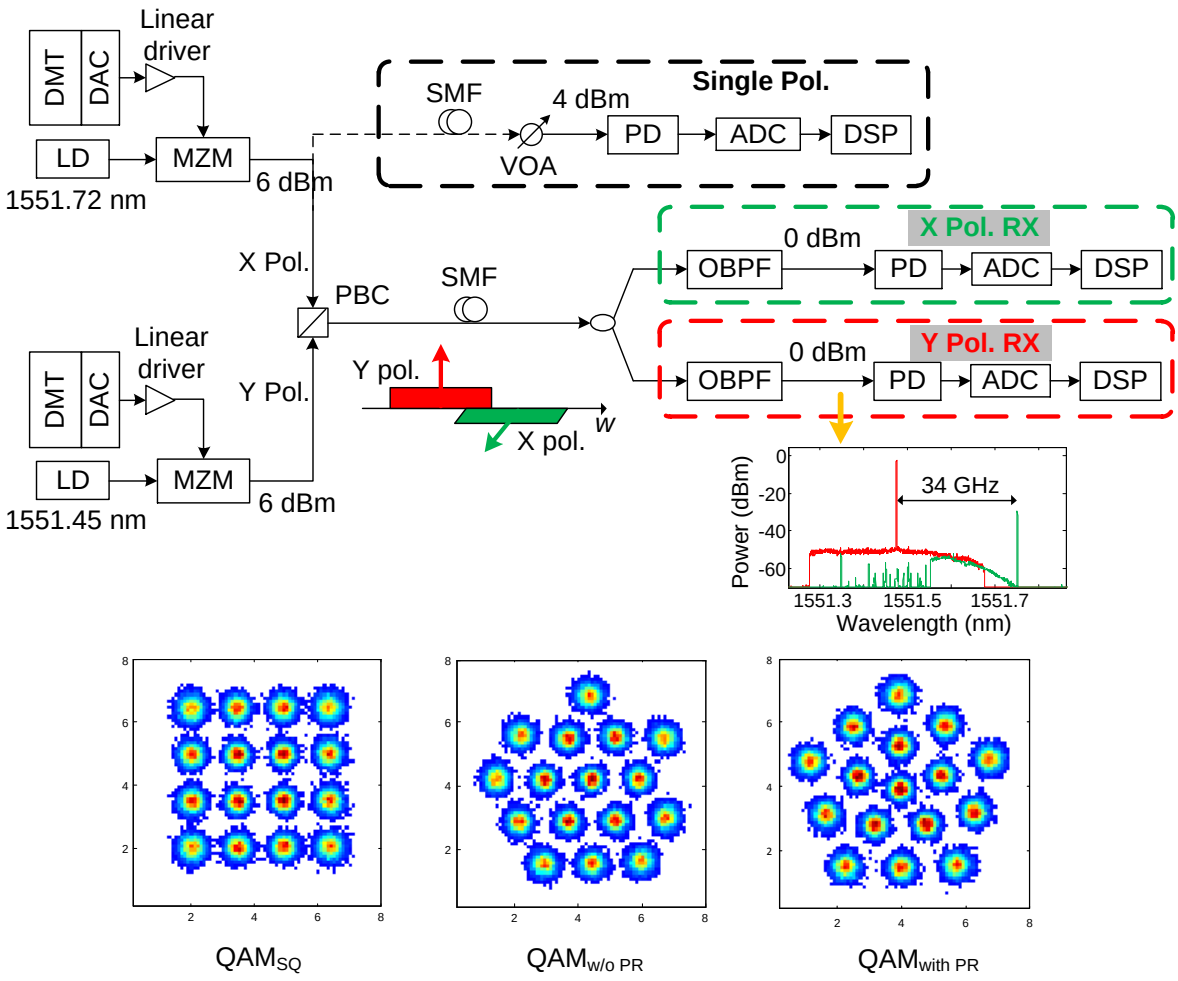

Figure 5.5: Experimental setup for SP and DP DSB DMT with direct detection. Insets: sample recovered 16-QAM constellations and signal spectrum at Y polarization receiver.

overhead due to training symbols is 7.8%. After channel equalization with a single-tap equalizer, decisions are made on the symbols and SER (or BER) is calculated, detecting at least 100 symbol errors. Most of the DSP blocks are the same as the ones used in chapter 4. Detailed description of the blocks are presented in Appendix B. The signal spectrum at the Y polarization receiver is an inset in Fig 5.5. The two polarizations are superimposed to highlight the impact of filtering on both polarizations. Sample recovered 16-QAM constellations are shown in the inset of Fig. 5.5.

5.4.2 Results

Fig. 5.6 shows SER versus raw data rate for SP DMT with uniform loading and different constellation designs for B2B and 2.2 km transmission. Results for B2B and 2.2 km are shown with solid lines and dashed lines, respectively. SER performance of the optimized constellations

is better than that of $\mathrm{QAM_{SQ}}$. The improvement is noticeable for 8-QAM and 16-QAM, whereas 32-QAM and 64-QAM show very small improvement. $\mathrm{QAM_{with\,PR}}$ and $\mathrm{QAM_{w/o\,PR}}$ exhibit similar performance. We also notice the SER degradation due to power fading when signal bandwidth is higher than 25 GHz; see for example the highlighted section of Fig. 5.6(a) for 8-QAM. Note that in the case of DMT with uniform loading, different data rates are achieved by varying the signal bandwidth.

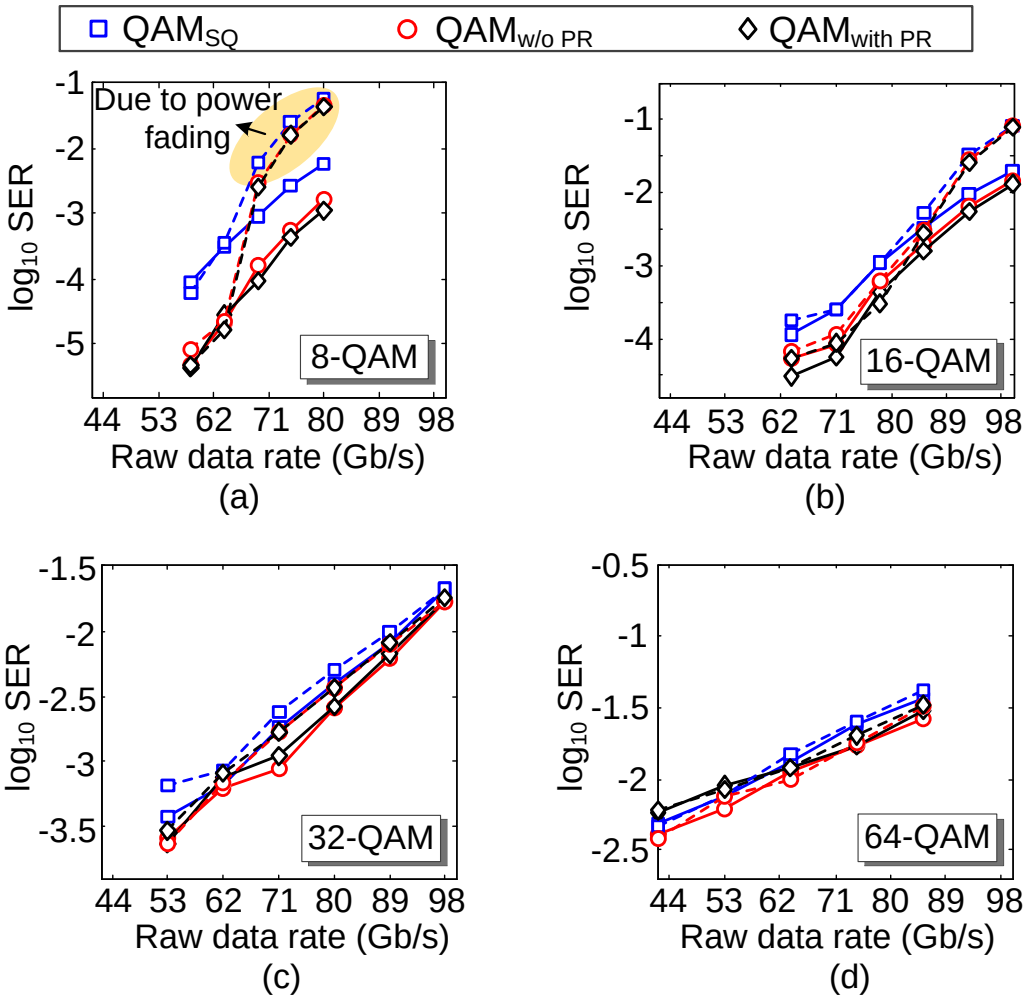

Figure 5.6: SER versus raw bit rate for SP DMT with uniform loading with $\mathrm{QAM_{SQ}}$, $\mathrm{QAM_{w/o\,PR}}$ and $\mathrm{QAM_{with\,PR}}$. Solid line: B2B, dashed line: 2.2 km. (a) 8-QAM, (b) 16-QAM, (c) 32-QAM, (d) 64-QAM.

In Fig. 5.7, we show measured BER versus raw data rate for SP DMT with uniform bit- and power-loading. BER of 3.8×10^{-3} is assumed for the FEC limit with 7% overhead. The improvement in BER is less pronounced than the SER improvement for the optimized constellations. $\mathrm{QAM_{with\,PR}}$ and $\mathrm{QAM_{w/o\,PR}}$ lose performance compared to $\mathrm{QAM_{SQ}}$ after symbol-to-bit mapping. As discussed in section 5.3.2, the ratio between BER and SER for the

optimized constellations is higher than the square QAM constellations with Gray coding. For 8-QAM, the achieved BER improvement is still noticeable. 16-QAM and 32-QAM optimized constellations show very small BER decrease. For 64-QAM, we observe $\mathrm{QAM_{SQ}}$ offers better BER compared to $\mathrm{QAM_{with\,PR}}$ and $\mathrm{QAM_{w/o\,PR}}$.

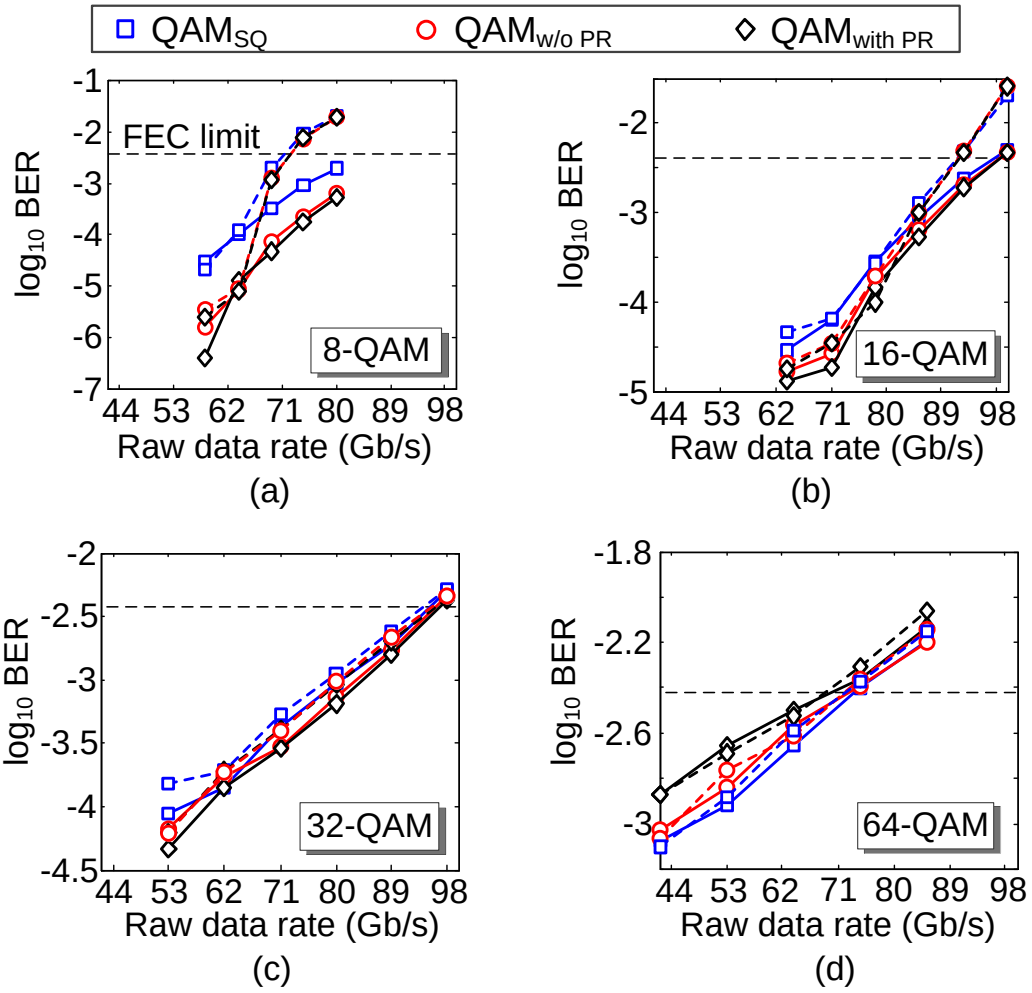

Figure 5.7: BER versus raw bit rate for SP DMT with uniform loading with $\mathrm{QAM_{SQ}}$, $\mathrm{QAM_{w/o\,PR}}$ and $\mathrm{QAM_{with\,PR}}$. Solid line: B2B, dashed line: 2.2 km. (a) 8-QAM, (b) 16-QAM, (c) 32-QAM, (d) 64-QAM.

Average BER of X and Y polarization for 8-QAM and 16-QAM PDM DMT with uniform loading after 2.2 km transmission are shown in Fig. 5.8. Compared to $\mathrm{QAM_{SQ}}$, using $\mathrm{QAM_{with\,PR}}$ and $\mathrm{QAM_{w/o\,PR}}$ leads to 4 Gb/s and 2 Gb/s data rate increase per polarization for 8-QAM and 16-QAM, respectively. Raw data rate per polarization of 66 Gb/s and 76.5 Gb/s with BER below the FEC threshold is achieved for 8-QAM and 16-QAM, respectively. In the DP DMT, the achieved data rate per polarization is lower than the SP system. In addition to crosstalk between the two polarizations, the difference originates from lower received power to the PD

in DP DMT compared to SP DMT (0 dBm versus 4 dBm).

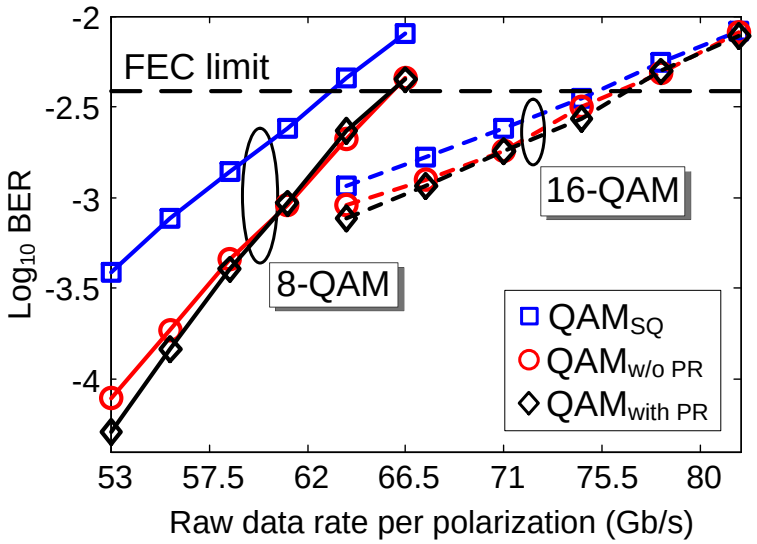

Figure 5.8: Average BER for X and Y polarization versus raw data rate per polarization for PDM DMT with uniform loading with $\mathrm{QAM_{SQ}}$, $\mathrm{QAM_{w/o\,PR}}$ and $\mathrm{QAM_{with\,PR}}$ after 2.2 km.

PN-induced ICI and PR are negligible compared to the other noise sources in our experiments since we use a narrow linewidth laser, hence we expected the constellations without PR to work best. In fact, QAM with PR works slightly better, most likely due to a residual PR when applying the single-tap equalizer. When using a wide linewidth laser, PN-induced effects would be stronger, and QAM constellations designed with the assumption of small PR are expected to still work best.

Bit- and power-loading in DMT improve data transmission rate compared to uniform power and bit allocations for optical communication systems that are frequency-limited. Data rate can be further increased by optimizing the constellation shapes used in DMT. We use the QAM constellations leading to minimum BER for each constellation size, as determined in Fig. 5.7. The best constellation options are: $\mathrm{QAM_{with\,PR}}$ for $\mathrm{M} = 8, 16$ and 32 and standard square for 64-QAM.

In the remainder of this section, we present the experimental results for DMT with optimized bit- and power-loading. We investigate BER performance of the optimized QAM constellations ($\mathrm{QAM_{best}}$) and evaluate the improvement compared to $\mathrm{QAM_{SQ}}$. We also summarize the achieved maximum net data rates with BER below the FEC threshold for different schemes examined throughout this chapter.

Fig. 5.9(a) depicts measured SNR versus frequency for electrical and optical B2B and transmission up to 10 km. Low power of high-frequency subcarriers are due to limited DAC frequency response. Pre-emphasis is not applied as it gives very little data rate improvement for DMT

with optimized loading [94]. Fig. 5.9(b) shows an example of bit and power allocations based on Chow's margin-adaptive algorithm for 92.5 Gb/s SP DMT with 2.2 km transmission. In the DMT with optimized bit- and power-loading, a maximum of 448 subcarriers are used to carry data, which corresponds to 28 GHz electrical DMT signal bandwidth.

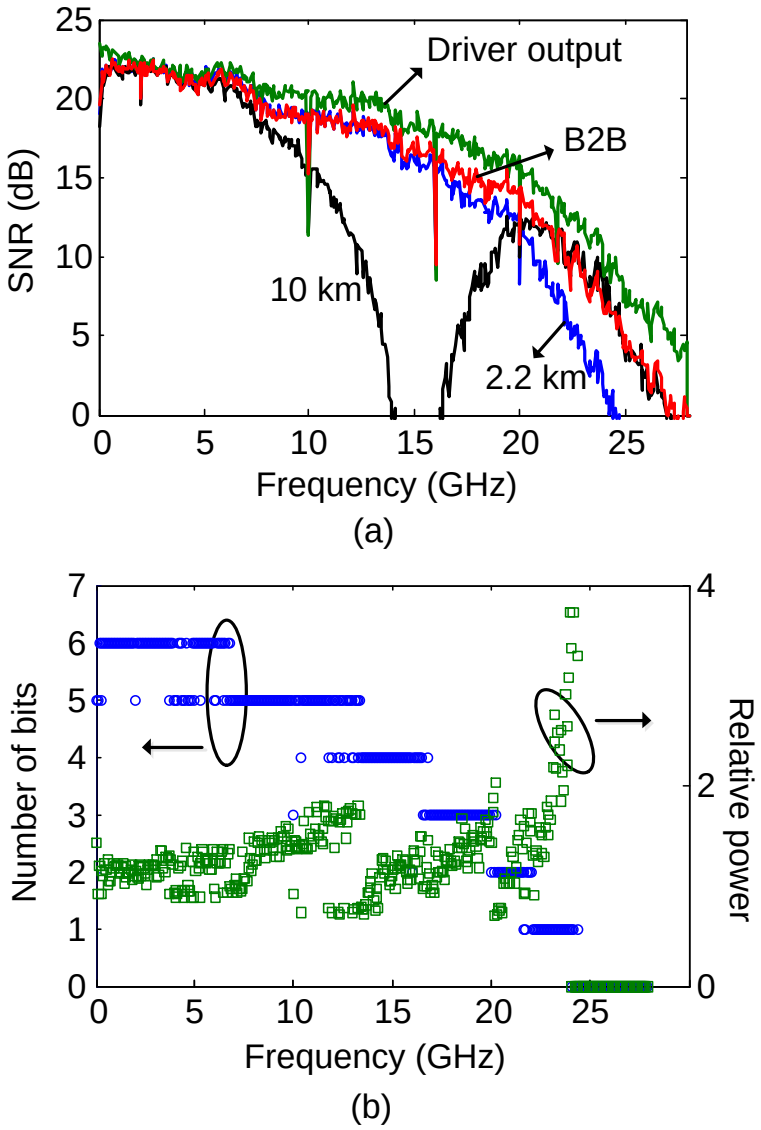

Figure 5.9: (a) Measured SNR versus subcarrier frequency. (b) Bit and power allocations for subcarriers when data rate is 92.5 Gb/s and fiber length is 2.2 km.

Measured BER versus data rate for SP DMT with bit- and power-loading is depicted in Fig. 5.10(a). DMT with QAM_{SQ} and QAM_{best} is shown with squares and circles, respectively. The optimized constellations improve data rate by 4 Gb/s at the FEC threshold. The obtained improvement depends on the bit allocation in DMT. The DMT transmissions with QAM_{best} and QAM_{SQ} differ in 8-, 16- and 32-QAM constellations. If more subcarriers use

these constellations after bit allocation, the performance improvement will be greater.

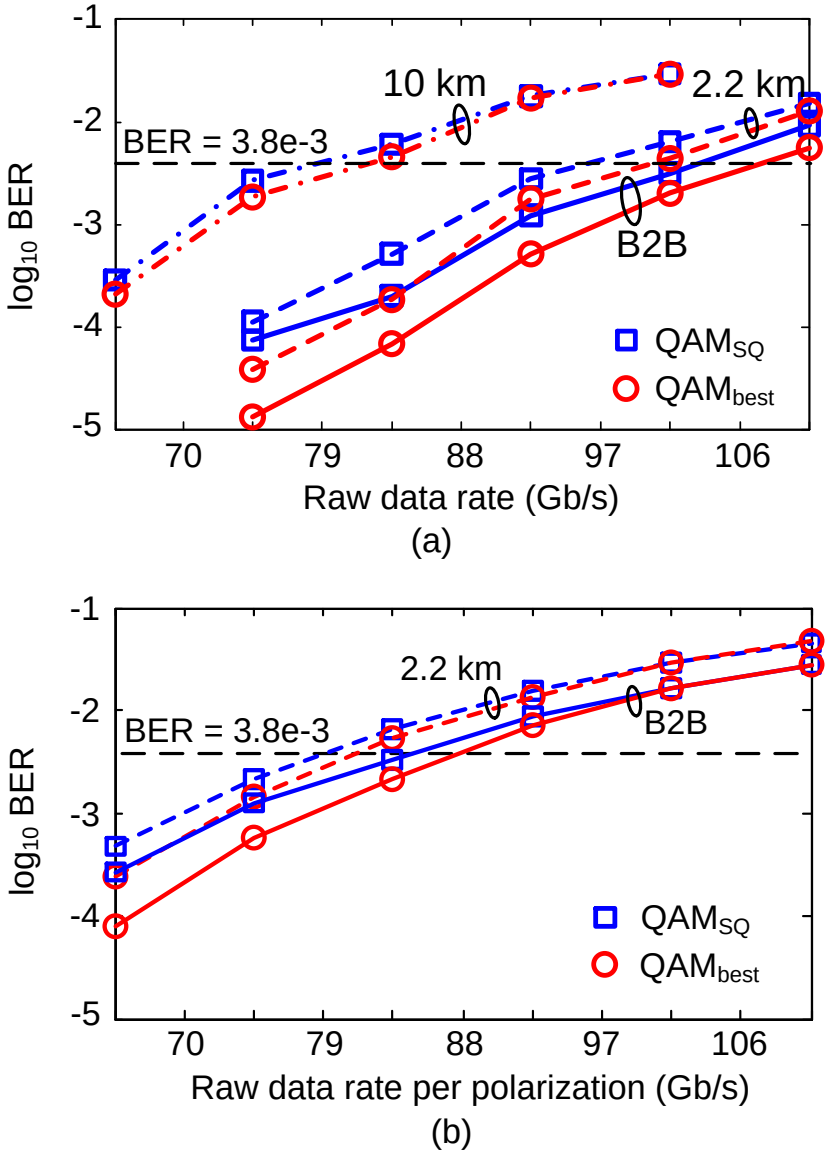

Figure 5.10: (a) BER versus data rate for SP DMT with QAM_{SQ} and QAM_{best} constellations. (b) Average BER for X and Y polarization versus data rate per polarization for DP DMT with QAM_{SQ} and QAM_{best} constellations. Solid line: B2B, dashed line: 2.2 km, dash-dot line: 10 km.

Fig. 5.10(b) shows average X and Y polarization BER versus data rate per polarization for DP DMT with QAM_{SQ} and QAM_{best} constellations. Application of optimized QAM constellations leads to consistent data rate increase for B2B and 2.2 km fiber length. Similar to DMT system with uniform loading, in DP DMT the achieved data rate per polarization is lower than SP DMT. Our PDs had low receiver sensitivity. Employing a more sensitive PD with transimpedance amplifier (TIA), as it was in the previous demonstrations [76,77], can alleviate

Table 5.1: Net data rates (Gb/s) with 7% FEC

	Uniform loading		Optimized loading	
	SP DMT	DP DMT	SP DMT	DP DMT
B2B QAM_{SQ}	91.5	156.5	96.5	159
B2B QAM_{best}	93.5	160	100.5	165
2.2 km QAM_{SQ}	89.5	140.5	90.5	148
2.2 km QAM_{best}	91.5	144	94.5	152

the performance gap between the SP and DP systems.

The net data transmission rates for DMT systems with uniform and optimized loading are summarized in Table 5.1. The total overhead is 15% and includes the overhead due to training symbols for channel estimation, CP and FEC. For B2B system, data rate of 100.5 Gb/s and 165 Gb/s is achieved for SP and DP DMT with optimized loading, respectively. For 2.2 km link, the achieved maximum bit rate is 94.5 Gb/s and 152 Gb/s for SP and DP DMT with optimized loading, respectively. Note that we did not apply error-correcting codes in the experiments; we assumed error-free transmission can be obtained after hard-decision FEC when BER is below 3.8×10^{-3}. Bit- and power-loading in DMT lead to 5 Gb/s bit rate improvement on average compared to a uniform bit and power allocation. Application of optimized constellations gives 3.6 Gb/s data rate improvement on average compared to square QAM constellations.

5.5 Conclusion

We experimentally demonstrate that performance of SP and DP direct-detection DMT can be improved by using optimized M-QAM constellations. The obtained data rate with BER below the FEC threshold of 3.8×10^{-3} is increased by 6 Gb/s for B2B and 4 Gb/s for 2.2 km span in DP DMT with optimized constellations compared to DMT with square QAM. Application of irregular constellations does not incur extra complexity in the transmitter; it only requires application of a two-dimensional decision unit based on look-up table and modification of the decision boundaries at the receiver. The employed polarization multiplexing scheme is feasible for short-reach applications as its implementation does not require expensive components and MIMO processing.

The application of irregular constellations in optical systems has became more attractive with the availability of high-speed DACs. As it is shown in this chapter, the optimized constellations give small but consistent performance improvement. With the current optical systems, it is probably not cost-effective to replace the square QAM constellations by the irregular ones due to increased complexity in decision making at the receiver side. However, with the reduction of hardware implementation cost and introduction of new constellation sets

with better performance, irregular constellations certainly have the potential to be deployed in future optical network architectures.

Part III

Experimental PON Demonstration

Chapter 6

Single-Fiber Lightwave Centralized WDM-OFDMA-PON with Colorless ONUs

Abstract

This chapter, published in [7], demonstrates a carrier-reuse, single-feeder, WDM-OFDMA-PON with colorless direct-detection ONUs and coherent detection optical line terminals (OLTs). We examine two strategies by adjusting the frequency occupancy and the modulation format of the UL and DL signals. We investigate the impact of DL SCR on performance of both UL and DL via simulations and identify impairments limiting system performance. As a proof of concept, we demonstrate on a single wavelength channel, a realization of each of the two scenarios investigated using OFDM. A QPSK approach with wide spectrum and narrow guard band achieves 21.6 Gb/s over 60 km of SMF. A 32-QAM approach with narrow spectrum and wide guard band achieves 14.5 Gb/s and a span of over 80 km.

6.1 Introduction

In the first two parts of this thesis, we examined strategies in single-carrier coherent detection and optical OFDM systems to improve performance of optical networks employing these technologies. Our focus was on demonstrating effectiveness of the studied schemes in optical communication systems. In this chapter, we concentrate on an efficient architecture for PON implementation. The strategies introduced in the first two parts can be deployed in this PON architecture to improve performance.

Research on future optical networks is driven by the growth in bandwidth-intensive applications and the requirement to accommodate data rates in Gb/s. PONs are a promising solution

for fiber-to-the-home due to their cost-efficiency and flexibility. Optimizing PON resources—a single fiber backbone and a distributed carrier being the most important—leads to even more cost-effective systems and decreases service provisioning expenses significantly [95–97].

Limitations in DACs/ADCs would require excessive parallelization and processing for time-division-multiplexing (TDM)-PONs as bit rate scales up. WDM has gained increased attention in the evolving PON standards process to accommodate the demand for high capacity [98]. OFDM is one option for future PONs, with the benefit of flexible bandwidth allocation and resilience in the face of chromatic dispersion. In OFDMA-PONs, sub-bands of the total signal bandwidth can be allocated to ONUs rendering low cost ONUs. Thus, WDM-OFDMA-PON, combining the key advantages of the two strategies, is emerging as a promising solution [99]. All architectures demonstrated in [100–108] exploit DDO-OFDM for DL to minimize signal reception cost at ONU. In [100–104], the UL is also directly detected at OLT receivers. This architecture allows a simple transceiver for both ONU and OLT, but leads to poor performance for the UL signal. Consequently, achieving symmetric bit rates is demanding, especially when resources are shared for the UL and DL.

Another approach is to use coherent detection for the UL signal transmission. Recently, a few PON architectures have been proposed deploying DDO-OFDM for DL and CO-OFDM for UL [105–109]. The underlying reason for this combination is to reduce ONU implementation costs while taking advantage of superior performance for UL with a coherent receiver at OLT, and thus enabling symmetric data transmission rates. In [105], a high-capacity WDM-OFDMA-PON is demonstrated with separate fibers and sets of carriers for UL and DL in a remotely seeded fashion. Schindler *et al.* used a similar approach for UL and proposed an OFDMA-PON with a single feeder fiber and remote heterodyne reception for DL [106]. Implementation of the two architectures requires more components, although they are expected to have superior performance compared to lightwave centralized PONs using a single carrier for both UL and DL. In [107], the same carrier is used for the UL and DL while employing a guard band to avoid interference due to remodulation; however, the DL and UL signals are transmitted over two different fibers with 25 km length. Double feeder PONs are not cost-efficient, although they provide higher reach.

We demonstrate a symmetrical, single-feeder, lightwave centralized OFDMA-PON using an architecture similar to [108,109]. In this PON architecture, one sideband of the signal spectrum is devoted to the DL signal while the other sideband is used for UL transmission. The proposed PON not only allows spectrally efficient signal transmission, but also enables us to use a single laser per WDM channel at the OLT for both DL and UL, enabling colorless ONUs. In [108], a single-fiber symmetrical 25 Gb/s OFDMA-POM is demonstrated with 20 km fiber length by using a single carrier for UL and DL. The main focus of [108] is power budget discussions and resources allocation for UL and DL. In [109], the potential of the single-carrier PON for achieving high UL data rate is experimentally demonstrated by using four WDM channels

(32 Gb/s per channel) and real-time digital signal processing (DSP). Only UL transmission is demonstrated in [109].

In this chapter, we concentrate on investigating the impairments that limit performance of the PON. We examine the impact of backscattering (BS) and particularly remodulation at ONU transmitter on performance of the UL and DL via analysis and Monte Carlo simulations. We demonstrate a proof-of-concept single WDM channel experiment with fiber length up to 80 km. We justify the results obtained in experiments by using the developed equations for the UL and DL signals. Our experiments and simulations study two scenarios for the frequency occupancy and the modulation format of the DL and UL signals. We discuss drawbacks and benefits of each scenario based on the analysis and the results obtained in simulations and experiments.

6.2 Lightwave Centralized WDM-OFDMA-PON Architecture

The key feature of the proposed carrier-reuse PON architecture is using DDO-OFDM for DL and CO-OFDM for UL, allowing a simple ONU transceiver and an OLT coherent detector. SSB transmission of the OFDM signal is employed in the DL, and the other sideband is reserved for the UL to increase spectral efficiency. Fig. 6.1 shows the WDM-OFDMA-PON architecture where w wavelength sources are used to generate multi-band OFDMA signals at the central office. The DSB OFDM signals are filtered to produce SSB OFDM. A guard band is introduced between the optical carrier and the DL signal. The guard band can be easily generated by inserting zero subcarriers in the OFDM signal before IFFT at the transmitter. The SSB OLT signals are fed into an arrayed waveguide grating (AWG) to form a WDM transmission.

The signal is demultiplexed via an AWG after transmission over fiber. Each of the w OFDM signals is then split and distributed to a set of N ONUs. At each ONU, the received signal is split with a passive coupler; one portion of the signal is detected with a single PD and the other portion is remodulated with a reflective optical modulator unit. The UL signal is DSB with two symmetric sidebands. The UL signals from N ONUs are combined and transmitted over fiber after amplification at the ONU and multiplexing at the local exchange.

At the OLT, the received signal is demultiplexed. The sideband with heavy interference can be removed via filtering before detection. The UL OFDM signal is coherently detected via a local oscillator (LO) derived from the transmission source. The choice to filter the UL to SSB at the OLT instead of the ONU allows the ONU to remain colorless.

The proposed PON architecture employs OFDMA in combination with WDM to reach multiple users. In the simulations and experiments, we assume a single WDM channel with OFDM modulation and focus on investigating detrimental PON impairments. The allocation of the

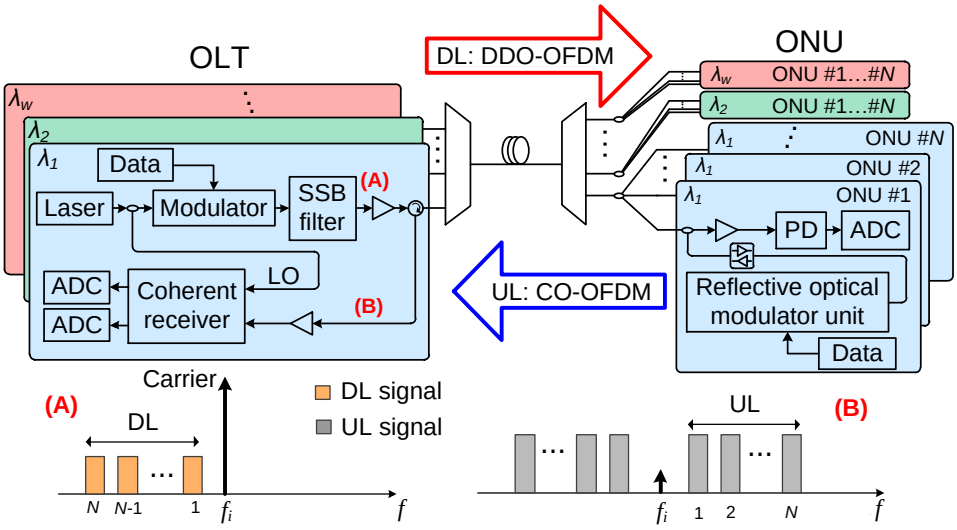

Figure 6.1: Proposed carrier-reuse WDM-OFDMA-PON architecture with colorless direct detection ONU and coherent detection OLT.

resources to multiple users have been studied in previous demonstrations [108].

The main advantage of our proposed WDM-OFDMA-PON is optimally reusing the carrier and bandwidth. One of the major concerns in the carrier-reuse scheme is the residual DL signal that is remodulated with the carrier at the ONU modulator. The signal after the ONU modulator has two terms: 1) the UL signal generated by modulation of the carrier and 2) interference due to remodulation of the DL signal by the UL signal. The second term can interfere with the detected sideband of the UL signal. The remodulation interference (RI) can be mitigated by properly choosing the DL and UL signal frequency bands with appropriate guard bands. Even if the two signals overlap in frequency on one sideband, as we will see in the next sections, the interference can be minimized by reducing the SCR of the DL signal. This leads to OSNR loss for the DL signal which is less critical in short-reach systems. BS is another important issue in single-feeder PONs. It originates from discrete components (e.g., connectors and couplers with limited directivity) or Rayleigh BS in the fiber [110].

In the next section, our main attention is on the impact of BS and RI on performance of the system assuming two different scenarios for the UL and DL signal. We use Monte Carlo simulations to justify our discussions and identify the influence of both RI and BS on the performance of each scenario.

6.3 PON Impairments

The two scenarios we examine are shown in Fig. 6.2. Both cases have symmetric UL and DL data rates, i.e., the same bandwidth and modulation format for UL and DL signals. In the first

scenario, the gap between the SSB DL OFDM signal and the carrier is small. The UL signal has two sidebands with Hermitian symmetry and the left sideband is at the same frequency band as the DL signal (see the first two rows in Fig. 6.2 for case 1). In the second scenario, the gap between the SSB DL signal and the carrier is large enough to accommodate the UL signal bandwidth. The left sideband of the UL OFDM signal is located in the frequency band between the DL OFDM signal and the carrier without any overlap with the DL signal (see the first two rows in Fig. 6.2 for case 2).

The first case uses the available bandwidth efficiently; however, it is more susceptible to the impairments. In the second case, the impairments are not as detrimental as the first case. Therefore, higher-order modulation formats can be used to compensate for inefficient bandwidth usage due to the larger guard band.

In the remainder of this section, we analyze the UL and DL signals in the PON and derive BS and remodulation terms. We employ the developed equations to identify the necessary condition for avoiding RI. We use Monte Carlo simulations to validate the analysis and demonstrate the impact of varying SCR on performance of the UL and DL.

6.3.1 System model

Fig. 6.3 depicts a block diagram of the lightwave centralized PON used for analysis and simulations. The DL signal after the SSB filter at the OLT consists of OFDM data and a carrier to directly detect the signal at the receiver. Let $E_{SSB}(t)$ be the DL signal after the SSB filter given by

$$E_{SSB}(t) = A_c \exp(j2\pi f_c t) \left[1 + \gamma x_{DL}(t)\right], \tag{6.1}$$

where $x_{DL}(t)$ is the baseband SSB DL OFDM signal carrying data with normalized power, f_c is the optical carrier frequency, A_c is the amplitude of the optical carrier and γ^2 is the SCR. To focus on the impairments peculiar to the PON architecture (BS and RI), in the analysis we neglect any other noise and distortion in the system. The DL transmitted signal can be written as

$$E_{T,DL}(t) = \sqrt{\frac{P_{L,DL}}{P_{SSB}}} E_{SSB}(t), \tag{6.2}$$

where $P_{L,DL}$ is the DL launched power to the fiber and P_{SSB} is the power of the signal after the SSB filter. After transmission over the channel, the signal at the input of ONU reflective modulator is written as

$$E_{in,Mod}(t) = \sqrt{P_{R,DL}} E_{SSB}(t), \tag{6.3}$$

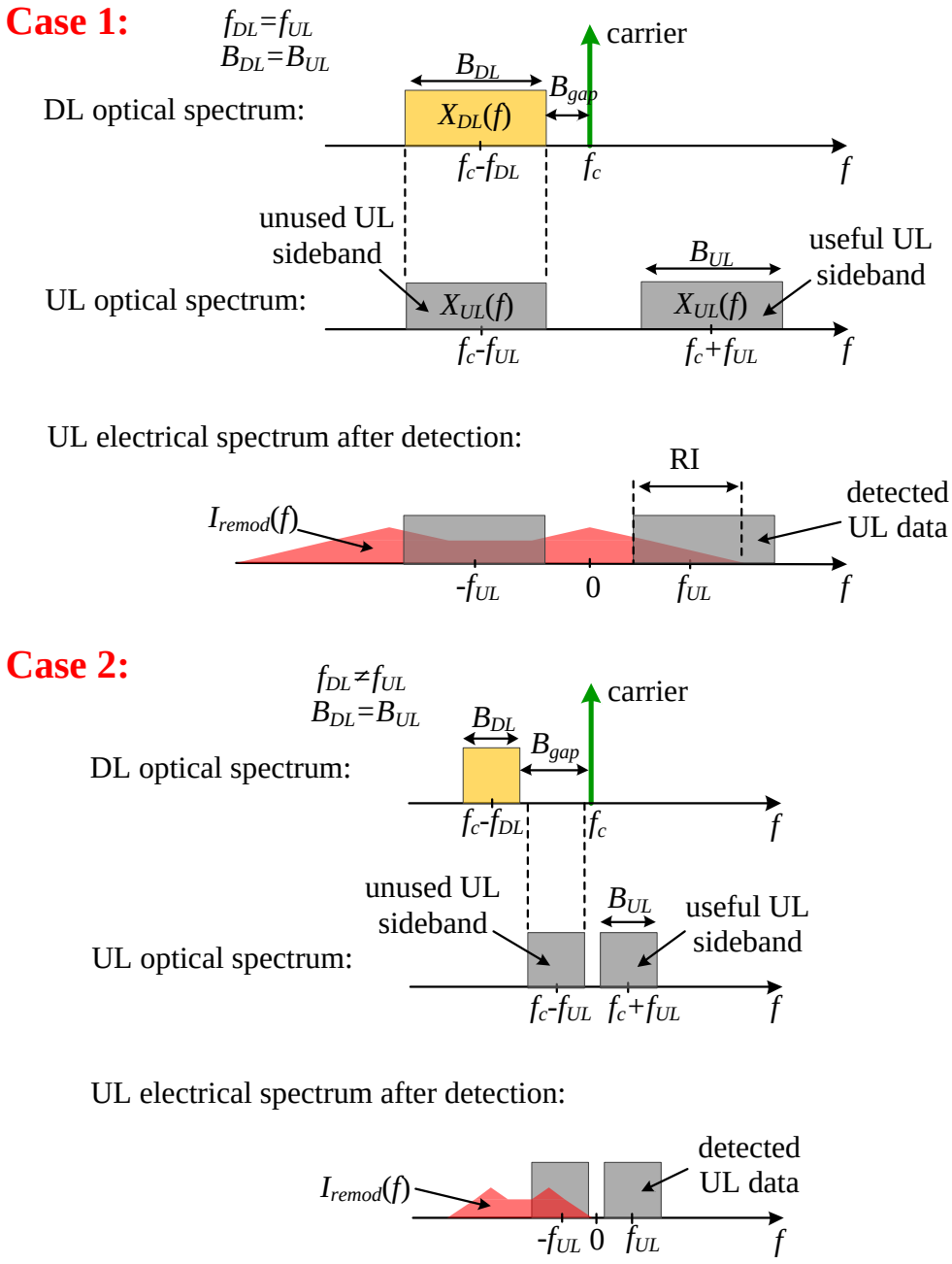

Figure 6.2: Spectra of the DL and UL signal for the two scenarios in the simulations and experiments.

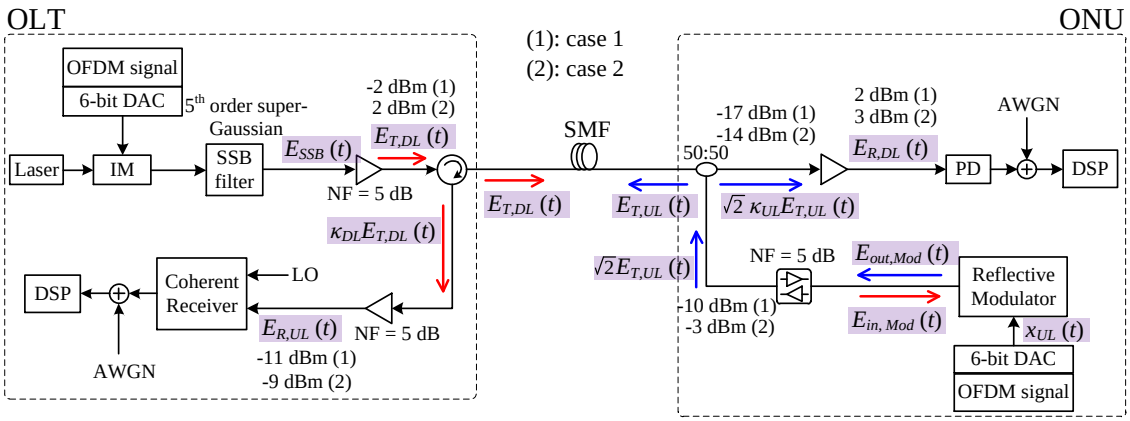

Figure 6.3: Block diagram of simulator with terms from analytic equations shown in shaded text. Powers are indicated at various junctures for each of the two cases studied.

where

$$P_{R,DL} = \frac{P_{L,DL}}{2P_{SSB}} L_{fiber} G_{amp}, \tag{6.4}$$

L_{fiber} is the total fiber loss and G_{amp} is the amplifier gain. Assuming a linear optical modulator with power loss of L_{Mod} at the ONU transmitter, the modulator output signal, $E_{out,Mod}(t)$, can be written as

$$E_{out,Mod}(t) = \sqrt{L_{Mod}} x_{UL}(t) E_{in,Mod}(t), \tag{6.5}$$

where $x_{UL}(t)$ is the DSB UL electrical OFDM signal. By replacing (6.3) into (6.5) and using (6.1) we obtain

$$E_{out,Mod}(t) = A_c \sqrt{L_{Mod} P_{R,DL}} \exp(j2\pi f_c t) x_{UL}(t) + E_{remod}(t), \tag{6.6}$$

where

$$E_{remod}(t) = \gamma A_c \sqrt{L_{Mod} P_{R,DL}} x_{UL}(t) x_{DL}(t) \exp(j2\pi f_c t), \tag{6.7}$$

is the signal generated due to remodulation of the DL OFDM signal by the UL electrical OFDM signal. This remodulation term can interfere with the desired UL OFDM signal given by the first term in the right side of (6.6) and degrade UL performance.

The transmitted UL signal, $E_{T,UL}(t)$, can be expressed as

$$E_{T,UL}(t) = \sqrt{\frac{P_{L,UL}}{P_{R,DL} L_{Mod}}} E_{out,Mod}(t), \tag{6.8}$$

where $P_{L,UL}$ is the UL launched power. Both the received DL and UL signals are affected by the BS in the bidirectional PON. As a result, the received DL and UL signals are respectively

given by

$$E_{R,DL}(t) = \sqrt{P_{R,DL}}E_{SSB}(t) + \sqrt{2G_{amp}}\kappa_{UL}E_{T,UL}(t), \tag{6.9}$$

and

$$E_{R,UL}(t) = \sqrt{L_{fiber}G_{amp}}E_{T,UL}(t) + \sqrt{G_{amp}}\kappa_{DL}E_{T,DL}(t), \tag{6.10}$$

where κ_{UL} and κ_{DL} are the BS coefficients of the UL and DL signals, respectively. The BS coefficients determine the power of the signal in the backward direction.

After direct detection by a square-law PD at the ONU receiver, removing the direct current (DC) term and simplifying, the detected DL signal can be written as

$$\begin{aligned} r_{DL}(t) &= |E_{R,DL}(t)|^2 \\ &= 2\gamma P_{R,DL}|A_c|^2\Re\left\{x_{DL}\left(t\right)\right\} + \gamma^2 P_{R,DL}|A_c|^2|x_{DL}(t)|^2 \\ &+ c_1\left|E_{SSB}(t)\right|^2 x_{UL}\left(t\right) + 2G_{amp}\kappa_{UL}^2\left|E_{T,UL}\left(t\right)\right|^2, \end{aligned} \tag{6.11}$$

where

$$c_1 = 2\kappa_{UL}G_{amp}\sqrt{\frac{P_{L,UL}P_{L,DL}L_{fiber}}{P_{SSB}}}. \tag{6.12}$$

The first term in (6.11) is the desired DL OFDM signal and the second term is the well-known signal-signal beat interference (SSBI) due to direct detection [111]. The third and fourth terms exist due to BS in the PON. Since the BS coefficient is small in practice, the fourth term can be neglected. Simplification of the third term gives the BS signal, $r_{BS,DL}(t)$, after PD as

$$\begin{aligned} r_{BS,DL}(t) \approx\ & |A_c|^2 c_1 x_{UL}(t) + |A_c|^2 c_1\gamma^2|x_{DL}|^2 x_{UL}(t) \\ &+ 2|A_c|^2 c_1\gamma\Re\left\{x_{DL}\left(t\right)\right\}x_{UL}\left(t\right). \end{aligned} \tag{6.13}$$

In (6.13), the first term has only the UL signal, $x_{UL}(t)$. Therefore, for the first scenario where UL and DL have the same frequency band, this term induces interference to the DL signal. However, the first term does not interfere with the DL signal in the second scenario since UL and DL use different frequency bands. The second and third terms in (6.13) induce interference to the DL signal in both scenarios.

For the UL, by replacing (6.2) and (6.8) into (6.10) and using (6.1) and (6.6) the signal after coherent detection can be obtained as

$$r_{UL}(t) = c_2 x_{UL}(t) + i_{remod}(t) + \gamma\kappa_{DL}A_c A_{LO}\sqrt{\frac{P_{L,DL}G_{amp}}{P_{SSB}}}x_{DL}\left(t\right), \tag{6.14}$$

where

$$c_2 = A_c A_{LO}\sqrt{P_{L,UL}G_{amp}L_{fiber}}, \tag{6.15}$$

A_{LO} is the LO amplitude, and

$$i_{remod}(t) = c_2\gamma x_{DL}(t)x_{UL}(t), \tag{6.16}$$

is the RI. As illustrated in the third row of Fig. 6.2, the remodulation term shown by triangular (red color) spectra does not interfere with the detected sideband of the UL signal (upper-frequency sideband) in the second scenario. However, it induces interference to the UL signal in the first scenario. By taking the Fourier transform of $i_{remod}(t)$ and comparing its frequency band to the frequency band of the UL signal, it is straightforward to obtain the condition for preventing interference to the UL signal as

$$B_{UL} \leq B_{gap}, \tag{6.17}$$

where B_{UL} is bandwidth of the UL OFDM signal and B_{gap} is bandwidth of the guard band (gap) between the DL signal and the carrier. This condition is met in the second case. Thus, the remodulation term does not induce any degradation to the signal in this case.

The third term in the right side of (6.14) is the BS induced to the UL signal. The backscattered signal and the detected UL signal are at different sidebands. Therefore, contrary to DL, BS does not degrade UL signal performance.

6.3.2 Simulations

We turn to simulations to validate our predictions for the two scenarios. In the simulations, the IFFT size is 256. Eight samples are added to each OFDM symbol as a CP to enable efficient channel equalization at the receiver. In the first scenario, a QPSK DL signal occupies a frequency band from 2 GHz to 13 GHz at the left side of the carrier. The DSB QPSK UL signal occupies the frequency bands at both sides of the carrier. Each of the DL and UL signal has 100 data-bearing subcarriers.

In the second scenario, a 32-QAM DL signal has a bandwidth from 4.8 GHz to 7.9 GHz and the UL signal has a bandwidth from 0.65 GHz to 3.9 GHz on both sides of the carrier. Each of the DL and UL signals has 28 data subcarriers. The bit rate is 21.6 Gb/s for the first scenario and 14.5 Gb/s for the second scenario.

Two pre-emphasized pilot subcarriers are inserted in the UL OFDM signal for phase noise compensation (50^{th} and 80^{th} subcarrier for the first case and 20^{th} and 30^{th} subcarrier for the second case). The DAC is modeled as a 6-bit quantizer with 13 GHz analog bandwidth and 28 GS/s sampling rate. In our experiments, limited ENOB for the DAC was the main limiting factor in achieving higher bit rates for the second scenario, which is not modeled in the simulations. Therefore, it would be possible to obtain the same bit rate for the first and second case in the simulations. However, we simulate the more realistic situation where bit rates would vary due to DAC impairments. The bit rates simulated reflect those we were able to achieve in our proof-of-concept experiments.

The laser source at the OLT with 10 kHz linewidth is modulated by an intensity modulator (IM) with no nonlinearity and bandwidth much larger than the signal bandwidth. A fifth-

order super-Gaussian filter is used to remove one sideband of the DL OFDM signal. SMF is modeled as a linear medium with dispersion parameter of 16 ps/nm·km. The amplifiers have a noise figure (NF) of 5 dB. The ONU receiver is a square-law detector and the OLT coherent receiver uses a 10 kHz laser as LO. The transmitted and received powers are given in Fig. 6.3 for both cases. The powers are adjusted according to our experimental setup described in section 6.4. Thermal noise-limited reception is assumed with -13 dBm and -24 dBm AWGN power for the DL and UL receiver, respectively. The BS coefficients are $\kappa_{UL} = \kappa_{DL} = -42$ dB, as measured in the experiments.

Fig. 6.4(a) shows DL BER versus DL SCR for the two cases. For the first case, SSBI given by the second term in (6.11) degrades performance of the DL when SCR is high. As we decrease SCR, the SSBI decreases leading to a better BER. Further decreasing SCR from the optimum value of -16 dB increases BER due to the BS and the amplifier noise. From (6.11), we know that the desired DL OFDM signal is proportional to $\gamma|A_c|^2$. On the other hand, the first term in the BS signal given by (6.13) depends on carrier power, $|A_c|^2$. Therefore, as γ (or SCR) decreases, the ratio between desired DL OFDM signal and BS signal decreases resulting in performance degradation.

For the second scenario, the SSBI does not degrade the DL OFDM signal performance [111]; we observe a BER floor at high SCR due to DL receiver noise. As discussed before, the first term of the BS signal does not interfere with the DL signal in this case. Therefore, the main limitation at low SCR is due to the amplifier noise. BER results without BS is also shown in Fig. 6.4(a) to confirm our discussions. We observe that BS has negligible effect on BER in the second case; however, it has considerable impact on BER in the first case.

Fig. 6.4(b) shows BER of UL signal versus DL SCR. The RI given by (6.16) increases as DL SCR increases. Since the first case does not respect the condition given in (6.17), RI induces significant degradation to the UL signal as SCR increases. We observe slight performance degradation for the second case by increasing SCR. Increasing DL SCR decreases power of the carrier available for UL remodulation. This power decrease in the useful portion of the UL OFDM signal leads to OSNR loss and degrades signal performance; however, the degradation is not significant as compared to the first case.

6.4 Experimental Setup and Spectral Effects

Fig. 6.5 depicts the experimental setup for single channel PON with OFDM. As a reflective MZM is unavailable, we replace the reflective optical modulator unit of Fig. 6.1 with non-reflective MZM and an optical circulator. At both OLT and ONU transmitters, independent QAM OFDM signals are generated using PRBSs with the length of $2^{21} - 1$.The parameters used for OFDM signals are similar to our simulations presented in section 6.3.2. After taking IFFT and adding CP in Matlab, the generated signals are loaded into memory of two field

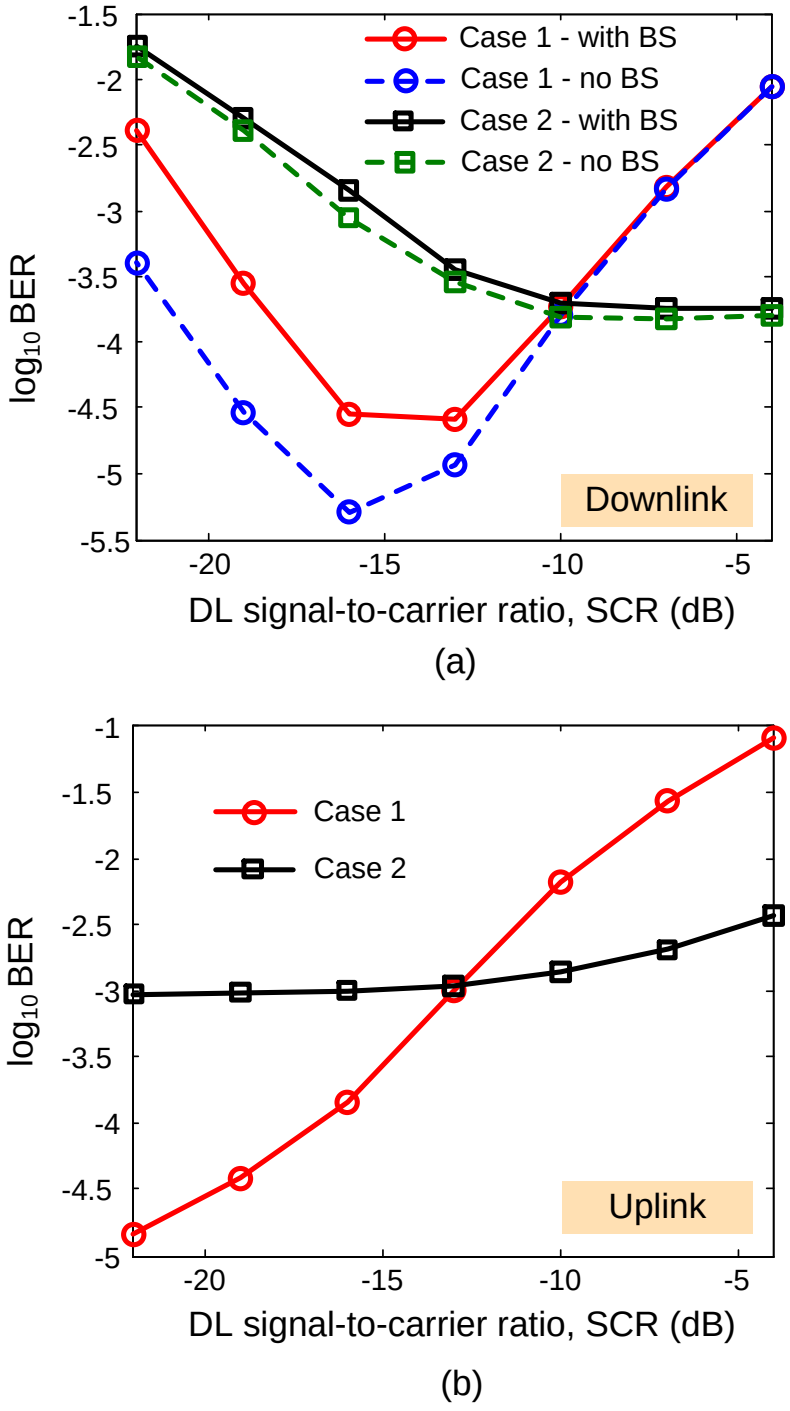

Figure 6.4: BER simulation results versus DL SCR for the two scenarios. (a) DL, (b) UL with BS.

programmable gate arrays (FPGAs) and then converted into analog signals using DACs with 6 bits resolution operating at 28 GS/s. The electrical OFDM signals from DACs are amplified and drive two MZMs (Fujitsu FTM7937EZ-A and FTM7938EZ), one for ONU and one for OLT. At the OLT, an ECL at 1546.62 nm with 10 kHz linewidth is modulated by an MZM biased at quadrature. To decrease the power fading effect, an optical SSB filter (Yenista XTM-50) rejects one OFDM sideband (see Fig. 6.5A). The signal power is adjusted to −2 dBm for the first case and 2 dBm for the second case with a VOA after amplification via EDFA.

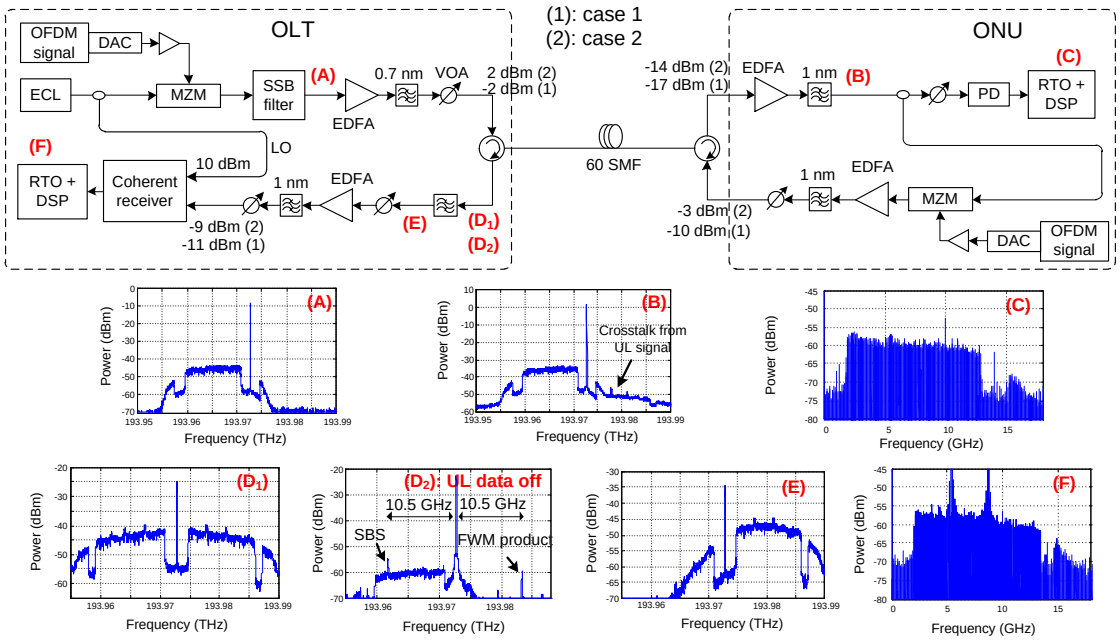

Figure 6.5: Experimental setup for single channel OFDMA-PON. Inset: signal spectra at 0.8 pm (100 MHz) resolution. (A) DL signal spectrum at the OLT after SSB filter; (B) DL signal spectrum at the ONU receiver; (C) Received electrical DL signal spectrum; (D_1) UL signal spectrum at the OLT before SSB filter; (D_2) Spectrum of the UL signal when UL data is turned off; (E) UL signal spectrum at the OLT after SSB filter; (F) Received electrical UL signal spectrum.

The OFDM signal is launched into standard SMF. We assume splitting loss at the ONU can be compensated for with the ONU optical amplifier. The ONU received signal is split (3-dB coupler) with one output detected by a PD (u2t XPDV3120R), and the other output fed into a $LiNbO_3$ MZM biased at the null point after manually adjusting the polarization. The UL OFDM signal is then amplified and launched back into the channel. The UL launched power is −10 dBm and −3 dBm for the first and second case, respectively. Note that the VOAs are not required for the PON implementation; they are used to control the signal power. Furthermore, while we use EDFAs for convenience, as discussed in chapter 2, application of SOAs are preferred in the ONU because of their cost-effectiveness, integrability and wide spectral gain. The simple DFBP technique can be used to mitigate the induced nonlinear distortions from

SOA. At the OLT receiver, the lower sideband of the OFDM signals is filtered with a tunable optical filter (see Fig. 6.5D_1 and E) and then coherently detected with an LO. The detected signals at both ONU and OLT are digitized using a RTO and processed offline. The spectrum of the received signal for ONU and OLT is shown in Fig. 6.5C and F, respectively.

We note that while employing the SSB filter before the coherent receiver improves receiver sensitivity, when removing the filter we can still obtain acceptable performance given that the coherent receiver input power is increased and the carrier is suppressed effectively at ONU modulator. We also note that the MZMs used in our experiment are polarization sensitive; however, they can be replaced by polarization-independent reflective MZMs [112].

Fig. 6.5B shows the spectrum of the DL OFDM signal after transmission; this is remodulated at the ONU transmitter. There is crosstalk induced by the DSB UL signal to the DL signal. Note that we avoid using an SSB filter at the ONU transmitter to have a simple colorless ONU. The observed crosstalk is mostly due to limited directivity of the optical circulator ($\sim 42\,\mathrm{dB}$) and partly because of BS from discrete components and Rayleigh BS. We categorize all of these effects as BS. We used low launched power at the ONU to minimize DL signal performance degradation. However, when using a reflective optical modulator, limited directivity of the coupler at ONU (rather than optical circulator) can lead to crosstalk. Couplers with directivity of as high as 55 dB are commercially available, providing 13 dB more protection than our experimental demonstration. In our experiments, we show that even in the worst case scenario when the UL and DL signals use the same frequency range at two sides of the carrier (first case) BER below FEC threshold of 3.8×10^{-3} (7% overhead) can be achieved.

Fig. 6.5D_2, taken at the OLT receiver after the circulator, shows the impact of stimulated Brillouin scattering (SBS) on the UL signal. We turned off the electrical UL OFDM data to highlight the SBS effect from the DL signal. SBS is caused by the $\chi^{(3)}$ nonlinearity in the fiber and occurs at slightly lower frequencies than the incident light in the backward direction. Since the high-frequency sideband is used for the UL signal transmission, SBS from the DL signal is not at the same sideband as the UL signal. However, due to presence of the SBS tone and the carrier in the UL direction, they interact with each other through FWM phenomenon and create a third tone at the high-frequency sideband (see Fig. 6.5D_2). The FWM product of the carrier and SBS occurs at $\sim 10.5\,\mathrm{GHz}$ spacing from the carrier. As we will see in section 6.5.1, the distortion from FWM product affects only a few subcarriers (two in our case). Hence, it is not a major problem in the proposed PON and can be easily avoided by properly designing the subcarrier structure for the UL signal.

6.5 Experimental Results

6.5.1 First case: QPSK experiment

Fig. 6.6(a) depicts BER versus received power for 21.6 Gb/s bidirectional QPSK OFDM signal which corresponds to the first scenario as described in the previous sections. The received power is measured before PD for the DL and before the EDFA at the OLT receiver for the UL. The SCR of the DL signal is −17 dBm. For the DL signal, performance is limited due to receiver noise. The PD used does not have a TIA and the receiver sensitivity is low compared to previous PON demonstrations with direct detection for DL [102]. This limitation is not related to the architecture of the PON and can be alleviated by employing a commercially available PD-TIA with high sensitivity at the ONU.

The UL signal has superior performance compared to the DL signal due to coherent detection. BER is below the FEC limit of 3.8×10^{-3} for the swept received power range. As we showed in the simulations, decreasing DL SCR decreases RI in UL. By using low SCR for the DL signal (−17 dBm), the RI in the UL is reduced in the experiments. We also show the DL signal BER results when the UL data is turned off to see the impact of BS. We observed 0.5 dB power penalty at BER equal to FEC threshold of 3.8×10^{-3}. Lower BER floor is achieved when BS is eliminated by turning off the UL data. This confirms our observation in simulations for DL signal for the first case.

In Fig. 6.6(b), EVM versus subcarrier index is shown for the UL and DL signal with 60 km SMF. All subcarriers achieve EVM less than the FEC limit. We notice that two subcarriers (at ~ 10.5 GHz) suffer distortion coming from FWM of the carrier and SBS in the UL. Although the induced distortion is not severe due to low launched power to the fiber, it can be avoided entirely by considering a few null subcarriers at the Brillouin frequency shift. The SBS nonlinear effect is observed at relatively low powers—the threshold for SBS is approximately 2 dBm [113]. Hence, the launched power per channel must be below the threshold power to avoid significant power saturation and attenuation due to SBS.

6.5.2 Second case: 32-QAM experiment

Fig. 6.7 shows BER versus fiber length for 32-QAM OFDM signal. We were able to increase the launched power for the DL and UL signal to 2 dBm and −3 dBm, respectively, since the second case is less vulnerable to RI and BS as discussed in section 6.3. The power at the input of DL PD and UL coherent receiver is 3 dBm and −9 dBm, respectively. The results show that system reach can be extended to 80 km in the second case achieving BER below hard-decision FEC limit of 3.8×10^{-3}.

For the DL, the observed performance degradation when increasing fiber length is due to increased BS interference from the UL signal to the DL signal. As (6.11) indicates, by increasing

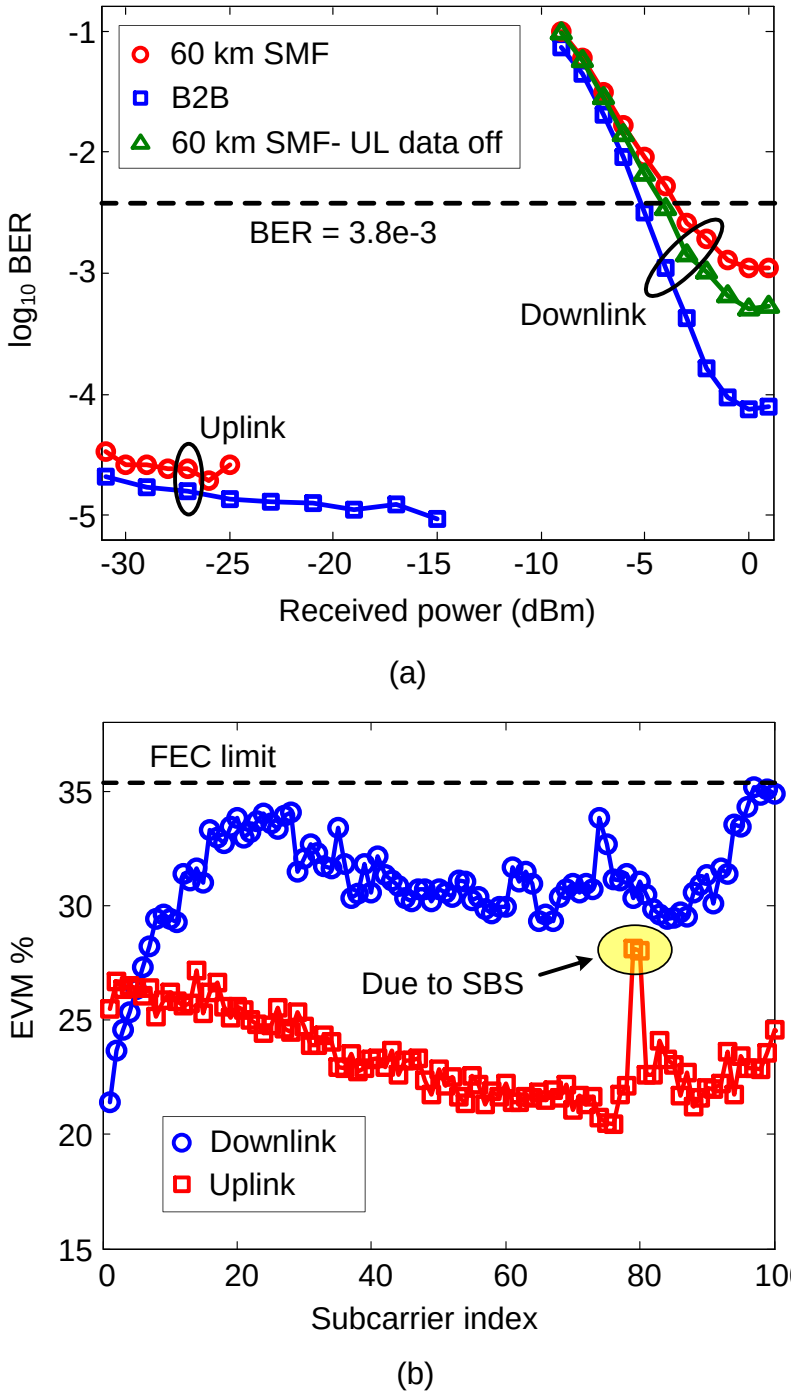

Figure 6.6: Experimental results for 21.6 Gb/s bidirectional QPSK OFDM. (a) BER versus received power. (b) EVM versus subcarrier index for the DL and UL signal with 60 km SMF.

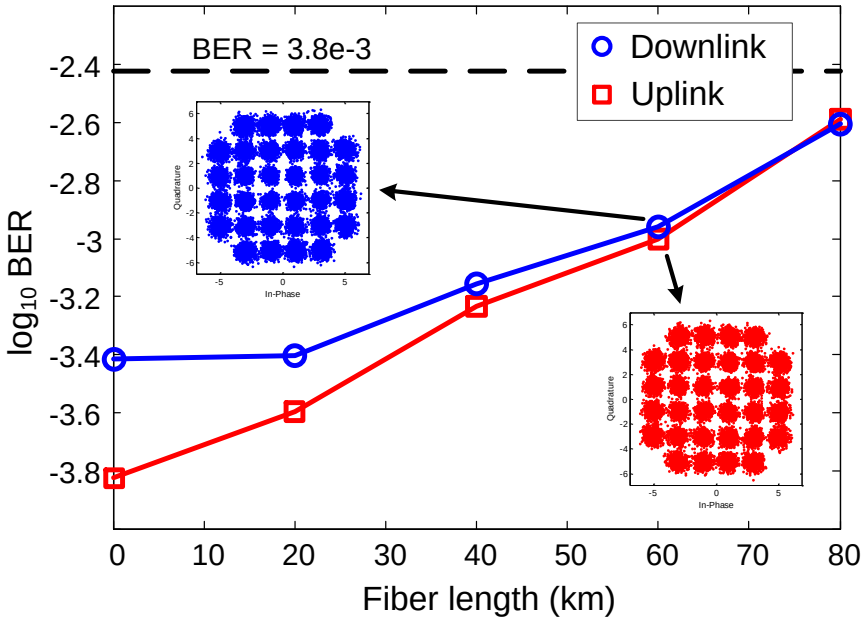

Figure 6.7: BER versus fiber length for 14.5 Gb/s bidirectional 32-QAM OFDMA-PON.

the fiber length the desired DL OFDM signal given by the first term of (6.11) decreases by a factor of L_{fiber}. As the UL and DL launched power is kept constant, the BS signal given by (6.13) decreases by a factor of $\sqrt{L_{fiber}}$. Therefore, the ratio between the desired DL signal and the BS decreases by increasing fiber length. Since we use direct detection at the DL receiver, BS still induces interference, although it is less severe in this case where the DL and UL do not share frequency bands [114]. In the UL, BS does not lead to performance degradation due to coherent detection as we discussed in section 6.3. However, as we extend the fiber length the input power to the optical modulator at the ONU decreases leading to OSNR loss for the UL signal.

6.6 Conclusion

We demonstrated a single-fiber lightwave centralized WDM-OFDMA-PON. Our proposed architecture uses DDO-OFDM for DL to minimize ONU implementation cost. We use CO-OFDM for UL to enable symmetric data transmission rates despite the signal quality degradation on the UL when using remodulation. We analyzed the impairments peculiar to the PON architecture and validated our discussions with simulations. We showed that RI can be detrimental for the UL and identified the necessary condition for preventing RI. This condition is respected in the second case. We minimized the RI by decreasing DL SCR in the first case where this condition is not respected. For the DL, BS is one of the main limiting factors in the first scenario where UL and DL signals overlap in frequency. BS has negligible

impact on the performance in the second scenario. Experiments show that BER below FEC threshold can be achieved for both DL and UL even in the worst case where the UL and DL signals completely overlap in frequency. This suggests the UL signal performance is not a bottleneck in the proposed PON architecture. We demonstrate 21.6 Gb/s bidirectional QPSK OFDMA-PON over 60 km of SMF. We show that system reach can be extended to 80 km for 14.5 Gb/s 32-QAM with different frequency bands for the DL and UL.

Subcarriers of OFDM are finely granular resources for bandwidth in optical networks. OFDM is resilient towards chromatic dispersion and its implementation can be potentially cheap by using silicon-based solutions. These benefits are the fundamental motivation for using OFDM in optical networks. Our proposed PON architecture introduces possibilities to make use of OFDM signal properties to reduce implementation cost of optical networks.

The algorithms introduced in previous chapters can be utilized in the proposed PON architecture to improve its performance. More specifically, since application of SOAs is preferred to EDFAs in PONs, DFBP nonlinearity compensation technique can play a critical role in increasing the link power budget and extending reach of the system. In addition, in realistic PON implementations where low-cost amplifiers and modulators are employed, predistortion technique can significantly improve the performance of OFDM-PON in the presence of nonlinearity.

Chapter 7

Conclusions and Future Work

Optical communication systems with advanced modulation formats using coherent detection and OFDM were the major subjects of this thesis. We studied several methods for improving performance of these systems. We were particularly interested in optical networks with reach below 100 km. The demonstrated methods in this thesis have effectively mitigated the problems and increased the data transmission rate. We also proposed and experimentally demonstrated a cost-efficient optical network architecture that uses a combination of modulation techniques studied in the thesis, i.e., direct detection, coherent detection and OFDM.

In chapter 2, we investigated performance of DFBP for compensating SOA nonlinearity in 16-QAM coherent detection system. Our experimental and numerical study showed that the simpler DFBP method leads to more effective nonlinearity compensation than RK4BP technique. By using DFBP method, we achieved over 5 dB higher launched power to the fiber. We also examined sensitivity of DFBP performance to the parameters used in "inverse SOA". Even with 10% variation of the parameters from their optimum values, negligible BER penalty is observed. The DFBP technique offers promising solution to performance degradation of integrated transmitters with SOAs in next-generation optical networks.

Chapter 3 proposed an efficient parameter estimation technique for DFBP. We investigated the performance of DFBP using coarse parameter estimation for suppressing SOA nonlinearity in 16-QAM coherent systems. We presented a simple, low overhead method based on EVM to coarsely estimate parameters of DFBP. The proposed scheme determines DFBP parameters by processing a small portion of data (4000 symbols). We showed that BER achieved with this method is in fact better than that achieved by DFBP with SOA characterization. We also found that a coarse-parameter DFBP has negligible penalty as compared to DFBP with fine parameter estimation. We investigated different bias currents for two commercial SOAs in our experiments to find optimum operating points and experimentally validated our method. We examined the OSNR penalty induced by application of SOA as booster at transmitter in transmission of signal over 80 km of SMF. The experimental results showed less than 4 dB

OSNR penalty at FEC threshold for both nonlinear and linear SOAs employed in our experiment. The proposed parameter estimation is independent of the employed SOA and facilitates implementation of DFBP in practical systems.

In chapter 4 we presented a comprehensive study of nonlinear distortions from an optical OFDM transmitter. We introduced parameters to quantify the nonlinear distortions from DAC, electrical PA and optical modulator. We showed that high IBO can solve the compression of OFDM signal at the transmitter; however, it incurs significant penalties in power efficiency. Our statistical analysis of PAPR in OFDM systems showed that combination of a PAPR reduction technique, e.g. clipping, with predistortion can lead to effective nonlinearity mitigation in a power efficient OFDM transmitter with high IBO. We proposed a predistortion method that uses training symbols to extract the transmitter nonlinear function. We showed that PLI leads to an accurate transmitter nonlinearity characterization. We derived a semi-analytical solution for BER that confirms the PLI approximation accurately captures transmitter nonlinearity. At the transmitter DSP, we used the inverse of the PLI estimate of the nonlinear function to suppress the nonlinearity. Our simulations showed when predistortion is used, BER below FEC threshold of 3.8×10^{-3} can be achieved with a 5-bit DAC, IBO equal to 2 dB and $\alpha_d = 1$ for optical modulator in 16-QAM CO-OFDM system. Clipping is the simplest PAPR reduction method and predistortion can be implemented via a lookup table with minimal hardware complexity.

In chapter 5, we experimentally demonstrated that performance of SP and DP direct-detection OFDM and DMT can be improved by using optimized M-QAM constellations. The obtained maximum data rate with BER less than FEC threshold is increased by 6 Gb/s for B2B and 4 Gb/s for 2.2 km span in DP DMT with optimized constellations compared to DMT with square QAM. We showed that optimized constellations increase data transmission rate by 3.6 Gb/s on average for OFDM and DMT systems. Application of irregular constellations does not incur extra complexity in the transmitter; it only requires application of a two-dimensional decision unit based on a look-up table, and modification of the decision boundaries at the receiver. .

In chapter 6, we proposed and experimentally demonstrated a single-fiber lightwave centralized WDM-OFDMA-PON. The proposed architecture uses DDO-OFDM for DL to minimize ONU implementation cost. We used CO-OFDM for UL to enable symmetric data transmission rates despite the signal quality degradation on the UL when using remodulation. We analyzed the impairments peculiar to the PON architecture and validated our discussions with Monte Carlo simulations. We showed that RI can be detrimental for the UL and identified the necessary condition for preventing RI. For the DL, BS is one of the main limiting factors. Our experiments show that BER below FEC threshold can be achieved for both DL and UL even in the worst case where the UL and DL signals completely overlap in frequency. This suggests the UL signal performance is not a bottleneck in the proposed PON architecture. We

demonstrate 21.6 Gb/s bidirectional QPSK OFDMA-PON over 60 km of SMF. We show that system reach can be extended to 80 km for 14.5 Gb/s 32-QAM with different frequency bands for the DL and UL.

There are several research opportunities to further the work presented in this thesis. Some of these possibilities are listed below:

- In our study on coherent detection systems with SOA, we considered 16-QAM as a popular modulation format for next-generation systems. Investigation of DFBP for higher order modulation formats, e.g., 64-QAM and higher, can be interesting due to high SE requirement of future optical communication systems.
- Our PON demonstration in chapter 6 used EDFAs for amplification due to limitations in the experimental equipment. In practice, SOAs are preferred due to their cost-effectiveness and integrability. Experimental demonstration of the proposed PON with SOAs and using DFBP for compensation of SOA-induced nonlinearities would highlight both DFBP effectiveness and the PON architecture.
- We focused on short/medium reach applications in this thesis. Therefore, fiber nonlinearity was neglected in our OFDM transmitter nonlinearity study. Including the impact of fiber nonlinearity in both theoretical analysis and simulations can extend the research to long-haul optical OFDM systems.
- We separated constellation optimization and bit-to-symbol mapping in chapter 5. A better optimization algorithm would perform both SER minimization and bit mapping at the same time, i.e., minimize BER rather than SER. Although this leads to more complexity in finding the constellations, the obtained constellations will offer lower BER. Another research opportunity would be extending the application of optimized constellations to medium and long-haul OFDM systems. In this case, new constellations should be found by taking into consideration the noise distribution in the system.
- The laser linewidth directly influences the noise distribution in the DDO-OFDM and DMT systems. Our experiments in chapter 5 used lasers with narrow linewidth (100 kHz). Performance of the optimized constellations for wide-linewidth lasers should be examined as a future work.

Appendix A

DFBP Parameter Variation

Fig. A.1(a) and Fig. A.1(b) show estimated carrier lifetime (τ_c) and P_{sat}, respectively, using coarse DFBP method for L-SOA and NL-SOA versus different SOA input powers. The parameters estimated by characterization of SOA in experiments (see Table 3.1) are also shown with dashed lines for comparison. We observe that for different SOA input powers, estimated parameters with coarse DFBP method change. This variation is more evident for estimated carrier lifetime. In SOA characterization method, the extracted parameters are constant for an SOA used in different nonlinear regimes. However, parameters leading to optimal performance in DFBP vary depending on the regime SOA is used in forward propagation.

The parameters measured by SOA characterization are for a specific SOA operating point which may be different from the operating point in coherent detection systems. Also, the accumulation of various effects in the channel, phase noise as an example, affects the parameters in DFBP which lead to minimum BER. Finally, measurement errors in SOA characterization can lead to inaccurate parameter estimation.

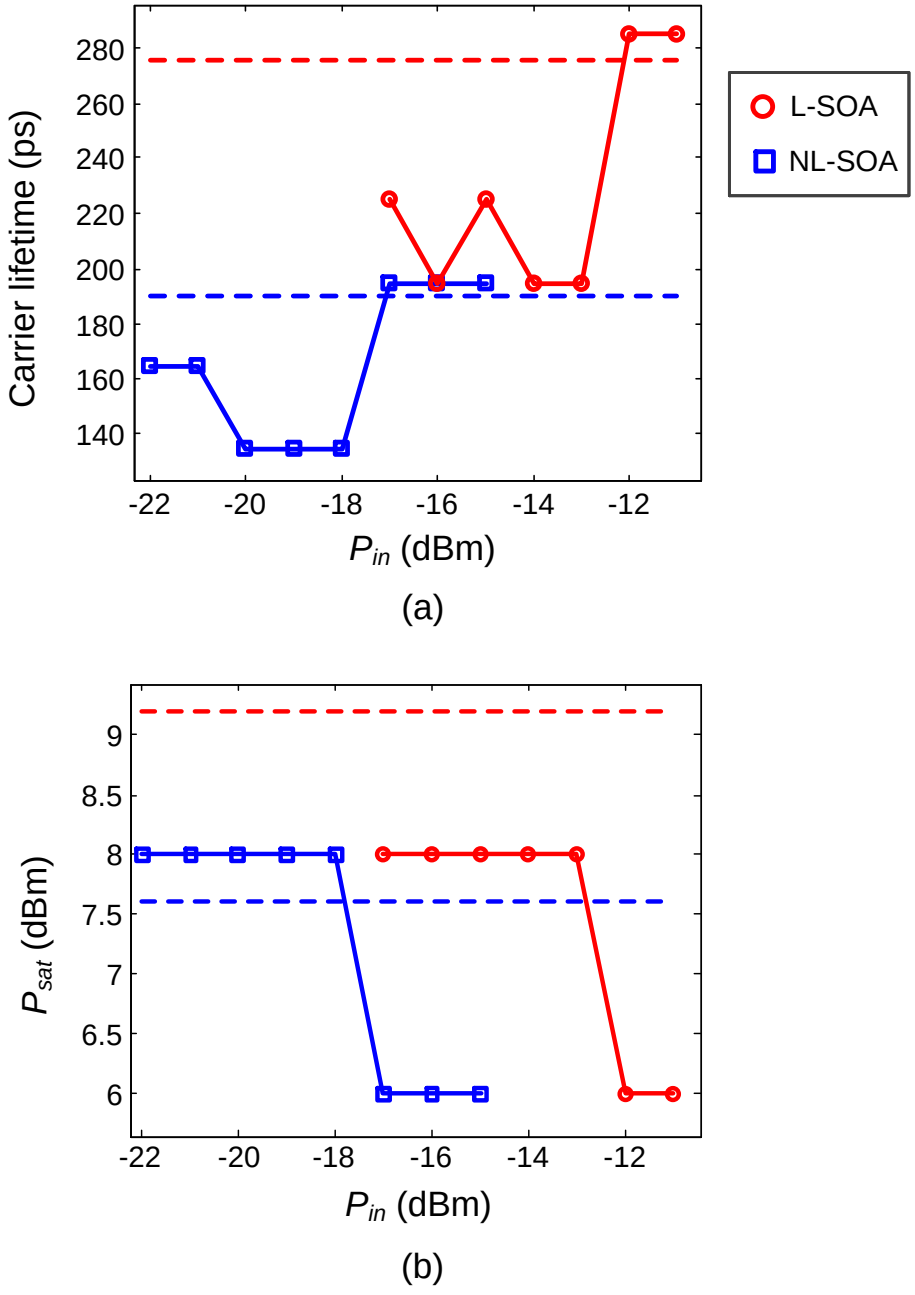

Figure A.1: Variation of estimated DFBP parameters for different SOA input powers. (a) Carrier lifetime, (b) SOA output saturation power. Solid line: coarse parameter estimation, dashed line: parameters extracted by SOA characterization. L-SOA and NL-SOA bias currents are 400 mA and 160 mA, respectively.

Appendix B

OFDM Receiver DSP

Block diagram of the OFDM receiver DSP is depicted in Fig. B.1. The captured data from RTO is first synchronized. A joint time and frequency synchronization can be implemented by using training symbols with two identical patterns in CO-OFDM [115]. We can also realize synchronization in time domain by identifying peaks in cross-correlation between the received samples and a known OFDM preamble. After synchronization, CP is removed from the OFDM signal. After the FFT block in DSP, we perform channel estimation and equalization. We estimate the channel across all subcarriers by using training symbols and comparing the received symbols with the transmitted ones in frequency domain. We then multiply the OFDM data symbols by inverse of the estimated channel response. The phase compensation step is highlighted since it is applied only in CO-OFDM. For phase estimation, we insert a few fixed pilot subcarriers in all OFDM symbols and estimate the phase by comparing the received and transmitted symbols. We then employ the estimated phase to compensate for the PN. Finally, we make decisions on the received symbols by assigning the reference symbol with smallest Euclidean distance to each received symbol and perform symbol-to-bit mapping.

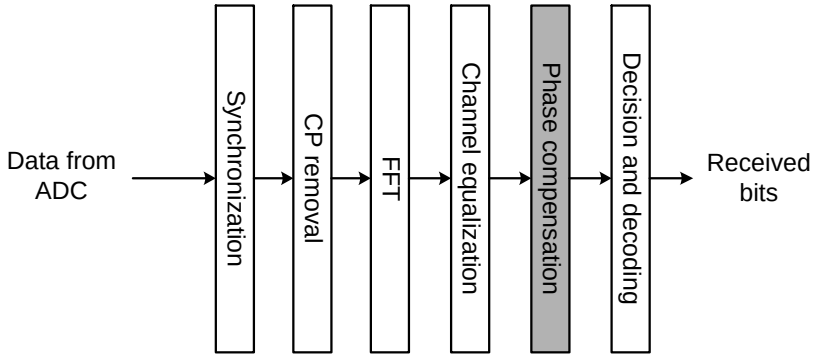

Figure B.1: Receiver DSP for CO-OFDM and DDO-OFDM. Phase noise compensation is done only for CO-OFDM.

Appendix C

Definition of $\psi_k(v, w)$

In this section, we introduce $\psi_k(v, w)$ function and present the required formula to calculate κ and σ_y^2 given in 4.17 and 4.18. $\psi_k(v, w)$ is defined as

$$\psi_k(v, w) = \frac{1}{\sqrt{2\pi\sigma_x^2}} \int_v^w x^k \exp(-\frac{x^2}{2\sigma_x^2}) \mathrm{d}x. \tag{C.1}$$

For $k = 0, 1$ and 2, $\psi_k(v, w)$ is given by

$$\psi_0(v, w) = \mathrm{Q}\left(\frac{v}{\sigma_x}\right) - \mathrm{Q}\left(\frac{w}{\sigma_x}\right), \tag{C.2}$$

$$\psi_1(v, w) = \frac{\sigma_x}{\sqrt{2\pi}} \left[\exp\left(-\frac{v^2}{2\sigma_x^2}\right) - \exp\left(-\frac{w^2}{2\sigma_x^2}\right)\right], \tag{C.3}$$

$$\psi_2(v, w) = \sigma_x^2 \psi_0(v, w) + \frac{\sigma_x}{\sqrt{2\pi}} \left[v \exp\left(-\frac{v^2}{2\sigma_x^2}\right) - w \exp\left(-\frac{w^2}{2\sigma_x^2}\right)\right], \tag{C.4}$$

where $\mathrm{Q}(x)$ is the tail probability of the standard normal distribution.

Appendix D

Coordinates of QAM Constellations

Table D.1: Coordinates of the symbols on the I/Q plane for optimized 8-QAM constellations

Bit mapping (decimal)	$\mathrm{QAM_{SQ}}$	$\mathrm{QAM_{w/o\,PR}}$	$\mathrm{QAM_{with\,PR}}$
0	$-1.2247 + 0.4082i$	1.3667	$-0.0008 - 0.8600i$
1	$-1.2247 - 0.4082i$	$-0.2208 - 1.0243i$	0.4074
2	$-0.4082 + 0.4082i$	$0.6018 + 0.5560i$	$-1.0802 - 0.6158i$
3	$-0.4082 - 0.4082i$	$0.6024 - 0.5569i$	$-0.4071 + 0.0010i$
4	$0.4082 + 0.4082i$	$-1.0229 + 0.4845i$	$1.0790 - 0.6184i$
5	$0.4082 - 0.4082i$	$-1.0221 - 0.4877i$	$1.0808 + 0.6158i$
6	$1.2247 + 0.4082i$	$-0.2222 + 1.0222i$	$-1.0790 + 0.6182i$
7	$1.2247 - 0.4082i$	$-0.1782 - 0.0009i$	$0.0011 + 0.8613i$

Table D.2: Coordinates of the symbols on the I/Q plane for optimized 16-QAM constellations

Bit mapping (decimal)	$\mathrm{QAM_{SQ}}$	$\mathrm{QAM_{w/o\,PR}}$	$\mathrm{QAM_{with\,PR}}$
0	$-0.9487 + 0.9487i$	$-0.2466 + 0.7182i$	$1.2343 + 0.4002i$
1	$-0.9487 + 0.3162i$	$0.0816 + 0.1399i$	$0.0008 + 1.2975i$
2	$-0.9487 - 0.3162i$	$-0.2575 - 0.4420i$	$0.6325 + 0.8695i$
3	$-0.9487 - 0.9487i$	$0.4109 - 0.4377i$	$0.0004 + 0.6001i$
4	$-0.3162 + 0.9487i$	$0.0641 + 1.3104i$	$1.0225 - 0.3329i$
5	$-0.3162 + 0.3162i$	$0.4262 + 0.7314i$	$0.3524 - 0.4857i$
6	$-0.3162 - 0.3162i$	$-0.6045 - 1.0374i$	$0.5709 + 0.1851i$
7	$-0.3162 - 0.9487i$	$0.0781 - 1.0406i$	0
8	$0.3162 + 0.9487i$	$-0.9078 + 0.7732i$	$-1.2338 + 0.4018i$
9	$0.3162 + 0.3162i$	$0.7465 + 0.1396i$	$-0.6315 + 0.8703i$
10	$0.3162 - 0.3162i$	$-0.5834 + 0.1416i$	$-1.0228 - 0.3316i$
11	$0.3162 - 0.9487i$	$1.1203 - 0.4086i$	$-0.5706 + 0.1858i$
12	$0.9487 + 0.9487i$	$-1.2570 + 0.1666i$	$0.7620 - 1.0502i$
13	$0.9487 + 0.3162i$	$1.1084 + 0.7019i$	$-0.0007 - 1.0753i$
14	$0.9487 - 0.3162i$	$-0.9438 - 0.4451i$	$-0.7634 - 1.0493i$
15	$0.9487 - 0.9487i$	$0.7647 - 1.0115i$	$-0.3531 - 0.4853i$

Table D.3: Coordinates of the symbols on the I/Q plane for optimized 32-QAM constellations

Bit mapping (decimal)	$\mathrm{QAM_{SQ}}$	$\mathrm{QAM_{w/o\,PR}}$	$\mathrm{QAM_{with\,PR}}$
0	$-0.6708 + 1.1180i$	$0.4922 + 0.8581i$	$-0.1344 - 1.3808i$
1	$-0.2236 + 1.1180i$	$0.9703 + 0.8735i$	$0.8080 - 0.7980i$
2	$-0.2236 - 1.1180i$	$0.7304 + 0.4463i$	$0.2680 - 0.9424i$
3	$-0.6708 - 1.1180i$	$1.2221 + 0.4428i$	$0.4900 - 0.4951i$
4	$-1.1180 + 0.6708i$	$-0.6839 - 1.1921i$	$0.7980 + 0.8080i$
5	$-1.1180 + 0.2236i$	$-0.9286 + 0.0380i$	$1.3808 - 0.1344i$
6	$-1.1180 - 0.2236i$	$-0.9396 - 0.7742i$	$0.5083 - 1.3080i$
7	$-1.1180 - 0.6708i$	$-1.1930 - 0.3557i$	$0.9340 - 0.2715i$
8	$-0.6708 + 0.6708i$	$0.2641 + 1.2785i$	$-0.2715 - 0.9340i$
9	$-0.6708 + 0.2236i$	$1.2247 - 0.3712i$	$1.3080 + 0.5083i$
10	$-0.6708 - 0.2236i$	$0.4931 + 0.0373i$	$-0.0003 - 0.5838i$
11	$-0.6708 - 0.6708i$	$0.9722 + 0.0363i$	$0.2053 - 0.2053i$
12	$-0.2236 + 0.6708i$	$0.5016 - 0.7824i$	$0.4951 + 0.4900i$
13	$-0.2236 + 0.2236i$	$0.9778 - 0.8043i$	$0.9424 + 0.2680i$
14	$-0.2236 - 0.2236i$	$0.2600 - 0.3685i$	$0.2053 + 0.2053i$
15	$-0.2236 - 0.6708i$	$0.7349 - 0.3729i$	$0.5838 - 0.0003i$
16	$0.2236 + 0.6708i$	$0.0165 + 0.8558i$	$-1.3808 + 0.1344i$
17	$0.2236 + 0.2236i$	$-0.6928 + 0.4461i$	$-0.9340 + 0.2715i$
18	$0.2236 - 0.2236i$	$0.2549 + 0.4444i$	$-0.9424 - 0.2680i$
19	$0.2236 - 0.6708i$	$-0.4493 + 0.0384i$	$-0.5838 + 0.0003i$
20	$0.6708 + 0.6708i$	$-0.1940 - 1.2019i$	$0.1344 + 1.3808i$
21	$0.6708 + 0.2236i$	$-1.1879 + 0.4380i$	$-0.8080 + 0.7980i$
22	$0.6708 - 0.2236i$	$-0.4448 - 0.7755i$	$-1.3080 - 0.5083i$
23	$0.6708 - 0.6708i$	$-0.6878 - 0.3677i$	$-0.4900 + 0.4951i$
24	$1.1180 + 0.6708i$	$-0.2348 + 1.2785i$	$-0.7980 - 0.8080i$
25	$1.1180 + 0.2236i$	$-0.4595 + 0.8575i$	$-0.5083 + 1.3080i$
26	$1.1180 - 0.2236i$	$0.0220 + 0.0383i$	$-0.4951 - 0.4900i$
27	$1.1180 - 0.6708i$	$-0.2167 + 0.4445i$	$-0.2053 - 0.2053i$
28	$0.6708 + 1.1180i$	$0.2952 - 1.2094i$	$0.2715 + 0.9340i$
29	$0.2236 + 1.1180i$	$-0.9388 + 0.8698i$	$-0.2680 + 0.9424i$
30	$0.2236 - 1.1180i$	$0.0298 - 0.7793i$	$0.0003 + 0.5838i$
31	$0.6708 - 1.1180i$	$-0.2106 - 0.3671i$	$-0.2053 + 0.2053i$

Table D.4: Coordinates of the symbols on the I/Q plane for optimized 64-QAM constellations

Bit mapping (decimal)	$\mathrm{QAM_{SQ}}$	$\mathrm{QAM_{w/o\,PR}}$	$\mathrm{QAM_{with\,PR}}$
0	$-1.0801 + 1.0801i$	$-0.2074 - 0.9987i$	$-0.8704 + 0.3903i$
1	$-1.0801 + 0.7715i$	$0.1358 - 0.4228i$	$-1.1263 + 0.5962i$
2	$-1.0801 + 0.4629i$	$-0.3692 - 0.7039i$	$1.1265 + 0.5960i$
3	$-1.0801 + 0.1543i$	$-0.0346 - 0.7083i$	$0.8706 + 0.3901i$
4	$-1.0801 - 0.1543i$	$-0.1869 + 0.1521i$	$-0.3418 - 0.3416i$
5	$-1.0801 - 0.4629i$	$0.1426 + 0.1485i$	$-0.1996 + 1.1802i$
6	$-1.0801 - 0.7715i$	$-0.6751 + 1.0424i$	$-0.5471 - 0.5471i$
7	$-1.0801 - 1.0801i$	$-0.8489 + 0.7336i$	$0.0002 + 1.4937i$
8	$-0.7715 + 1.0801i$	$-0.5463 - 0.9947i$	$-0.6332 + 0.1935i$
9	$-0.7715 + 0.7715i$	$-1.2296 + 0.1637i$	$-0.9032 + 0.0001i$
10	$-0.7715 + 0.4629i$	$-0.7093 - 0.7001i$	$-0.9873 + 0.9875i$
11	$-0.7715 + 0.1543i$	$-1.0592 - 0.6970i$	$0.6332 + 0.1933i$
12	$-0.7715 - 0.1543i$	$-0.0183 + 0.4370i$	$-0.1423 - 0.1423i$
13	$-0.7715 - 0.4629i$	$-1.0257 + 0.4398i$	$-1.1801 + 0.1999i$
14	$-0.7715 - 0.7715i$	$-1.0202 + 1.0304i$	$-0.1935 - 0.6332i$
15	$-0.7715 - 1.0801i$	$-1.2071 + 0.7234i$	$0.4029 - 0.0001i$
16	$-0.4629 + 1.0801i$	$-0.3570 - 0.1316i$	$1.4937 - 0.0002i$
17	$-0.4629 + 0.7715i$	$-0.0260 - 0.1351i$	$1.1802 + 0.1996i$
18	$-0.4629 + 0.4629i$	$-0.5308 - 0.4149i$	$0.1996 - 1.1802i$
19	$-0.4629 + 0.1543i$	$-0.1962 - 0.4186i$	$-0.0002 - 1.4937i$
20	$-0.4629 - 0.1543i$	$-0.5180 + 0.1552i$	$1.1263 - 0.5962i$
21	$-0.4629 - 0.4629i$	$-0.6817 + 0.4431i$	$0.0001 + 0.9032i$
22	$-0.4629 - 0.7715i$	$-0.5123 + 0.7334i$	$-0.7612 - 0.7610i$
23	$-0.4629 - 1.0801i$	$-0.3412 + 1.0252i$	$0.1999 + 1.1801i$
24	$-0.1543 + 1.0801i$	$-0.6919 - 0.1279i$	$1.1801 - 0.1999i$
25	$-0.1543 + 0.7715i$	$-1.0388 - 0.1174i$	$0.9032 - 0.0001i$
26	$-0.1543 + 0.4629i$	$-0.8733 - 0.4086i$	$-0.0001 - 0.9032i$
27	$-0.1543 + 0.1543i$	$-1.2345 - 0.3935i$	$-0.1999 - 1.1801i$
28	$-0.1543 - 0.1543i$	$-0.3485 + 0.4408i$	$0.8704 - 0.3903i$
29	$-0.1543 - 0.4629i$	$-0.8550 + 0.1581i$	$0.6332 - 0.1935i$
30	$-0.1543 - 0.7715i$	$-0.1790 + 0.7284i$	$-0.3903 - 0.8704i$
31	$-0.1543 - 1.0801i$	$-0.1825 + 1.3268i$	$-0.5962 - 1.1263i$
32	$0.1543 + 1.0801i$	$-0.0425 - 1.3031i$	$-0.4029 + 0.0001i$
33	$0.1543 + 0.7715i$	$0.4690 - 0.4286i$	$-0.6332 - 0.1933i$
34	$0.1543 + 0.4629i$	$0.3077 - 1.3112i$	$0.5960 - 1.1265i$

35	$0.1543 + 0.1543i$	$0.1292 - 1.0038i$	$0.9873 - 0.9875i$
36	$0.1543 - 0.1543i$	$0.6418 + 0.4341i$	$-0.3901 + 0.8706i$
37	$0.1543 + 0.4629i$	$0.3047 - 0.1393i$	$-0.1933 + 0.6332i$
38	$0.1543 - 0.7715i$	$0.4818 + 0.7260i$	$-0.5960 + 1.1265i$
39	$0.1543 - 1.0801i$	$-0.3317 + 1.0223i$	$0.0001 + 0.4029i$
40	$0.4629 + 1.0801i$	$-0.3930 - 1.2988i$	$-0.5471 + 0.5471i$
41	$0.4629 + 0.7715i$	$0.2994 - 0.7135i$	$-1.1802 - 0.1996i$
42	$0.4629 + 0.4629i$	$-0.8885 - 1.0025i$	$-0.7610 + 0.7612i$
43	$0.4629 + 0.1543i$	$0.4663 - 1.0110i$	$0.3418 + 0.3416i$
44	$0.4629 - 0.1543i$	$0.3109 + 0.4344i$	$-0.3416 + 0.3418i$
45	$0.4629 - 0.4629i$	$0.4728 + 0.1454i$	$-1.4937 + 0.0002i$
46	$0.4629 - 0.7715i$	$0.1515 + 0.7261i$	$-0.1423 + 0.1423i$
47	$0.4629 - 1.0801i$	$0.1759 + 1.3249i$	$0.1423 + 0.1423i$
48	$0.7715 + 1.0801i$	$0.9756 - 0.1488i$	$0.9875 + 0.9873i$
49	$0.7715 + 0.7715i$	$0.6375 - 0.1439i$	$0.7612 + 0.7610i$
50	$0.7715 + 0.4629i$	$1.1542 - 0.4454i$	$0.3901 - 0.8706i$
51	$0.7715 + 0.1543i$	$0.8065 - 0.4365i$	$0.7610 - 0.7612i$
52	$0.7715 - 0.1543i$	$0.9766 + 0.4381i$	$0.3903 + 0.8704i$
53	$0.7715 - 0.4629i$	$0.8060 + 0.1435i$	$0.1935 + 0.6332i$
54	$0.7715 - 0.7715i$	$0.8121 + 0.7349i$	$-0.9875 - 0.9873i$
55	$0.7715 - 1.0801i$	$0.6717 + 1.0466i$	$0.5471 - 0.5471i$
56	$1.0801 + 1.0801i$	$1.3291 - 0.1463i$	$-1.1265 - 0.5960i$
57	$1.0801 + 0.7715i$	$0.6369 - 0.7229i$	$-0.8706 - 0.3901i$
58	$1.0801 + 0.4629i$	$0.9810 - 0.7397i$	$0.1933 - 0.6332i$
59	$1.0801 + 0.1543i$	$0.8056 - 1.0384i$	$0.5471 + 0.5471i$
60	$1.0801 - 0.1543i$	$1.3240 + 0.4350i$	$0.5962 + 1.1263i$
61	$1.0801 - 0.4629i$	$1.1460 + 0.1426i$	$0.1423 - 0.1423i$
62	$1.0801 - 0.7715i$	$1.1501 + 0.7482i$	$-0.0001 - 0.4029i$
63	$1.0801 - 1.0801i$	$-0.0056 + 1.0228i$	$0.3416 - 0.3418i$

Appendix E

DP DMT Performance Sensitivity to OBPF Center Frequency Offset

Cost-efficient implementation of short-reach optical communication systems is of great importance. In order to reduce the cost, inexpensive devices are usually preferred in these systems. The deployed DP DMT scheme requires application of an OBPF at each receiver. Instability of center frequency or bandwidth of the employed filter can induce significant crosstalk between the two polarizations or lead to attenuation of the received signal.

Fig. E.1 shows measured BER of Y polarization versus center frequency offset of the OBPF at DP DMT receiver. The experimental results show that BER penalty is less than 0.3 dB when displacement of the OBPF center frequency is below 6.5 GHz. The tolerance to center frequency offset is much higher compared to the SSB DDO-OFDM [86]. Robustness of the signal in our experiments is due to the DSB transmission; while one sideband of the signal is affected from filter center frequency detuning, the other sideband is not disturbed. We also notice that BER degradation is less when center frequency is shifted towards left as opposed to right. When filter is shifted toward left, the performance degradation is due to power attenuation of one sideband of the signal. However, crosstalk from X polarization increases BER when filter center frequency is shifted to right.

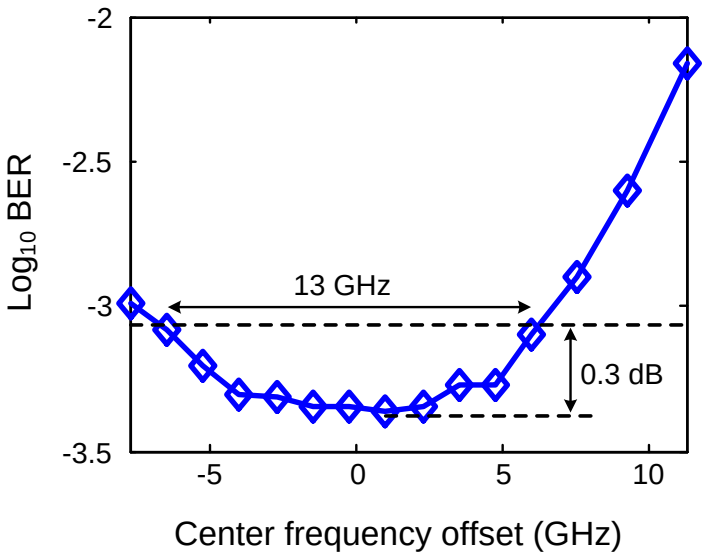

Figure E.1: BER versus OBPF center frequency offset in 75 Gb/s per polarization DP DMT with optimized QAM constellations and 2.2 km transmission.

Publication List

During my PhD, I had the privilege of contributing to the following research works, some of which were presented in detail in this thesis:

1. S. Amiralizadeh, A. Yekani, and L. A. Rusch, "Discrete multi-tone transmission with optimized QAM constellations for short-reach optical communications", Accepted for publication in *IEEE Journal of Lightwave Technology*, 2016.

2. R. Mirzaei Nejad, K. Allahverdyan, P. Vaity, S. Amiralizadeh, C. Brunet, Y. Messaddeq, S. LaRochelle, and L. A. Rusch, "Mode Division Multiplexing using Orbital Angular Momentum Modes over 1.4 km Ring Core Fiber", Accepted for publication in *IEEE Journal of Lightwave Technology*, 2016.

3. S. Amiralizadeh, A. T. Nguyen, C. S. Park, and L. A. Rusch, "Single-fiber lightwave centralized WDM-OFDMA-PON with colorless optical network units", *Journal of Optical Communications and Networking*, vol. 8, no. 4, pp. 196–205, Apr. 2016.

4. A. Yekani, S. Amiralizadeh, and L. A. Rusch, "Comparison of 100 Gb/s O-band PAM-4 vs. C-band DMT for different laser linewidths and fiber lengths", *Conference on Lasers and Electro-Optics*, 2016.

5. R. Mirzaei Nejad, K. Allahverdyan, P. Vaity, S. Amiralizadeh, C. Brunet, Y. Messaddeq, S. LaRochelle and L. A. Rusch, "Orbital angular momentum mode division multiplexing over 1.4 km RCF fiber", *Conference on Lasers and Electro-Optics*, 2016.

6. S. Amiralizadeh, A. T. Nguyen, and L. A. Rusch, "Modeling and compensation of transmitter nonlinearity in coherent optical OFDM", *Optics Express*, vol. 23, no. 20, pp. 26192–26207, 2015.

7. S. Amiralizadeh, C. S. Park, and L. A. Rusch, "Experimental study of M-QAM constellation options for short-reach dual-polarization optical OFDM with direct detection", *European Conference on Optical Communication*, 2015, paper p.4.6.

8. S. Amiralizadeh and L. A. Rusch, "Transmitter sensitivity to high PAPR in coherent optical OFDM systems", *Conference on Lasers and Electro-Optics*, 2014, paper SW1J.5.

9. S. Amiralizadeh, A. T. Nguyen, and L. A. Rusch, "Error vector magnitude based parameter estimation for digital filter back-propagation mitigating SOA distortions in 16-QAM", *Optics Express*, vol. 21, no. 17, pp. 20376–20386, 2013.

10. S. Amiralizadeh, A. T. Nguyen, C. S. Park, A. Ghazisaeidi, and L. A. Rusch, "Experimental validation of digital filter back-propagation to suppress SOA-induced nonlinearities in 16-QAM", *Optical Fiber Communication Conference*, 2013, paper OM2B.2.

11. B. Filion, S. Amiralizadeh, A. T. Nguyen, L. A. Rusch and S. LaRochelle, "Wideband wavelength conversion of 16 Gbaud 16-QAM signals in a semiconductor optical amplifier", *Optical Fiber Communication Conference*, 2013, paper OTh1C.5.

Bibliography

[1] S. Amiralizadeh, A. T. Nguyen, C. S. Park, A. Ghazisaeidi, and L. A. Rusch. Experimental validation of digital filter back-propagation to suppress SOA-induced nonlinearities in 16-QAM. *Optical Fiber Communication Conference*, paper OM2B.2, 2013.

[2] S. Amiralizadeh, A. T. Nguyen, and L. A. Rusch. Error vector magnitude based parameter estimation for digital filter back-propagation mitigating SOA distortions in 16-QAM. *Opt. Express*, vol. 21, no. 17, pp. 20376–20386, 2013.

[3] S. Amiralizadeh and L. A. Rusch. Transmitter sensitivity to high PAPR in coherent optical OFDM systems. *CLEO: Science and Innovations*, paper SW1J.5, 2014.

[4] S. Amiralizadeh, A. T. Nguyen, and L. A. Rusch. Modeling and compensation of transmitter nonlinearity in coherent optical OFDM. *Opt. Express*, vol. 23, no. 20, pp. 26192–26207, 2015.

[5] S. Amiralizadeh, C. Park, and L. A. Rusch. Experimental study of M-QAM constellation options for short-reach dual-polarization optical OFDM with direct detection. *European Conference and Exhibition on Optical Communication*, paper p.4.6, 2015.

[6] S. Amiralizadeh, A. Yekani, and L. A. Rusch. Discrete multi-tone transmission with optimized QAM constellations for short-reach optical communications. *J. Lightwave Technol.*, submitted for publication.

[7] S. Amiralizadeh, A. T. Nguyen, C. S. Park, and L. A. Rusch. Single-fiber lightwave centralized WDM-OFDMA-PON with colorless optical network units. *J. Opt. Commun. Netw.*, submitted for publication.

[8] Cisco VNI: Forecast and Methodology, 2014–2019. *Cisco Public Information*, May, 2015.

[9] R. Essiambre and R. W. Tkach. Capacity trends and limits of optical communication networks. *in Proceedings of the IEEE*, vol. 100, no. 5, pp. 1035–1055, 2012.

[10] D. Qian, M.-F. Huang, E. Ip, Y.-K. Huang, Y. Shao, J. Hu, and T. Wang. High capacity/spectral efficiency 101.7-Tb/s WDM transmission using PDM-128QAM-OFDM

over 165-km SSMF within C- and L-bands. *J. Lightwave Technol.*, vol. 30, no. 10, pp. 1540–1548, 2012.

[11] C. R. Doerr. High performance photonic integrated circuits for coherent fiber communication. *Optical Fiber Communication Conference*, paper OWU5, 2010.

[12] G. Contestabile, Y. Yoshida, A. Maruta, and K. Kitayama. 100 nm-bandwidth positive-efficiency wavelength conversion for m-PSK and m-QAM signals in QD-SOA. *Optical Fiber Communication Conference*, paper OTh1C.6, 2013.

[13] B. Filion, S. Amiralizadeh, A. T. Nguyen, L. A. Rusch, and S. LaRochelle. Wideband wavelength conversion of 16 Gbaud 16-QAM signals in a semiconductor optical amplifier. *Optical Fiber Communication Conference*, paper OTh1C.5, 2013.

[14] A. Ghazisaeidi, F. Vacondio, A. Bononi, and L. A. Rusch. SOA intensity noise suppression: A Multicanonical Monte Carlo simulator of extremely low BER. *J. Lightwave Technol.*, vol. 27, no. 14, pp. 2667–2677, 2009.

[15] C. Porzi, A. Bogoni, and G. Contestabile. Regeneration of DPSK signals in a saturated SOA. *IEEE Photon. Technol. Lett.*, vol. 24, no. 18, pp. 1597–1599, 2012.

[16] P. Leclerc, B. Lavigne, E. Balmefrezol, P. Brindel, L. Pierre, D. Rouvillain, and F. Seguineau. Optical regeneration at 40 Gb/s and beyond. *J. Lightwave Technol.*, vol. 21, no. 11, pp. 2779–2790, 2003.

[17] Z. Li, Y. Dong, J. Mo, Y. Wang, and C. Lu. 1050-km WDM transmission of 8×10.709 Gb/s DPSK signal using cascaded in-line semiconductor optical amplifiers. *IEEE Photon. Technol. Lett.*, vol. 16, no. 7, pp. 1760–1762, 2004.

[18] P. Cho, Y. Achiam, G. Levy-Yurista, M. Margalit, Y. Gross, and J. Khurgin. Investigation of SOA nonlinearities on the amplification of DWDM channels with spectral efficiency up to 2.5 b/s/Hz. *IEEE Photon. Technol. Lett.*, vol. 16, no. 3, pp. 918–920, 2004.

[19] X. Wei, Y. Su, X. Liu, J. Leuthold, and S. Chandrasekhar. 10-Gb/s RZ-DPSK transmitter using a saturated SOA as a power booster and limiting amplifier. *IEEE Photon. Technol. Lett.*, vol. 16, no. 6, pp. 1582–1584, 2004.

[20] A. Ciaramella, E.and D'Errico and V. Donzella. Using semiconductor-optical amplifiers with constant envelope WDM signals. *IEEE J. Quantum Electron.*, vol. 44, no. 5, pp. 403–409, 2008.

[21] L. H. Spiekman, J. M. Wiesenfeld, A. H. Gnauck, L. D. Garrett, G. N. Van den Hoven, T. Van Dongen, M. J. H. Sander-Jochem, and J. J. M. Binsma. Transmission of 8 DWDM

channels at 20 Gb/s over 160 km of standard fiber using a cascade of semiconductor optical amplifiers. *IEEE Photon. Technol. Lett.*, vol. 12, no. 6, pp. 717–719, 2000.

[22] D. Zimmerman and L. Spiekman. Amplifiers for the masses: EDFA, EDWA, and SOA amplets for metro and access applications. *J. Lightwave Technol.*, vol. 22, no. 1, pp. 63–70, 2004.

[23] T. Yasui, Y. Shibata, K. Tsuzuki, N. Kikuchi, Y. Kawaguchi, M. Arai, and H. Yasaka. Lossless 10-Gbit/s InP n-p-i-n Mach-Zehnder modulator monolithically integrated with semiconductor optical amplifier. *Optical Fiber Communication Conference*, paper OThC5, 2008.

[24] A. Nakanishi, N. Sasada, Y. Sakuma, R. Washino, K. Okamoto, H. Hayashi, H. Arimoto, and S. Tanaka. Uncooled (0 to 85°C) and full C-band operation of a 10.7 Gbit/s InP Mach-Zehnder modulator monolithically integrated with SOA. *Optical Fiber Communication Conference*, paper OW1G.3, 2013.

[25] R. A. Griffin, N. D. Whitbread, S. Jones, S. C. Heck, P. Firth, D. Govan, and T. Goodall. InP coherent optical modulator with integrated amplification for high capacity transmission. *Optical Fiber Communication Conference*, paper Th4E.2, 2015.

[26] N. Kamitani, Y. Yoshida, and K. Kitayama. Experimental study on impact of SOA nonlinear phase noise in 40Gbps coherent 16QAM transmissions. *European Conference and Exhibition on Optical Communication*, paper P1.04, 2012.

[27] A. Ghazisaeidi and L. A. Rusch. On the efficiency of digital back-propagation for mitigating SOA-induced nonlinear impairments. *J. Lightwave Technol.*, vol. 29, no. 21, pp. 3331–3339, 2011.

[28] F. Vacondio, A. Ghazisaeidi, A. Bononi, and L. A. Rusch. Low-complexity compensation of SOA nonlinearity for single-channel PSK and OOK. *J. Lightwave Technol.*, vol. 28, no. 3, pp. 277–288, 2010.

[29] X. Li and G. Li. Electrical postcompensation of SOA impairments for fiber-optic transmission. *IEEE Photon. Technol. Lett.*, vol. 21, no. 9, pp. 581–583, 2009.

[30] X. Li and G. Li. Joint fiber and SOA compensation using digital backward propagation. *IEEE Photon. J.*, vol. 2, no. 5, pp. 753–758, 2010.

[31] S. Lange, Y. Yoshida, and K. Kitayama. A low-complexity digital pre-compensation of SOA induced phase distortion in coherent QAM transmissions. *Optical Fiber Communication Conference*, paper OTh3C.7, 2013.

[32] D. Cassioli, S. Scotti, and A. Mecozzi. A time-domain computer simulator of the nonlinear response of semiconductor optical amplifiers. *IEEE J. Quantum Electron.*, vol. 36, no. 9, pp. 1072–1080, 2000.

[33] M. Selmi, Y. Jaouen, and P. Cibalt. Accurate digital frequency estimator for coherent PolMux QAM transmission systems. *European Conference and Exhibition on Optical Communication*, paper P3.08, 2009.

[34] S. Zhang, C. Yu, P. Y. Kam, and J. Chen. Parallel implementation of decision-aided maximum likelihood phase estimation in coherent M-ary phase-shifted keying systems. *IEEE Photon. Technol. Lett.*, vol. 21, no. 19, pp. 1471–1473, 2009.

[35] B. Filion, A. Ghazisaeidi, L. A. Rusch, and S. LaRochelle. Extraction of semiconductor optical amplifier parameters for wavelength conversion modeling. *IEEE Photonics Conference*, pp. 367–368, 2011.

[36] A. Saleh. Nonlinear models of travelling-wave optical amplifiers. *Electron. Lett.*, vol. 24, no. 14, pp. 835–837, 1988.

[37] R. Schmogrow, B. Nebendahl, M. Winter, A. Josten, D. Hillerkuss, S. Koenig, J. Meyer, M. Dreschmann, M. Huebner, C. Koos, J. Becker, W. Freude, and J. Leuthold. Error vector magnitude as a performance measure for advanced modulation formats. *IEEE Photon. Technol. Lett.*, vol. 24, no. 1, pp. 61–63, 2012.

[38] H. Sari, G. Karam, and I. Jeanclaude. Transmission techniques for digital terrestrial TV broadcasting. *IEEE Commun. Mag.*, vol. 33, no. 2, pp. 100–109, 1995.

[39] I. Koffman and V. Roman. Broadband wireless access solutions based on OFDM access in IEEE 802.16. *IEEE Commun. Mag.*, vol. 40, no. 4, pp. 96–103, 2002.

[40] R. Prasad. *OFDM for wireless communications systems.* Artech House, 2004.

[41] A. J. Lowery, L. Du, and J. Armstrong. Orthogonal frequency division multiplexing for adaptive dispersion compensation in long haul WDM systems. *Optical Fiber Communication Conference*, paper PDP39, 2006.

[42] W. Shieh, H. Bao, and Y. Tang. Coherent optical OFDM: theory and design. *Opt. Express*, vol. 16, no. 2, pp. 841–859, 2008.

[43] S. L. Jansen, I. Morita, T. C. W. Schenk, N. Takeda, and H. Tanaka. Coherent optical 25.8-Gb/s OFDM transmission over 4160-km SSMF. *J. Lightwave Technol.*, vol. 26, no. 1, pp. 6–15, 2008.

[44] Q. Zhuge, M. H. Morsy-Osman, and D. V. Plant. Low overhead intra-symbol carrier phase recovery for reduced-guard-interval CO-OFDM. *J. Lightwave Technol.*, vol. 31, no. 8, pp. 1158–1169, 2013.

[45] S. Chandrasekhar, X. Liu, P. J. Winzer, T. Lotz, C. J. Youn, Y. H. Kwon, and E. S. Nam. Field demonstration of 3×341-Gb/s PDM-OFDM-256 iterative polar modulation signals with a record 11.0-b/s/Hz intrachannel spectral efficiency. *Optical Fiber Communication Conference*, paper Th5A.8, 2014.

[46] C. Guo, J. Liang, J. Liu, and L. Liu. Extended reach OFDM-PON using super-Nyquist image induced aliasing. *Opt. Express*, vol. 23, no. 17, pp. 21798–21808, 2015.

[47] Y. Chen, A. Lobato, Y. Jung, H. Chen, V. A. J. M. Sleiffer, M. Kuschnerov, N. K. Fontaine, R. Ryf, D. J. Richardson, B. Lankl, and N. Hanik. 41.6 Tbit/s C-Band SDM OFDM transmission through 12 spatial and polarization modes over 74.17 km few mode fiber. *J. Lightwave Technol.*, vol. 33, no. 7, pp. 1440–1444, 2015.

[48] J. Armstrong. OFDM for optical communications. *J. Lightwave Technol.*, vol. 27, no. 3, pp. 189–204, 2009.

[49] Y. Tang, W. Shieh, X. Yi, and R. Evans. Optimum design for RF-to-optical up-converter in coherent optical OFDM systems. *IEEE Photon. Technol. Lett.*, vol. 19, no. 7, pp. 483–485, 2007.

[50] S. H. Han and J. H. Lee. An overview of peak-to-average power ratio reduction techniques for multicarrier transmission. *IEEE Wireless Commun.*, vol. 12, no. 2, pp. 56–65, 2005.

[51] T. Jiang and Y. Wu. An overview: peak-to-average power ratio reduction techniques for OFDM signals. *IEEE Trans. Broadcast.*, vol. 54, no. 2, pp. 257–268, 2008.

[52] Ö. Bulakçi, M. Schuster, C.-A. Bunge, and B. Spinnler. Precoding based peak-to-average power ratio reduction for optical OFDM demonstrated on compatible single-sideband modulation with direct detection. *Optical Fiber Communication Conference*, paper JThA56, 2008.

[53] S. Hellerbrand, B. Goebel, and N. Hanik. Trellis shaping for reduction of the peak-to-average power ratio in coherent optical OFDM systems. *Optical Fiber Communication Conference*, paper JThA48, 2009.

[54] B. Goebel, B. Fesl, L. D. Coelho, and N. Hanik. On the effect of FWM in coherent optical OFDM systems. *Optical Fiber Communication Conference*, paper JWA58, 2008.

[55] H. W. Kang, Y.-S. Cho, and D.-H. Youn. On compensating nonlinear distortions of an OFDM system using an efficient adaptive predistorter. *IEEE Trans. Commun.*, vol. 47, no. 4, pp. 522–526, 1999.

[56] K. Wesolowski and J. Pochmara. Efficient algorithm for adjustment of adaptive predistorter in OFDM transmitter. *Proceedings of IEEE Vehicular Technology Conference*, pp. 2491–2496, 2008.

[57] F. H. Gregorio. *Analysis and compensation of nonlinear power amplifier effects in multi-antenna OFDM systems*. Ph.D. dissertation, Helsinki University of Technology, Finland, 2007.

[58] A. N. D'Andrea, V. Lottici, and R. Reggiannini. Nonlinear predistortion of OFDM signals over frequency-selective fading channels. *IEEE Trans. Commun.*, vol. 49, no. 5, pp. 837–843, 2001.

[59] Y. Tang, K.-P. Ho, and W. Shieh. Coherent optical OFDM transmitter design employing predistortion. *IEEE Photon. Technol. Lett.*, vol. 20, no. 11, pp. 954–956, 2008.

[60] Y. London and D. Sadot. Nonlinear effects mitigation in coherent optical OFDM system in presence of high peak power. *J. Lightwave Technol.*, vol. 29, no. 21, pp. 3275–3281, 2011.

[61] D. J. F. Barros and J. M. Kahn. Optical modulator optimization for orthogonal frequency-division multiplexing. *J. Lightwave Technol.*, vol. 27, no. 13, pp. 2370–2378, 2009.

[62] C. Sánchez, B. Ortega, and J. Capmany. System performance enhancement with pre-distorted OOFDM signal waveforms in DM/DD systems. *Opt. Express*, vol. 22, no. 6, pp. 7269–7283, 2014.

[63] Y. Bao, Z. Li, J. Li, X. Feng, B. Guan, and G. Li. Nonlinearity mitigation for high-speed optical OFDM transmitters using digital pre-distortion. *Opt. Express*, vol. 21, no. 6, pp. 7354–7361, 2013.

[64] G. Shulkind and M. Nazarathy. Nonlinear digital back propagation compensator for coherent optical OFDM based on factorizing the Volterra series transfer function. *Opt. Express*, vol. 21, no. 11, pp. 13145–13161, 2013.

[65] S. C. Thompson. *Constant envelope OFDM phase modulation*. Ph.D. dissertation, Univ. of California, San Diego, CA, 2005.

[66] C. Berger, Y. Benlachtar, R. Killey, and P. Milder. Theoretical and experimental evaluation of clipping and quantization noise for optical OFDM. *Opt. Express*, vol. 19, no. 18, pp. 17713–17728, 2011.

[67] J. A. Fredenburg and M. P. Flynn. Statistical analysis of ENOB and yield in binary weighted ADCs and DACs with random element mismatch. *IEEE Trans. Commun.*, vol. 59, no. 7, pp. 1396–1408, 2012.

[68] H. E. Rowe. Memoryless nonlinearities with Gaussian inputs: elementary results. *Bell Syst. Tech. J.*, vol. 61, no. 7, pp. 1519–1525, 1982.

[69] D. Dardari, V. Tralli, and A. Vaccari. A theoretical characterization of nonlinear distortion effects in OFDM systems. *IEEE Trans. Commun.*, vol. 48, no. 10, pp. 1755–1764, 2000.

[70] D. Tsonev, S. Sinanovic, and H. Haas. Complete modeling of nonlinear distortion in OFDM-based optical wireless communication. *J. Lightwave Technol.*, vol. 31, no. 18, pp. 3064–3076, 2013.

[71] Z. Li, I. Shubin, and X. Zhou. Optical interconnects: recent advances and future challenges. *Opt. Express*, vol. 23, no. 3, pp. 3717–3720, 2015.

[72] J. C. Cartledge and A. S. Karar. 100 Gb/s intensity modulation and direct detection. *J. Lightw. Technol.*, vol. 32, no. 16, pp. 2809–2814, 2014.

[73] K. Zhong, X. Zhou, T. Gui, L. Tao, Y. Gao, W. Chen, J. Man, L. Zeng, A. P. T. Lau, and C. Lu. Experimental study of PAM-4, CAP-16, and DMT for 100 Gb/s short reach optical transmission systems. *Opt. Express*, vol. 23, no. 2, pp. 1176–1189, 2015.

[74] X. Xu, E. Zhou, G. N. Liu, T. Zuo, Q. Zhong, L. Zhang, Y. Bao, X. Zhang, J. Li, and Z. Li. Advanced modulation formats for 400-Gbps short-reach optical inter-connection. *Opt. Express*, vol. 23, no. 1, pp. 492–500, 2015.

[75] K. Zhong, X. Zhou, Y. Gao, W. Chen, J. Man, L. Zeng, A. P. T. Lau, and C. Lu. 140-Gb/s 20-km transmission of PAM-4 signal at 1.3 μm for short reach communications. *IEEE Photon. Technol. Lett.*, vol. 27, no. 16, pp. 1757–1760, 2015.

[76] Y. Kai, M. Nishihara, T. Tanaka, R. Okabe, T. Takahara, J. C. Rasmussen, H. Ishihara, K. Goi, and K. Ogawa. 130-Gbps DMT transmission using silicon Mach-Zehnder modulator with chirp control at 1.55-μm. *Optical Fiber Communication Conference*, paper Th4A.1, 2015.

[77] P. Dong, J. Lee, Y. Chen, L. L. Buhl, S. Chandrasekhar, J. H. Sinsky, and K. Kim. Four-channel 100-Gb/s per channel discrete multi-tone modulation using silicon photonic integrated circuits. *Optical Fiber Communication Conference*, paper Th5B.4, 2015.

[78] L. Nadal, M. Svaluto Moreolo, J. M. Fàbrega, A. Dochhan, H. Griesser, M. Eiselt, and J. Elbers. DMT modulation with adaptive loading for high bit rate transmission over directly detected optical channels. *J. Lightw. Technol.*, vol. 32, no. 21, pp. 4143–4153, 2014.

[79] W. Ling, I. Lyubomirsky, and O. Solgaard. Digital quadrature amplitude modulation with optimized non-rectangular constellations for 100 Gb/s transmission by a directly-modulated laser. *Opt. Express*, vol. 22, no. 9, pp. 10844–10857, 2014.

[80] T. Pfau, X. Liu, and S. Chandrasekhar. Optimization of 16-ary quadrature amplitude modulation constellations for phase noise impaired channels. *European Conference and Exhibition on Optical Communication*, paper Tu.3.A.6, 2011.

[81] T. Pfau. Noise-resilient constellations for an optical transport system, 2014.

[82] L. Beygi, E. Agrell, and M. Karlsson. Optimization of 16-point ring constellations in the presence of nonlinear phase noise. *Optical Fiber Communication Conference*, paper OThO4, 2011.

[83] A. T. Nguyen, W. C. Ng, and L. A. Rusch. An optimized 16-QAM constellation for mitigating impairments of phase noise and limited transmitter ENOB in optical coherent detection systems. *European Conference and Exhibition on Optical Communication*, paper Tu.1.3.5, 2014.

[84] B. Guo and C.-M. Hwang. Multiple payload slicer system with prenormalization integer values, 2003.

[85] W. R. Peng. Direct detection optical OFDM. *Optical Fiber Communication Conference*, paper Th3K.7, 2014.

[86] A. Al Amin, H. Takahashi, I. Morita, and H. Tanaka. 100-Gb/s direct-detection OFDM transmission on independent polarization tributaries. *IEEE Photon. Technol. Lett.*, vol. 22, no. 7, pp. 468–470, 2010.

[87] G. J. Foschini, R. Gitlin, and S. Weinstein. Optimization of two-dimensional signal constellations in the presence of Gaussian noise. *IEEE Trans. Commun.*, vol. 22, no. 1, pp. 28–38, 1974.

[88] W. R. Peng. Analysis of laser phase noise effect in direct-detection optical OFDM transmission. *J. Lightw. Technol.*, vol. 28, no. 17, pp. 2526–2536, 2010.

[89] C. R. Berger, Y. Benlachtar, R. I. Killey, and P. A. Milder. Theoretical and experimental evaluation of clipping and quantization noise for optical OFDM. *Opt. Express*, vol. 19, no. 18, pp. 17713–17728, 2011.

[90] H. A. Mahmoud and H. Arslan. Error vector magnitude to SNR conversion for nondata-aided receivers. *IEEE Trans. Wireless Commun.*, vol. 8, no. 5, pp. 2694–2704, 2009.

[91] Y. Li, S. Xu, and H. Yang. Design of signal constellations in the presence of phase noise. *in Proc. IEEE Vehicular Technology Conference (VTC'08)*, pp. 1–5, 2008.

[92] D. D. Feldman and F. Chethik. Two-dimensional constellation generation, pruning, and partial gray coding for bandwidth and power efficiency, 2003.

[93] P. S. Chow, J. M. Cioffi, and J. A. C. Bingham. A practical discrete multitone transceiver loading algorithm for data transmission over spectrally shaped channels. *IEEE Trans. Commun.*, vol. 43, no. 2, pp. 773–775, 1995.

[94] Z. Liu, T. Richter, C. Schubert, D. J. Richardson, and R. Slavík. Practical considerations on discrete multi-tone transmission for cost-effective access networks. *Optical Fiber Communication Conference*, paper M3J.4, 2015.

[95] N. Cvijetic. OFDM for next-generation optical access networks. *J. Lightwave Technol.*, vol. 30, no. 4, pp. 384–398, 2012.

[96] E. Wong. Next-generation broadband access networks and technologies. *J. Lightwave Technol.*, vol. 30, no. 4, pp. 597–608, 2012.

[97] P. Vetter. Next generation optical access technologies. *European Conference and Exhibition on Optical Communication*, paper Tu.3.G.1, 2012.

[98] P. Prat. Technologies for a cost effective UDWDM-PON. *Optical Fiber Communication Conference*, paper Th3I.3, 2015.

[99] J. von Hoyningen-Huene and C. Ruprecht. OFDM for optical access. *Optical Fiber Communication Conference*, paper Tu1H.1, 2015.

[100] H.-Y. Chen, M. Yuang, P. Tien, D.-Z. Tien, C.-C. Wei, Y.-S. Tsai, and J. Chen. Design and demonstration of a colorless WDM-OFDMA PON system architecture achieving symmetric 20-Gb/s transmissions with residual interference compensation. *Opt. Express*, vol. 21, no. 18, pp. 21097–21104, 2013.

[101] E. Hugues-Salas, R. P. Giddings, X. Q. Jin, Y. Hong, T. Quinlan, S. Walker, and J. M. Tang. REAM intensity modulator-enabled 10Gb/s colorless upstream transmission of real-time optical OFDM signals in a single-fiber-based bidirectional PON architecture. *Opt. Express*, vol. 20, no. 19, pp. 21089–21100, 2012.

[102] T. Dong, Y. Bao, Y. Ji, A. P. T. Lau, Z. Li, and C. Lu. Bidirectional hybrid OFDM-WDM-PON system for 40-Gb/s downlink and 10-Gb/s uplink transmission using RSOA remodulation. *IEEE Photon. Technol. Lett.*, vol. 24, no. 22, pp. 2024–2026, 2012.

[103] J. Yu, M.-F. Huang, D. Qian, L. Chen, and G.-K. Chang. Centralized lightwave WDM-PON employing 16-QAM intensity modulated OFDM downstream and OOK modulated upstream signals. *IEEE Photon. Technol. Lett.*, vol. 20, no. 18, pp. 1545–1547, 2008.

[104] P. C. Schindler M. C. Santos V. Polo J. Leuthold I. Tomkos I. N. Cano, X. Escayola and J. Prat. Experimental demonstration of a statistical OFDM-PON with multiband ONUs and elastic bandwidth allocation. *J. Opt. Commun. Netw.*, vol. 7, no. 1, pp. A73–A79, 2015.

[105] N. Cvijetic, M. Cvijetic, M.-F. Huang, E. Ip, Y.-K. Huang, and T. Wang. Terabit optical access networks based on WDM-OFDMA-PON. *J. Lightwave Technol.*, vol. 30, no. 4, pp. 493–503, 2012.

[106] P. C. Schindler, R. Schmogrow, M. Dreschmann, J. Meyer, I. Tomkos, J. Prat, H.-G. Krimmel, T. Pfeiffer, P. Kourtessis, A. Ludwig, D. Karnick, D. Hillerkuss, J. Becker, C. Koos, W. Freude, and J. Leuthold. Colorless FDMA-PON with flexible bandwidth allocation and colorless, low-speed ONUs. *J. Opt. Commun. Netw.*, vol. 5, no. 10, pp. A204–A212, 2013.

[107] M.-F. Huang, D. Qian, and N. Cvijetic. A novel symmetric lightwave centralized WDM-OFDM-PON architecture with OFDM-remodulated ONUs and a coherent receiver OLT. *European Conference and Exhibition on Optical Communication*, paper Tu.5.C.1, 2011.

[108] B. Charbonnier A. Lebreton and J. Le Masson. A single wavelength 25-Gb/s symmetric FDMA PON. *J. Lightwave Technol.*, vol. 33, no. 8, pp. 1630–1634, 2015.

[109] A. Nespola J. Chang V. Ferrero R. Gaudino S. Straullu, P. Savio and S. Abrate. Demonstration of upstream WDM+FDMA PON and real time implementation on an FPGA platform. *European Conference and Exhibition on Optical Communication*, paper Mo.3.4.3., 2015.

[110] P. Gysel and R. K. Staubli. Statistical properties of Rayleigh backscattering in single-mode fibers. *J. Lightwave Technol.*, vol. 8, no. 4, pp. 561–567, 1990.

[111] A. J. Lowery and J. Armstrong. Orthogonal-frequency-division multiplexing for dispersion compensation of long-haul optical systems. *Opt. Express*, vol. 14, no. 6, pp. 2079–2084, 2006.

[112] B. Charbonnier, N. Brochier, and P. Chanclou. Reflective polarisation independent Mach-Zenhder modulator for FDMA/OFDMA PON. *Electron. Lett.*, vol. 46, no. 25, pp. 1682–1683, 2010.

[113] J. Toulouse. Optical nonlinearities in fibers: review, recent examples, and systems applications. *J. Lightwave Technol.*, vol. 23, no. 11, pp. 3625–3641, 2005.

[114] C. W. Chow, C.-H. Yeh, C. H. Wang, F. Y. Shih, and S. Chi. Rayleigh backscattering performance of OFDM-QAM in carrier distributed passive optical networks. *IEEE Photon. Technol. Lett.*, vol. 20, no. 18, pp. 1545–1547, 2008.

[115] T. M. Schmidl and D. C. Cox. Robust frequency and timing synchronization for OFDM. *IEEE Trans. Commun.*, vol. 45, no. 12, pp. 1613–1621, 1997.